Nature and origin of the cover sequence of the Tuscan basement on Elba Island: evidence from detrital zircon dating

Master of Science thesis

Hallgeir Sirevaag

Department of Earth Science
University of Bergen
2013

Acknowledgement

First of all, I would like to thank my team of supervisors, Prof. Joachim Jacobs, Dr. Anna Ksienzyk, Prof. Jan Košler and Prof. Sergio Rocchi, for excellent help during these two years. Joachim is thanked for the great supervision and for giving me the opportunity to work with such an interesting project. Anna is thanked for very good help with everything from sampling and lab-work to reviewing of the thesis. I would like to thank Sergio for being great support during the fieldwork and when it comes to local knowledge on Elba and the Italian geology. I also would like to thank Jan for providing great help with the LA-ICPMS analyses.

I had a lot of help during the fieldwork. Therefore, I would first of all like to thank Henrik Stokke for being a great field assistant and for providing new perspectives during the fieldwork. I would also like to thank Andrea Dini and Gabriele Paoli for the help with the sampling and sampling strategy.

This thesis included lots of hours of lab work. I would therefore like to thank Benjamin Emmel and Martina Suppersberger for help with the mineral separation. Tereza Konopasekova and Irina Dumitru are thanked for the help with the making of thin-sections and for mount preparation. In addition to these, I would especially like to thank Egil Erichsen for great help with the cathodoluminescence imaging and Siv Hjort Dundas for valuable help on the LA-ICPMS lab.

I would like to thank all present and former members of the Bergen Tectonics and Thermochronology group (BeTTh) for great discussions, help and good times during these two years.

In addition to Joachim and Anna, I have had invaluable help from Christian Rønnevik, Kari Moldskred Sekkingstad, Karen Cecilie Johannessen, Hanne Labugt Angell and Carita Grindvik Knudsen for reviewing and for providing very constructive feedback and new perspectives to the thesis. Also, Kristian Agasøster Haaga has provided excellent help with the petrographic microscope. I would therefore like to thank all of you for spending so much time on helping me with this thesis!

I would like to thank all my fellow geology and geophysics students at the University of Bergen for five wonderful years filled with unforgettable memories from field trips and hours at the university, including coffee-breaks and social events. In addition to this, I would also like to thank Vegard Aamodt for great support and good company during the last year.

Finally, I would like to thank my family for the invaluable support during these five years and for showing interest and enthusiasm in this project. Thank you very much!

Bergen, 31 May 2013

Hallgeir Sirevaag

Abstract

Elba Island represents the westernmost part of the northern Apennines and has, for the last decades, been a subject to comprehensive geological studies. Due to west-directed subduction of the Adriatic microplate below Corsica-Sardinia since late Cretaceous times, resulting in piling-up of Tuscan-, Ligurian- and Ligurian-Piedmontese units, and the late Eocene-early Miocene thrusting of the Ligurian accretionary wedge onto the Tuscan margin, it is difficult to determine the origin of the metasedimentary rocks on Elba. Still, most of the age relationships of the metasedimentary rocks on Elba are based fossil content or on correlation of similar rocks in mainland Tuscany, Corsica and Sardinia. Because very little information is available about the provenance of the cover sequence of the Tuscan basement on Elba, this study aims at providing more accurate age relationships for selected lithologies within the Ortano, Acquadolce and Monticiano-Roccastrada units on eastern Elba, as well as trying to trace the origin of the sediments.

Detrital zircons from six samples from eastern Elba have been U/Pb dated. The LA-ICPMS technique has been applied in order to analyse a large quantity of zircons. This is the first study to provide U/Pb zircon crystallization ages for the unimodal populations or subpopulations within the quartzo-phyllitic Capo d'Arco Schists (Ortano Unit) and the phyllites and metasiltstones (Acquadolce Unit), respectively.

New constraints on the maximum age of deposition is provided for most of the selected lithologies. Maximum deposition ages of Lower Devonian and uppermost Silurian times are suggested for the Capo d'Arco Schists and the blackish quartzites and phyllites, respectively. A crystallization age for the igneous source rock of the quartzo-phyllitic Capo d'Arco Schist is calculated to 422±8 Ma. Analyses of the phyllites and metasiltstones provide controversial, yet very interesting results. The phyllites and metasiltstones, which previously have been attributed to the upper part of the Lower Cretaceous, contains a subpopulation of young, idiomorphic detrital zircons. These form a tight unimodal population with an age of 32±1 Ma. This is interpreted to represent the crystallization of an igneous source rock and is used to establish a maximum age of deposition of late Eocene-early Oligocene age. The previously suggested late Carboniferous-early Permian age of the Rio Marina Formation and the Middle-Upper Triassic age of the Verruca Formation is still be regarded as reasonable, on the basis of U/Pb dating from the present study.

The U/Pb data from the present study provide further evidences for an African affinity of the metasediments. It is suggested that the majority of the zircons in the present study can be interpreted as being erosional products from the African continent, the Iberian Massif and from the late Eocene-middle Miocene igneous phase on Sardinia.

Contents

1 Introduction

Elba Island represents the westernmost part of the northern Apennines and is located about 50 km east of Corsica in the northern Tyrrhenian Sea (Fig. 1a). Thus, it is an important area for the understanding of the interplay between the northern Apennine chain and Corsica, as well as the evolution of the western Mediterranean. The geological evolution of Elba includes a late Cretaceous-early Miocene convergence between Africa+Adria and Europe+Iberia, followed by extension, igneous activity and the formation of the Tuscan Magmatic Province. Due to its complex geological evolution, Elba is interesting both for structural studies and provenance studies. As most of the lithologies on Elba have been dated by correlation with similar lithologies on Corsica, Sardinia and mainland Tuscany, very few provenance studies have been published. This study will therefore present the provenance of selected lithologies in the lowermost part of the tectonic nappe pile on eastern Elba Island.

1.1 Previous work

The first proper geological study in modern times was carried out by Trevisan (1950*; in* e.g. Bortolotti et al., 2001a). Trevisan defined five geological complexes on eastern Elba, and this marked the start of major geological studies on the island. Complex I-V are described in detail in chapter 2.2. Bortolotti et al. (2001a) published a revision of the structural and stratigraphic setting on central and eastern Elba. This work included a further division of the 5 complexes defined by Trevisan (1950; *in* e.g. Bortolotti et al., 2001a) into 9 main units and 8 subunits.

Elba Island has been a subject to comprehensive geological studies since the work by Trevisan. However, very few geochronological studies have been undertaken. Most of the ages suggested for the lithologies on Elba are based on correlation either with the Apuane Alps or the Paleozoic formations on Sardinia (Bortolotti et al., 2001a; Musumeci et al., 2011). Recently, Musumeci et al. (2011) published the first provenance study from the lowermost units represented by the Ortano Porphyroids and the Mt. Calamita Schist, showing middle Ordovician and early Carboniferous ages, respectively. This study also proposed that the Mt. Calamita Schist is derived from the Visean flysch deposits in the Variscan chain and it confirmed the ages and correlations between the Ortano Porphyroids and the magmatic rocks of the Paleozoic basement on Sardinia (Pandeli and Puxeddu, 1990). Later on, Jørgensen (2011) presented a refined proposal for the provenance of the Mt. Calamita Schist in Porto Azzurro Unit, as well as the Capo d'Arco Schist, the Ortano Porphyroids and the silver-grey phyllites and quartzites, all in the Ortano Unit.

1.2 Research objective

Musumeci et al. (2011) and Jørgensen (2011) have presented provenance studies on eastern Elba that provided data from the two lowermost complexes. By the use of U/Pb zircon dating, this study focuses on complementing these data by providing the detrital zircon ages and determining

the provenance for selected lithologies from the Mt. Calamita Formation in Complex I, the Ortano Unit and the Aquadolce Unit in Complex II and the lower parts of the Monticiano-Roccastrada Unit in Complex III.

Pandeli and Puxeddu (1990) suggest that the Capo d'Arco Schist could be interpreted as the base of the Ortano Unit. However, Bortolotti et al. (2001a) propose that the silver-grey phyllites and quartzites and the Capo d'Arco Schist represent a single horizon that was folded as an east-vergent overturned fold with the porphyroids in the center. U/Pb analyses of two varieties of the Capo d'Arco Schist will be compared with analyses of the porphyroids and the silver-grey phyllites and quartzites from Musumeci et al. (2011) and Jørgensen (2011). This is done in order to the test the hypotheses of Pandeli and Puxeddu (1990) and Bortolotti et al. (2001a).

1.3 Study area

This study focuses on the Mt. Calamita Schist (Complex I), the Capo d'Arco Schist, the blackish quartzites and phyllites and the phyllites and metasiltstones (all from Complex II) and the Rio Marina and Verruca formations (both complex III). These lithologies are mainly exposed on eastern Elba, more specifically between the Capo d'Arco residence in the south and Topinetti Beach in the north (Fig. 1b). In addition to this, the Porto Azzurro Unit was studied on the Mt. Calamita promontory towards the southeastern end of Elba. Most of the samples from Complex I, II and III were obtained at well-exposed roadcuts, coastal outcrops or in the open-pit Rio Marina Mine. The study of the Capo d'Arco Schist was carried out at well-exposed coastal outcrops between the southern side of the Capo d'Arco residence and Ortano Beach, as well as along the southeastern side of Ex. Vedetta.

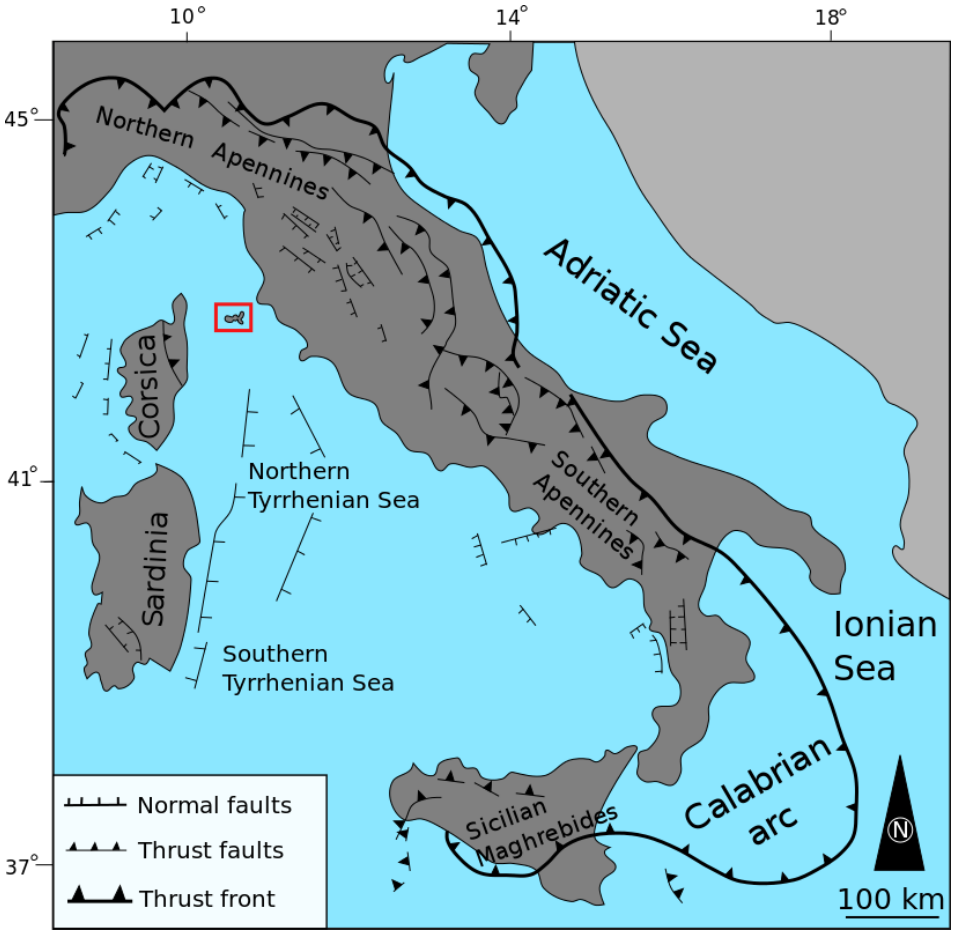

(a)

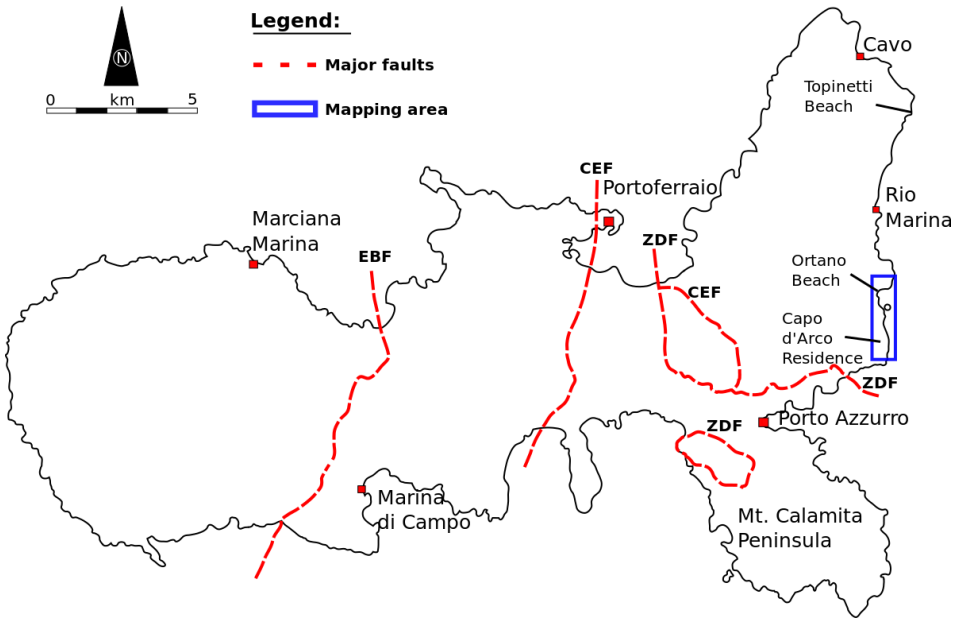

(b)

Fig. 1: a) Overview map of Italy and Tyrrhenian Sea, showing the main regional tectonic features in the area and the position of Elba Island (red square); b) Simplified map of Elba, showing mapping area of Capo d'Arco Schist in blue and main faults in red. **EBF** - Eastern Border Fault; **CEF** - Central Elba Fault; **ZDF** - Zuccale Detachment Fault. Modified after Rosenbaum and Lister (2004) and Westerman et al. (2004)

2 Regional geology

The geological evolution of the Mediterranean is now fairly constrained for a long period of time. For a long time, it was believed that the geology of the Mediterranean was a result of the Variscan orogeny, as well as the closure of a single oceanic domain known as the Tethys. However, since 1940-1950, it has been suggested that the area is the result of the formation and consumption of two oceanic domains known as Paleotethys and Neotethys, in addition to some smaller oceanic basins (Cavazza and Wezel, 2003; Stampfli and Hochard, 2009). Also, it has been suggested that the Prototethys existed prior to the Paleotethys (Stampfli, 2000). This oceanic domain was probably bordering the North African-Australian side of Gondwana. Little is known about the Prototethys and it is still not constrained whether the Prototethys was a late Proterozoic or a Cambrian ocean (Stampfli, 2000). The Prototethys will not be discussed further in this part.

The Tethyan oceans were first defined by Stöcklin (1974; *in* Stampfli, 2000). It is now generally accepted that the Paleotethys existed north of the Cimmerian superterrane during the Paleozoic and that the Neotethys existed during the late Paleozoic-Mesozoic south of the Cimmerian superterrane. However, the Paleotethyan and the Neotethyan reconstructions are controversial. In addition to the Paleotethys and the Neotethys, a middle Jurassic ocean, the Alpine Tethys, existed as an extension of the central part of the Atlantic ocean (Cavazza and Wezel, 2003). The Paleotethys, the Variscan orogeny, the Neotethys and the Alpine Tethys will be described in more detail in this section.

Von Raumer et al. (2002) suggested that the Paleotethys ocean opened as a result of the stepwise detachment of the Hun superterrane from the northern Gondwanan margin during the late Ordovician-early Devonian rifting (Fig. 2). The Paleotethys was a triangular embayment, narrowing towards the west (Şengör et al., 1984). The closure of this oceanic domain was probably finalized during the Middle-Late Triassic (Stampfli et al., 2001) and, as a result of this, the Cimmerian orogenic system was formed. The Cimmerian superterrane consisted of the following blocks: Adria, Hellenides-western Taurides externides, Menderes-Taurus, Sanadaj-Sirjan, Alborz, Lut-central Iran, central Afghanistan, south Tibet and Sibu Masu (Stampfli, 2000). A Permian-Triassic reconstruction of the Paleotethys and Neotethys oceans and the Cimmerian superterrane is shown in Fig. 3.

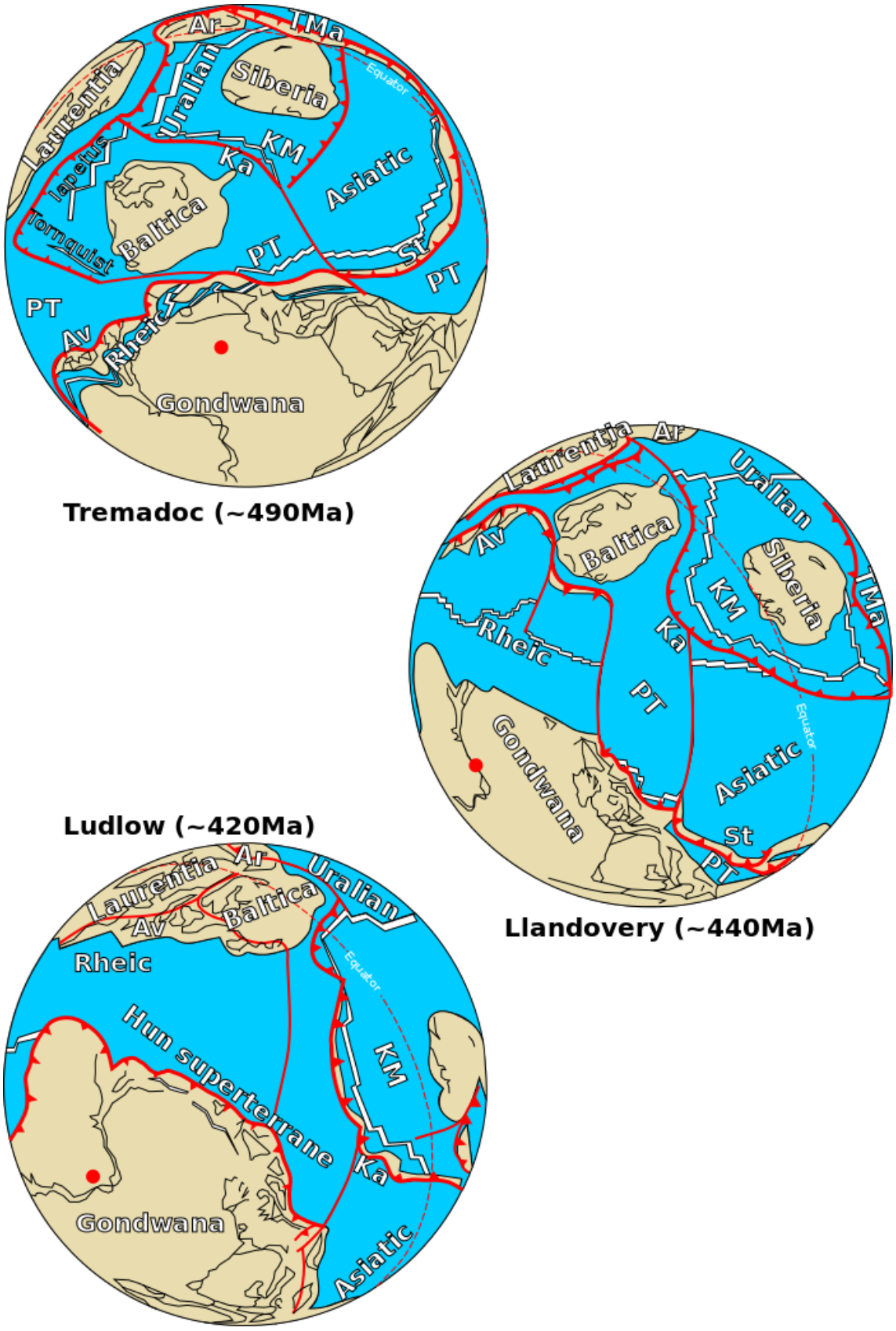

Fig. 2: Early-middle Paleozoic reconstruction showing the location of the different oceanic domains with respect to Gondwana, Laurentia and Baltica. Red dot indicates the location of the south pole. **Ar:** Arctida; **Av:** Avalonia; **Ka:** Kipchak arc; **KM:** Khanty-Mansi; **PT:** Prototethys **St:** Serinda terranes; **TMa:** Tuva-Mongol arc; Modified after Stampfli and Borel (2002).

Between the early Ordovician and the late Carboniferous, a large mountain belt extending from the Appalachian to the Caucasus was formed as a result of a diachronous collision between Gondwana and Laurentia-Baltica (Matte, 2001). The microcontinents Avalonia and Armoria were, at that stage, located between Gondwana and Laurentia-Baltica. It is suggested that the closure of the Rheic oceanic domain, an oceanic domain located between Avalonia and Armoria, resulted in the formation of the Variscan orogeny when Gondwana collided with Avalonia and Armoria (Matte, 2001). Matte (1986, 2001) suggests that the closure of this oceanic domain could be divided into a period of a two-sided subductions (600-420 Ma) and obductions (420-380 Ma). A second period of intracontinental deformation took place between the Late Devonian and the Early Permian (Matte, 1986). Also, it is interpreted that the main metamorphic event during the Variscan orogeny was during this accretion and when the mid-ocean ridge of Paleotethys was subducted during the early Carboniferous (Stampfli and Borel, 2002).

The Alpine and Variscan mountain chains are important parts of the geology in the Mediterranean area. These mountain chains are mainly build up by pre-Variscan rocks, derived from the active Gondwana margin (Stampfli and Borel, 2002; von Raumer et al., 2003). By studying the pre-Variscan basement of Sardinia, Gaggero et al. (2012) distinguished three Ordovician magmatic cycles: 1) A late Cambrian-Lower Ordovician ($492 - 480$ Ma) stage that could be linked to rifting, 2) a Middle Ordovician cycle (~ 465 Ma) linked to volcanic arcs and 3) an Upper Ordovician-Silurian cycle (~ 440 Ma) that has been linked to the rift-drift stages.

Paleotethys was followed by the Neotethys (Fig. 4). Different ages have been proposed for the opening of the Neotethys. Stampfli et al. (2001) suggested that the Neothetys opened during the late Carboniferous-Early Permian when the Cimmerian superterrane drifted away from Gondwana, while others (e.g. Garfunkel and Derin, 1984) suggested an early Mesozoic age. Stampfli (2000) proposed that the Cimmerian superterrane was separated from Gondwana by the Neotethys from the latest Paleozoic and until the earliest Cenozoic.

An early-middle Mesozoic sinistral-oblique extension between Iberia and Africa resulted in the opening of a narrow seaway that was connecting the central Atlantic ocean and the Neotethys ocean (Platt, 2007). This seaway evolved from a Triassic-Jurassic rift system that was transecting Pangea and into the Alpine Tethys ocean (Favre and Stampfli, 1992; Stampfli, 2000; Stampfli and Hochard, 2009). Fig. 5 shows a Lower Jurassic reconstruction of the Alpine Tethys ocean. The Alpine orogenic cycle probably started during Triassic-Jurassic times (Stampfli et al., 2002a). According to Wortmann et al. (2001), the tectonic evolution of the Alpine Tethys ocean can be explained by the movement of the African, European and Adriatic microplates. Since Oligocene times, the northward subduction of the Alpine Tethys sea-floor below Spain has led to the formation and evolution of the Apenninic accretionary prism located east of Corsica and Sardinia (Stampfli et al., 2002a).

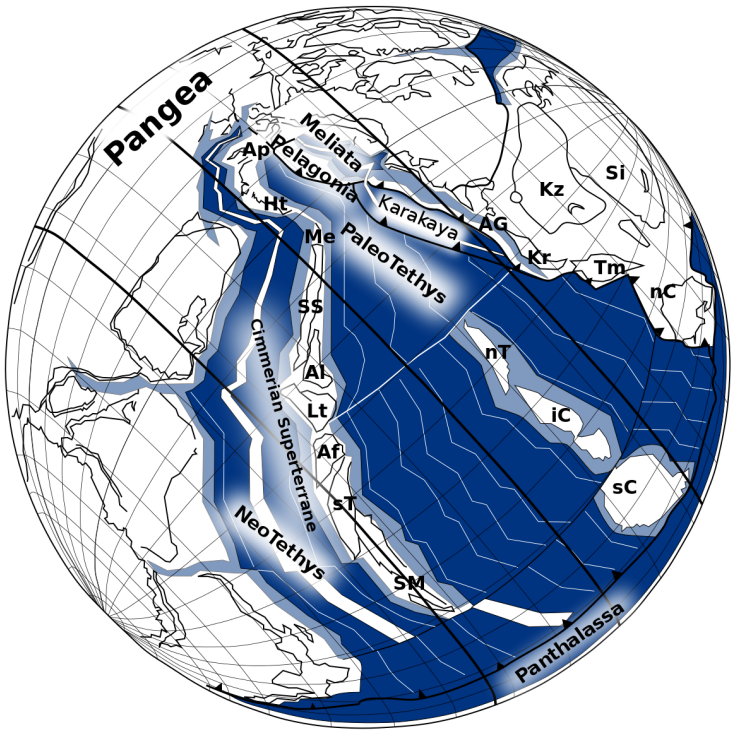

Fig. 3: Permian-Triassic reconstruction showing the Cimmerian superterrane separating the Paleotethys ocean from the Neotethys ocean. **Af:** Central Afghanistan; **Al:** Alborz; **Ap:** Apulia s.str.: **HT:** Hellenides-western Taurides externides; **IC:** Indochina and Borneo; **Lt:** Lut-central Iran **Me:** Menderes-Taurus; **nT:** north Tibet; **sC:** south China**; SM:** Sibu Masu; **SS:** Sanandaj-Sirjan; ; **st:** south Tibet. Modified after Stampfli (2000).

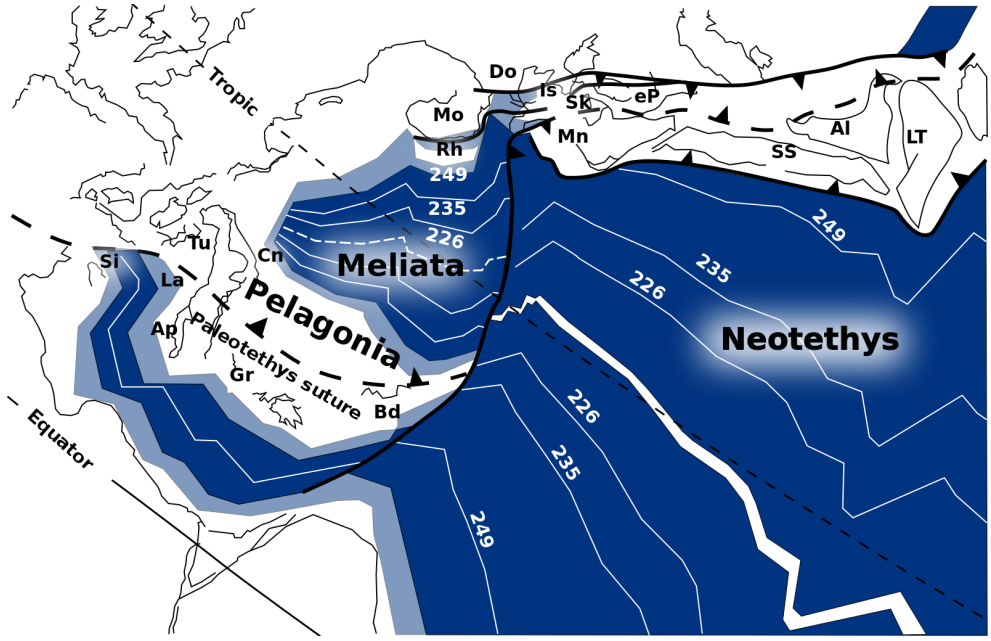

Fig. 4: Carnian reconstruction of Neotethys. **Al:** Alborz; **Ap:** Apulia s.str.; **Bd:** Bey Daglari; **Cn:** Carnic Alps; **Do:** Dobrogea; **eP:** east Pontides; **Gr:** Autochtonous of Greece; **Is:** Istanbul; **La:** Lagonegro; **LT:** Lut-Tabas; **Mn:** Menderes, Taurus; **Mo:** Moesia; **Rh:** Rhodope; **Si:** Sicannian Basin; **Sk:** Sakarya; **SS:** Sanadaj-Sirjan; **Tu:** Tuscan Nappes. Modified after Stampfli (2000).

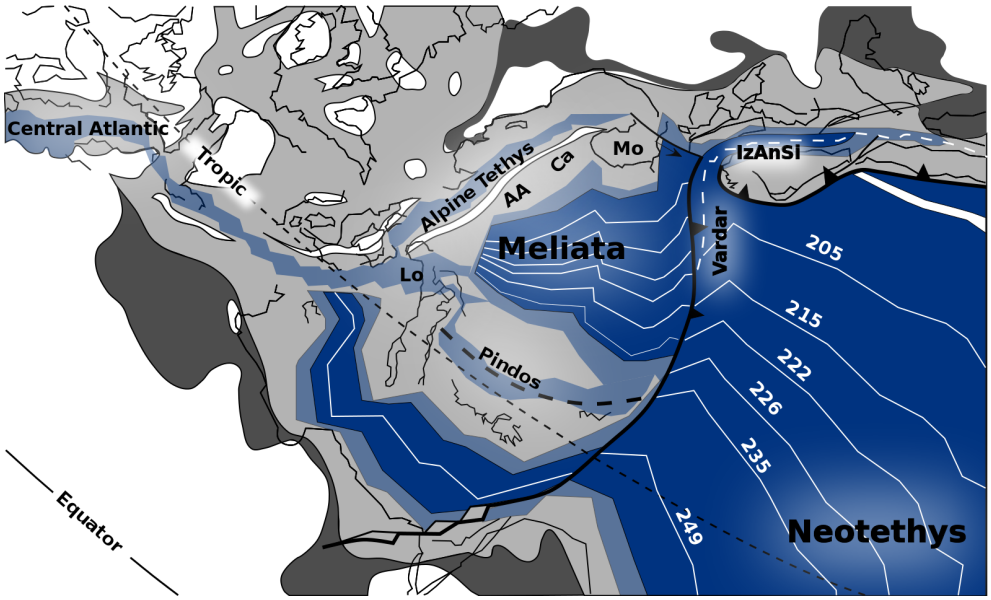

Fig. 5: Sinemurian reconstruction of the Alpine Tethys ocean, showing its relation to Neotethys and the central Atlantic ocean. **AA:** Austro-Alpine; **Ca:** Inner Carpatian; **IzAnSi:** Izmir-Ankara Ocean **Lo:** Lombardia Basin **Mo**: Moesia. Modified after Stampfli (2000).

2.1 The Apennines

The geodynamic evolution of the Corsica-Northern Apennine orogenic system probably started as a result of an oblique collision between the Africa+Adria plate and the Europe+Iberia plate during the Late Cretaceous (Bortolotti et al., 2001a, and references therein) in a transpressional regime that was dominant during Late Cretaceous-early Eocene times (Marroni and Treves, 1998). Prior to the collision, several important geodynamic processes resulted in the amalgamation of the African, Adriatic, European and Iberian plates respectively. It has been suggested that the Adriatic plate rotated 30° counter-clockwise with respect to the African plate between 130 and 80 Ma (Dercourt et al., 1986). After this, the Adriatic and African plates were linked. A collision between the European and Adriatic plates in the north led to a separation from the African plate in the south and the opening of the Mesogean ocean, an oceanic domain extending from Neotethys in the east to the Maghrebian ocean in the west . The convergence rate between Africa and Europe has been changing through time. Two periods of of relatively high convergence rates have been identified: the first during the Late Cretaceous and the second during Eocene-Oligocene times (Jolivet and Faccenna, 2000; Rosenbaum et al., 2002). Mazzoli and Helman (1994) suggested that the direction of the motion between Africa and Europe could be divided into NNE-directed conversion during late Oligocene-Burdigalian times, NNW-directed conversion during the Langhian-early Tortonian and finally NW-directed conversion from the early Tortonian to the present.

It has been suggested that the Iberian plate experienced a counter-clockwise rotation between 30° (Zeck, 1996) and 41° (Galdeano et al., 1989) with respect to Europe since 135 Ma (Fig. 6). The Iberian plate was, at that time, mainly linked to the African plate. This was followed by the progressive opening of the North Atlantic, resulting in the eastward movement of Iberia

(Zeck, 1996). The movement of Iberia with respect to Europe can, according to Rosenbaum et al. (2002), be identified as a Late Jurassic-Early Cretaceous sinistral strike-slip movement, a Late Cretaceous convergence and a more quiet time during the Paleocene followed by a short period of dextral strike-slip movement before the Eocene-Oligocene convergence.

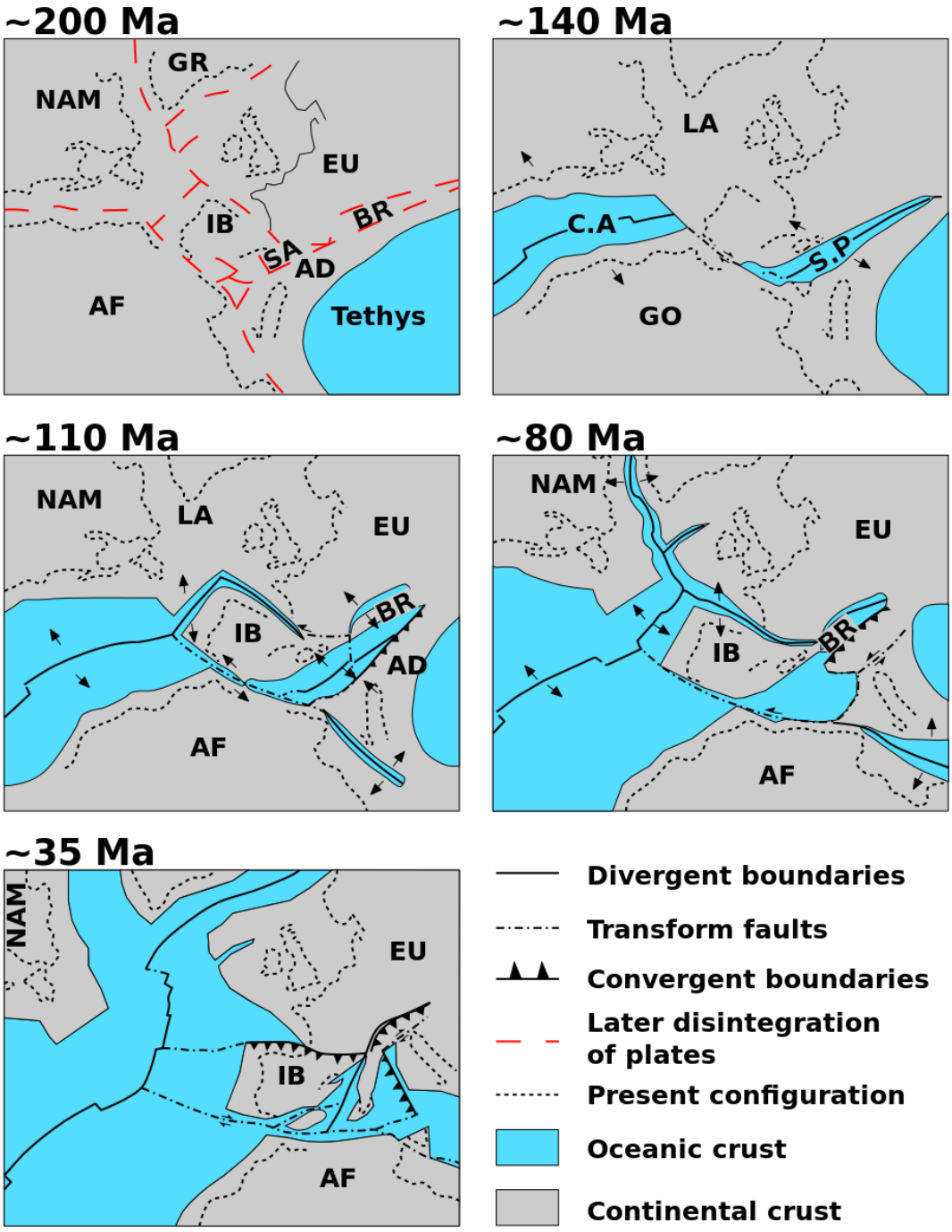

Fig. 6: Reconstruction showing the opening of the central Atlantic ocean and the south Penninic ocean between late Triassic and late Eocene-early Oligocene. The reconstruction also shows the counter-clockwise rotation of Iberia with respect to Africa. **AD:** Adria; **AF:** Africa; **BR:** Briançonia; **EU:** Eurasia; **GO:** Gondwana; **GR:** Greenland; **IB:** Iberia; **LA:** Laurasia; **NAM:** North America; **SA:** Sardinia-Corsica; **C.A:** Central Atlantic ocean; **S.P:** South Penninic ocean. Modified after Frisch (1981).

During the latest Cretaceous-early Pleistocene convergence, the European plate and the Ionian and Adriatic plates collided, resulting in the formation of the Apennine-Maghrebian fold-and-thrust belt along the subduction zone (Elter et al., 2003). The time of existence of a west-dipping subduction zone below the continental margin of Corsica is still not constrained, but different hypotheses have been proposed (Bortolotti et al., 2001a). It has been suggested that the subduction zone existed during the late Cretaceous-early Paleocene. Dating of eclogites on Corsica has given a $^{147}Sm/^{144}Nd$-age of 84 Ma (Lahondère and Guerrot, 1997) and a $^{40}Ar/^{39}Ar$-age of 90 Ma on glaucophane (Maluski, 1977; *in* Bortolotti et al., 2001a). This is used as evidence for a late Cretaceous subduction along the European margin. Siliciclastic input from the uplifted Corsica Massif, deposited as submarine fans, suggest a subduction zone beneath the Corsica margin during Campanian times (Bortolotti et al., 2001a). However, the lack of a magmatic arc is not consistent with the theory of a subduction zone. Several hypotheses have been suggested in order to explain this inconsistency. Abbate and Sagri (1982; cited in Bortolotti et al., 2001a) suggested that the subduction zone moved several times before stabilizing. Treves (1984) and Principi and Treves (1984) (both cited in Bortolotti et al., 2001a) proposed that very low convergence rates would lead to the lack of magmatism. As a result of this, the subducted slab could not have been longer than approximately 100 km between the late Cretaceous and the Oligocene. This indicates either a maximum convergence rate of 0.25 cm/year or pauses in the subduction. One of the more recent hypotheses by Marroni and Treves (1998) suggests a transcurrent regime which may have resulted in the formation of a passive subduction zone that, according to Serri et al. (1993), lasted at least until the Paleogene.

After a period of contraction since the late Mesozoic, a period of extension was initiated (Platt, 2007). The opening of the western Mediterranean started at about 30 Ma as irregular basins were generated during back-arc extension due to roll-back of the hangingwall of the Apennine-Maghrebian subduction zone. These basins have a progressively younger age towards the east (Gueguen et al., 1998). The oldest basins are the Alboran, Valencia and Liguro-Provençal basins in the western Mediterranean with late Oligocene-Miocene ages (Gueguen et al., 1998; Jolivet and Faccenna, 2000). The present-day tectonic setting in the Mediterranean is shown in Fig. 7. Speranza et al. (2002) suggest that the opening of the back-arc basin was related to a counter-clockwise rotation of the Corsica-Sardinia block (Fig. 8). The Tyrrhenian basin is located further east and has a late Miocene to Plio-Pleistocene age (Kastens et al., 1988; Gueguen et al., 1998).

During late Paleogene-Neogene times, the Northern Apennine fold-and-thrust belt developed as a result of the collision between the Corsica-Sardinia block and the Adriatic microplate (Tavarnelli, 1997; Bortolotti et al., 2001a; Massoli et al., 2006). It is generally agreed that the Corsica-Sardinia block rotated counter-clockwise during the same time, but the timing of this rotation is debated. Alvarez (1972) suggested that the Corsica-Sardinia block rotated between 11.5 and 6.0 Ma, while Gueguen (1995; *in* Gueguen et al., 1998) proposed that the Corsica-Sardinia block rotated 60° between 25 and 10 Ma.

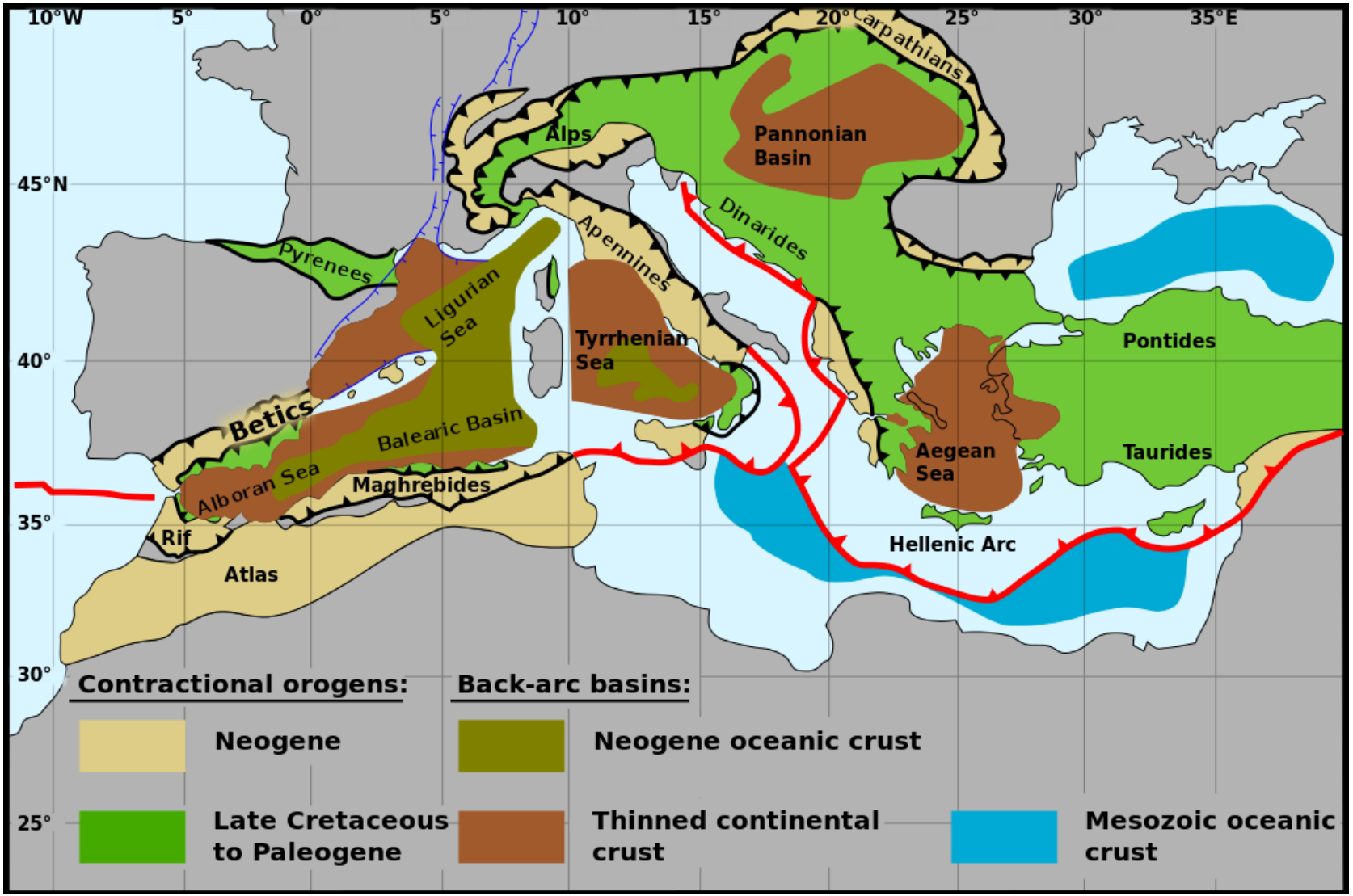

Fig. 7: The present-day tectonic setting of the Mediterranean, showing the different contractional orogens and back-arc basins in the area. The red line represents the boundary between Eurasia and Africa. Modified after Platt (2007)

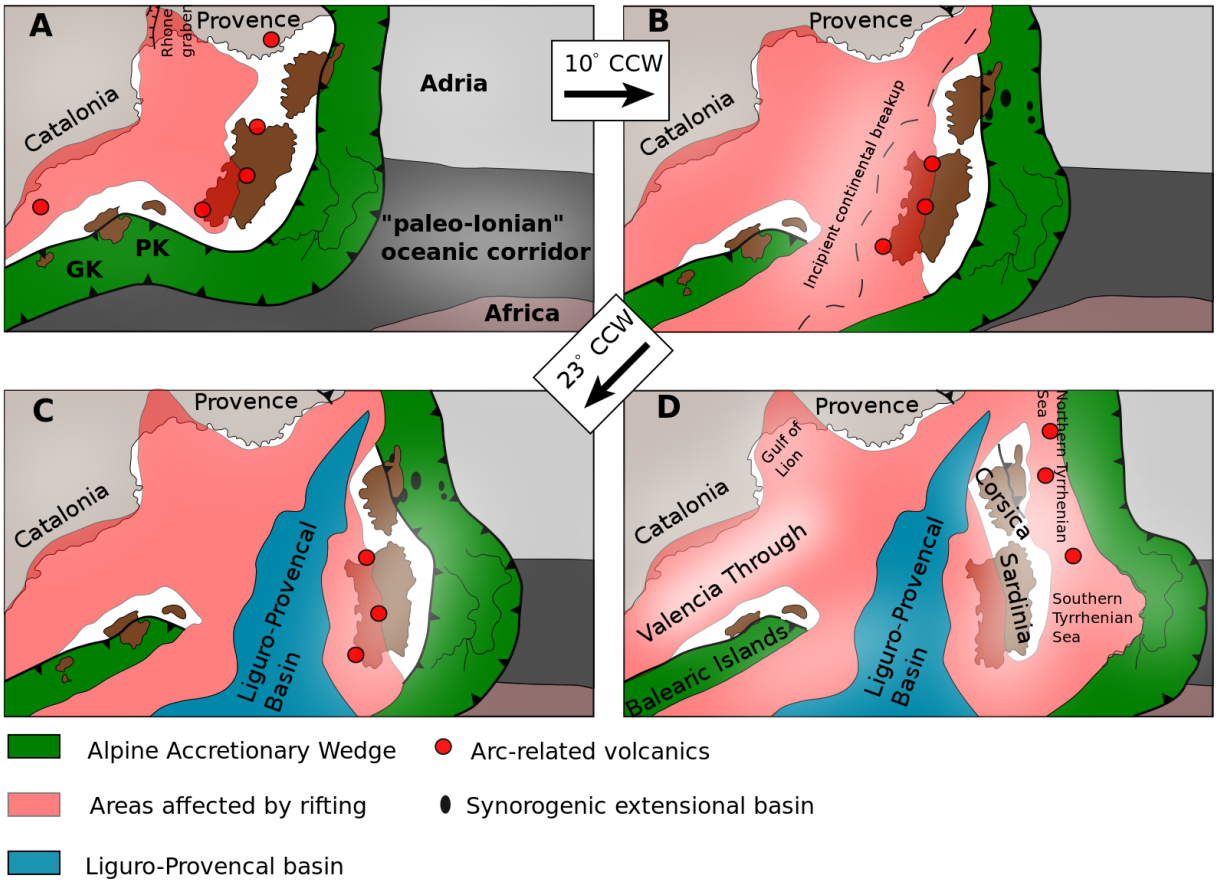

Fig. 8: Rotation of Corsica-Sardinia and the opening of the Liguro-Provençal basin between the early Burdigalian and the early Messinian (20-7 Ma). **a)** early Burdigalian; **b)** early-mid Burdigalian; **c)** early Langhian; **d)** early Messinian. Modified after Speranza et al. (2002)

2.2 Geological framework of Elba Island

Elba Island is located in the northern part of the Tyrrhenian Sea, a part of the western Mediterranean. The tectonic evolution of Elba has therefore been strongly influenced by the evolution of these areas and. according to Benvenuti et al. (2001), the evolution can be divided into an accretionary stage, a continent-continent collision stage and a post-orogenic extension stage.

The first stage of the evolution of Elba was the accretionary stage. During the Late Cretaceous, an oblique convergence between Africa+Adria and Europe+Iberia was initiated (Dewey et al., 1989; Marroni and Treves, 1998). This resulted in the west-directed oceanic subduction of the Adriatic microplate below the Corsica-Sardinia microplate lasting at least until the Paleogene (Serri et al., 1993), and marked the start of the accretionary stage in the evolution of Elba. Several events during the accretionary stage led to the piling up of the Ligurian-, Tuscan- and Liguria-Piedmontese units on Elba (Complex I-V). The oceanic lithosphere in the Alpine Tethys ocean was subducted below the Corsica-Sardinia continental margin during the accretionary stage. The oceanic crust was then trapped between the continental margin of Corsica and the ophiolitic units in the Ligurian accretionary wedge (Fig. 9). During the Late Cretaceous erosion started on the continental margin of Corsica and the siliciclastic material was deposited as large submarine fans on the trapped crust (Bortolotti et al., 2001a). Pelagic sedimentation continued

on the Tuscan margin during this period.

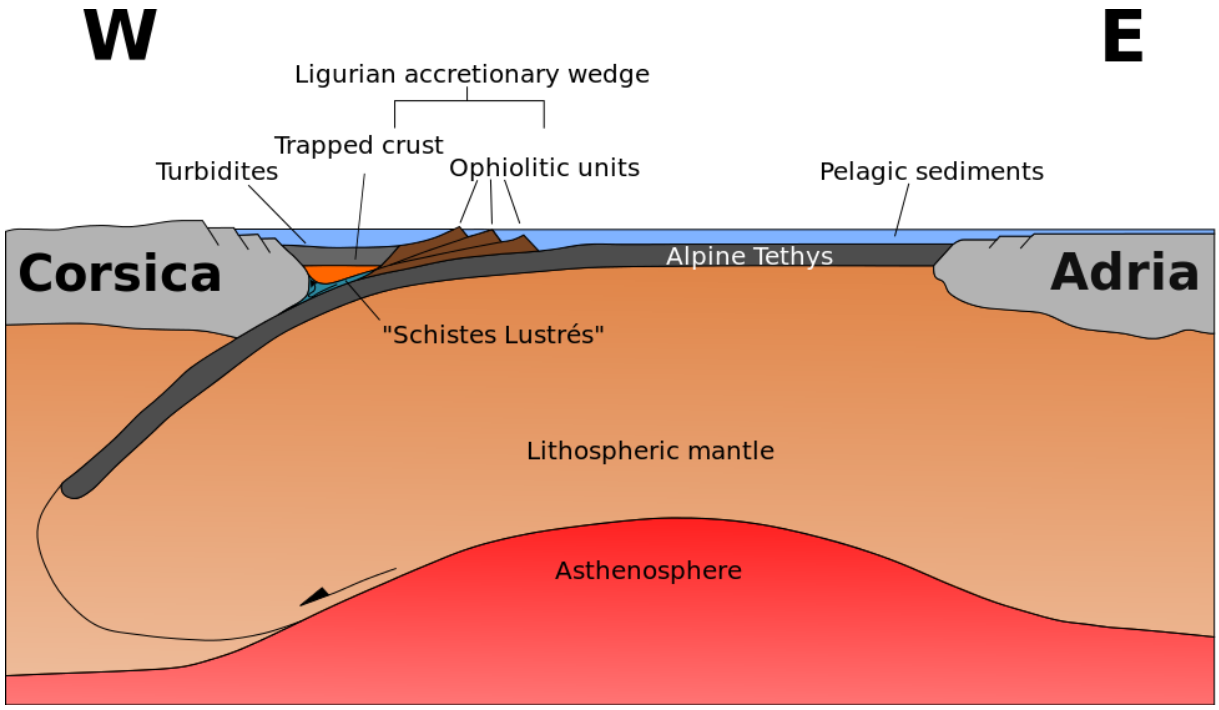

Fig. 9: Sketch showing the convergence between Adriatic (east) and Corsica (west) margins resulting in trapped oceanic crust in-between Corsica and the Ligurian accretionary wedge. This was the configuration during the Late Cretaceous-early Paleocene. Modified after Bortolotti et al. (2001a).

Between late Paleocene and early Eocene, the subducted oceanic slab reached the upper part of the asthenosphere. Simultaneously, the lithospheric mantle in the mantle wedge below Corsica became modified as a result of the upwelling fluids.

The second phase of the tectonic evolution was the continent-continent collision phase. It corresponds to all events between the late Eocene/Oligocene and the early Miocene. The oceanic subduction was replaced by foredeep subduction. During this period, the eastern margin of Corsica became overthrust by the trapped crust and was incorporated into the northern Apennines orogenic system (Bortolotti et al., 2001a). Between the late Eocene and the early Miocene, the Ligurian accretionary wedge was thrust onto the Tuscan continental margin (Fig. 10) leading to imbrication of the westernmost Tuscan lithosphere.

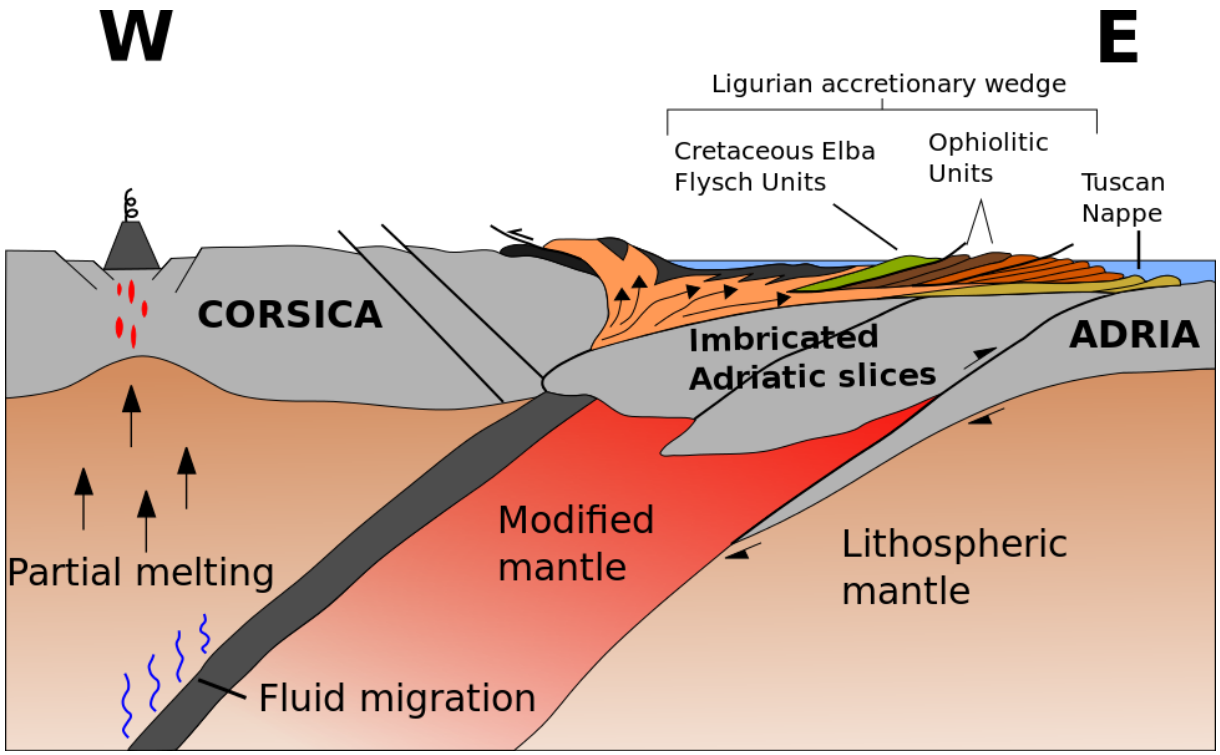

Fig. 10: Continent-continent collision during Oligocene-early Miocene resulting in imbrication of the Adriatic slices during the subduction. The Cretaceous flysch units (Complex V), ophiolithic units (Complex IV) and the Tuscan Nappes (Complex III) are units that are present at Elba Island. Modified after Bortolotti et al. (2001a).

The post-orogenic extensional phase is the third and last phase of the tectonic evolution of Elba Island. This phase was initiated in the Apennines by the eastward roll-back of the west-dipping subduction zone and the upwelling of asthenosphere during the middle Miocene. The rifting of the Tyrrhenian Sea was initiated during the middle-late Miocene (Bartole, 1995). According to Rosenbaum and Lister (2004), two main periods of roll-back induced back-arc extension can be distinguished: The first period (10-6 Ma) affected the northern and western parts of the Tyrrhenian Sea, while the second (starting at 6-5 Ma) mainly influenced the southern part of the Tyrrhenian Sea.

Several different processes have been proposed as the mechanism for the extension: 1) Barberi et al. (1973) stated that the southern Tyrrhenian basin was formed by an abyssal plain. By studying the volcanism in this area, they found that the magmatic activity could be related to back-arc processes. Due to this, Barberi et al. (1973) suggested that the abyssal plain was a marginal basin produced by extension. 2) Mantovani et al. (1997) suggest that the extensional regime that led to the opening of different basins and troughs (e.g. the Tyrrhenian Sea and the Valencia trough) was a secondary effect of the outward extrusion of crustal wedges resulting from longitudinal compression in for example the Apennines. 3) A hypothesis by Carmignani and Kligfield (1990) involves rapid underplating of the accretionary wedge during the earlier stages that led to an overthickened accretionary wedge resulting in gravitational collapse. The gravitational collapse led to extensional tectonics on both upper- and mid-crustal levels in the Apennines. The attenuated continental crust was affected by intrusion of hot asthenosphere

resulting in large-scale extension and volcanism. Other possible mechanisms have also been suggested. Roeder (1980; *in* Finetti et al., 2001) suggested that delamination was a possible explanation, while e.g. Van Bemmelen (1972; *in* Finetti et al., 2001) proposed that different processes associated with the uprising of mantle and gravity sliding resulted in the extension.

Due to the eastward migration of the subduction zone during the third stage, the post-orogenic igneous activity also migrated eastward. According to Serri et al. (1993) and Rocchi et al. (2002), the ages recorded for this igneous activity span from 14 Ma in the west to 0.1 Ma to the east (Fig. 11). Marinelli (1967; *in* Serri et al., 1993) was the first who referred to this region as the Tuscan Magmatic Province, a magmatic province covering a total area of 30 000 km^2 in the northern Tyrrhenian Sea and in southern Tuscany (Dini et al., 2002). The magmatic activity of the northern Apenninic arc was intense during Neogene-Quaternary times and this activity can, according to Serri et al. (1993), be separated into four phases that are separated both in time and space: Phase I - ∼14 Ma; Phase II - 7.3-6.0 Ma; Phase III - 5.1-2.2 Ma and Phase IV - 1.3-0.1 Ma. The Mt. Capanne and La Serra-Porto Azzurro plutons on Elba are of Miocene age and are therefore correlated to the second and third phase of the Tuscan igneous activity (Serri et al., 1993; Dini et al., 2002; Maineri et al., 2003). Together, the plutons cover about 100 km^2 of the island (Poli, 1992). Thermometamorphism associated with the intrusion of the La Serra-Porto Azzurro Pluton is recorded as e.g. the presence of andalusite±cordierite in the Capo d'Arco Schist and as skarn bodies within the Porto Azzurro Unit, Ortano Unit, Acquadolce Unit and Monticiano-Roccastrada Unit (Duranti et al., 1992; Bortolotti et al., 2001a).

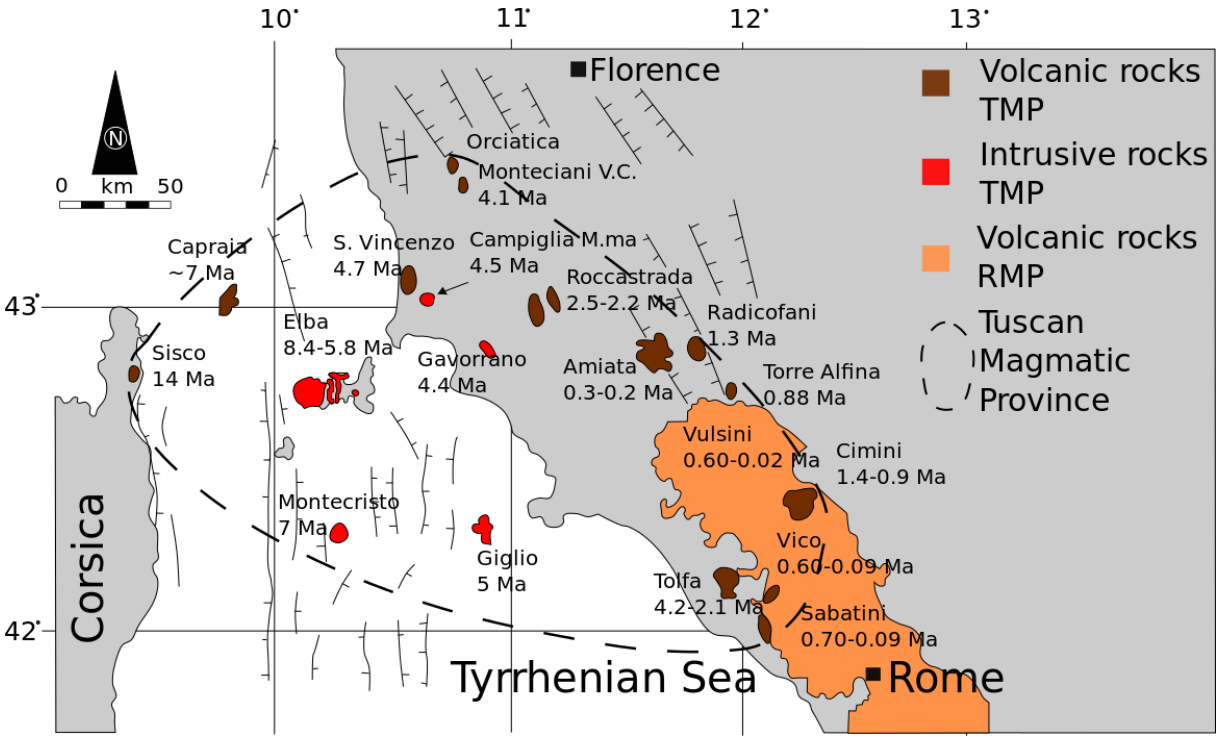

Fig. 11: Map of the Tuscan Magmatic Province showing the middle Miocene-present igneous activity in the northern Tyrrhenian Sea and in southern Tuscany, as well as the main extensional faults and the extent of the Tuscan Magmatic Province. **TMP** - Tuscan Magmatic Province; **RMP** - Roman Magmatic Province. Modified after Dini et al. (2002) and Westerman et al. (2004).

According to Bortolotti et al. (2001a), the uplift related to the Mt. Capanne Pluton (7.0-6.8 Ma) induced gravitational sliding of the nappes on the east and west sides of the pluton along the Central Elba Fault (CEF). The emplacement of the La Serra-Porto Azzurro Pluton (5.9 Ma) resulted in a north-eastwards extensional detachment known as the Zuccale Detachment Fault (Fig. 12 and 13).

2.2.1 Tectonostratigraphy

Termier (1909; *in* e.g. Bortolotti et al., 2001b) was the first who described the allochtonous units on Elba Island. Later on, Trevisan (1950; *in* e.g. Bortolotti et al. 2001a) defined 5 tectonostratigraphic units or complexes on Elba Island (Fig. 12). These complexes are stacked with an east vergence (Fig. 13). Complex I-III are of Tuscan origin, while Complex IV and V have a Ligurian origin. Bortolotti et al. (2001a) divided these complexes into 9 units and 8 subunits, resulting in 17 main slices of the tectonic pile. The 5 complexes and 9 units are summarized in table 1. An objective of this study is to analyse lithologies from the three lowermost complexes and therefore the selected lithologies are described in the section 2.3.

Table 1: The five complexes defined by Trevisan (1950) separated into 9 major units by Bortolotti et al. (2001a).

Complex	Unit	Origin
I	Porto Azzurro Unit	Tuscan
II	Ortano Unit	
	Acquadolce Unit	Ligurian-Piedmontese
III	Monticiano-Roccastrada Unit	Tuscan
	Tuscan Nappe	
	Gràssera Unit	
IV	Ophiolitic Unit	Ligurian
V	Paleogene Flysch Unit	
	Cretaceous Flysch Unit	

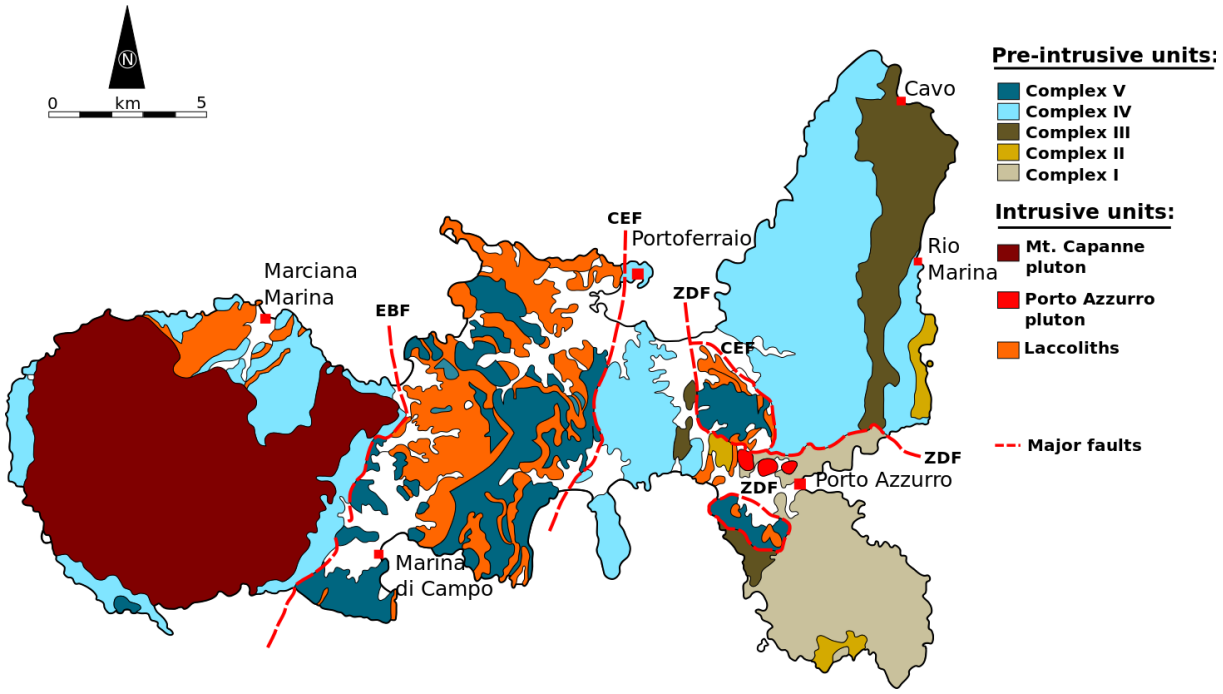

Fig. 12: Geological map of Elba Island showing the 5 complexes defined by Trevisan (1950) as well as the two major plutons and other, smaller intrusive units. **EBF**: Eastern Border Fault; **CEF**: Central Elba Fault; **ZDF:** Zuccale Detachment Fault. Modified after Westerman et al. (2003).

Complex I is the lowest complex on Elba Island and has a Cambrian-Triassic age (Bortolotti et al., 2001a). This complex is made up of the Porto Azzurro Unit and is exposed on south-eastern Elba, mainly on the Mt. Calamita peninsula. It consists mainly of micaschists covered by dolomitic limestones and crystalline dolostones, as well as lenses of amphibolite (Bortolotti et al., 2001a).

Complex II is separated from Complex I by the low-angle Zuccale Detachment Fault (ZDF). Bortolotti et al. (2001a) divided this complex into the Ordovician Ortano Unit and the Cretaceous-Paleogene Acquadolce Unit. The Ortano Unit has a terrestrial origin and has been correlated to the Paleozoic Tuscan succession of the Apuane Alps on the mainland (Pandeli and Puxeddu, 1990). This unit consists of micaschists, phyllites, quartzitic phyllites and metavolcanic rocks. In addition to this, the Capo d'Arco Schist includes thin aplitic dykes and quartzitic lenses related to the Porto Azzurro Pluton. The Acquadolce Unit has a marine origin and is made up of marbles grading up to calcschists, phyllites and metasiltstones and serpenitised peridotites at the boundary to Complex III. Elter and Pandeli (2001) suggest that the Acquadolce Unit has a Ligurian-Piedmontese origin. This is based on structural differences between the underlying and overlying units. The Acquadolce Unit is believed to represent the "Schistes Lustrés" (Fig. 9), which was a result of HT-LP metamorphism in the accretionary wedge during Late Cretaceous-early Paleocene (Bortolotti et al., 2001a; Elter and Pandeli, 2001).

Complex III is the uppermost of the Tuscan complexes on Elba and has a shallow marine origin. It comprises the Monticiano-Roccastrada Unit, the Tuscan Nappe and the Gràssera Unit. The Monticiano-Roccastrada Unit is made up of graphitic metasedimentary rocks with a Carboniferous-Permian age at the base. Its upper part contains limestones, chert, metasiltstones

and phyllites which have an Oligocene age at the top (Bortolotti et al., 2001b). The Tuscan Nappe contains mostly calcareous-dolomitic breccias and carbonatic, carbonatic-cherty and marly-carbonatic formations with a Triassic-Jurassic age. The Gràssera Unit is the uppermost unit in Complex III and consists of calcschists and cherts at the base. The rest of this unit is mainly made up of varicolored slates and siltstones (Bortolotti et al., 2001a,b). According to Elter and Pandeli (2001), the Gràssera and Monticiano-Roccastrada units have the same structural features as the Ortano Unit in Complex II. Therefore, they suggest that the Ortano Unit, the Monticiano-Roccastrada Unit and the Gràssera Unit represent a single, wedging stratigraphic succession that is similar to successions on the Monticiano-Roccastrada ridge and on Monti Pisani that could be linked to extension in the Tyrrhenian Sea (Elter and Pandeli, 2001).

Complex IV is from the Ligurian domain and was defined by Bortolotti et al. (2001a) as the Ophiolitic Unit. The Ophiolitic Unit comprises four subunits: Aquaviva Subunit, consisting of serpentinites and ophicalcites at the boundary to Complex III, as well as cherts and shales; Mt. Serra Subunit, consisting of ophicalcites, cherts and limestones; Sassi Turchini Subunit, composed of serpentinites and the Volterraio Subunit, made up of gabbros, basalts, cherts, limestones and shales. This unit has been interpreted to be a relic of the trapped crust in the Ligurian oceanic basin, with a Cretaceous-Jurassic age (Bortolotti et al., 2001b).

The uppermost complex is Complex V. This was divided by Bortolotti et al. (2001a) into the Paleogene Flysch Unit and the Cretaceous Flysch Unit. The Paleogene Flysch Unit contains Paleogene, shaly-marly succession including ophiolitic breccias, turbiditic limestones and sandstones (Bortolotti et al., 2001b). The Cretaceous Flysch Unit consist of shales, siliciclastic and conglomeratic sandstones, as well as a sheared complex of ophiolitic and pelagic rocks. This unit is cross-cut by porphyritic and aplitic dykes that may be related to the Mt. Capanne granite (Bortolotti et al., 2001b).

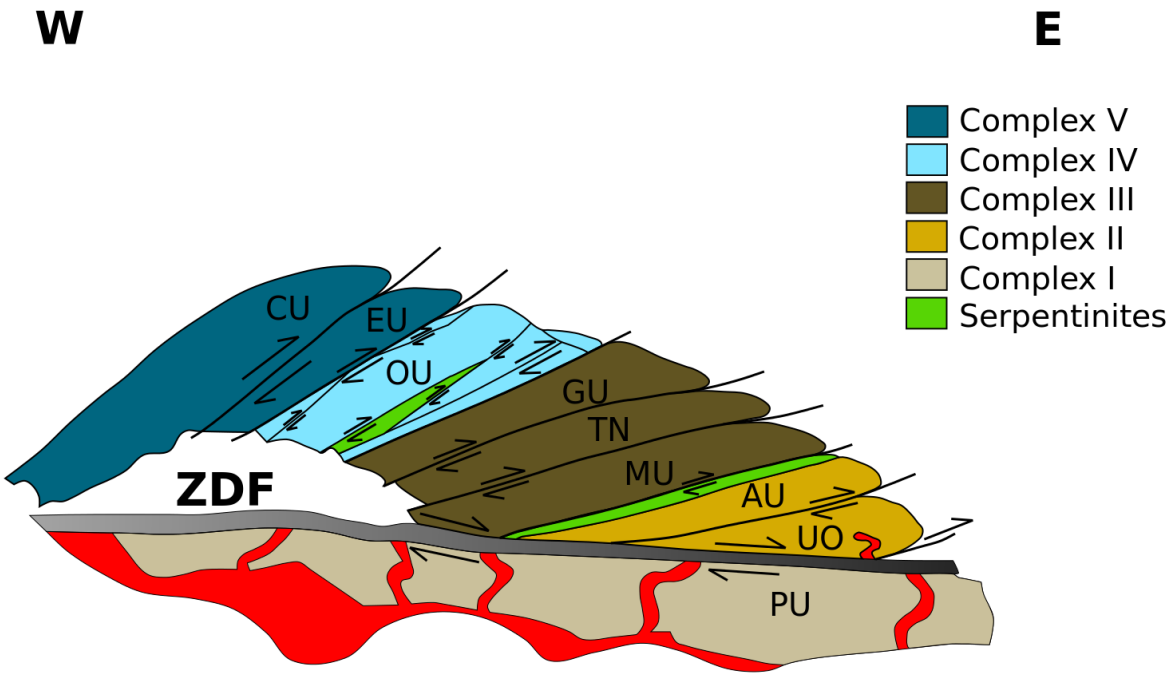

Fig. 13: A simplified sketch showing the stacking of the 5 complexes defined by Trevisan (1950) separated into the 9 units defined by Bortolotti et al. (2001a) on central and eastern Elba. **PU**: Porto Azzurro Unit; **UO:** Ortano Unit; **AU:** Acquadolce Unit; **MU:** Monticiano-Roccastrada Unit; **TN:** Tuscan Nappe; **GU**: Gràssera Unit; **OU:** Ophiolitic Unit; **EU:** Paleogene Flysch Unit; **CU:** Cretaceous Flysch Unit; **ZDF:** Zuccale Detachment Fault. Modified after Bortolotti et al. (2001a) and Barnes et al. (2006).

2.3 Main lithologies

This study presents detrital zircons data from the cover units of the Tuscan basement. Thus, the lithologies that were studied were selected from the Porto Azzurro-, Ortano-, Acquadolce- and Monticiano-Roccastrada units in Complex I-III.

Mt. Calamita Schist

The Mt. Calamita Schist (Fig. 14a) is the tectono-stratigraphic lowermost lithology on Elba Island and it is the main constituent in the Porto Azzurro Unit. It is exposed on the Mt. Calamita peninsula, between Porto Azzurro and Cala di Mola Residence, as well as at Reale and Barbarossa beaches. The Mt. Calamita Schist is composed of fine-grained, greyish micaschists and quartzites that mainly consist of quartz, feldspar, muscovite and biotite. It is also crosscut by tourmaline-bearing aplitic dykes related to the La Serra-Porto Azzurro Pluton. Andalusite and cordierite also occur in this lithology (Puxeddu et al., 1984). Based on geochemical and petrological data by Puxeddu et al. (1984), a Paleozoic age has been established for this lithology. Garfagnoli et al. (2005) have suggested that the age is probably pre-Carboniferous. Jørgensen

(2011) suggested that the sediments were derived from the imbricated slices formed during the early Miocene collision between the western Adriatic margin and Corsica (Fig. 10).

Capo d'Arco Schist

The Capo d'Arco Schist (Fig. 14b) is the basal lithology of the Ortano Unit and is observed along coastal outcrops on the western side of Mt. Arco and towards the southern end of the Capo d'Arco residence. The Capo d'Arco Schist appears both as dark micashist and a light quartzitic phyllite. The micaschist is stratigraphically overlain by the quartzitic phyllite which again is in tectonic contact with the porphyroids. The contact between the micaschist and the quartzitic phyllite is usually observed as a sharp, folded contact.

The micaschist is dark grey in colour and consist mainly of biotite, quartz and feldspar. Cm- and dm-scale quartz seggregations are present as thin veins or tension gashes. The quartz seggregations appear as isoclinally folded. The isoclinal folds are plunging either towards north or west. Tourmalines with a preferred orientation in aplite dykes may indicate the fold axial plane of a more open fold. Compared to the quartzitic phyllite, the micaschist appear more weathered. The quartzitic phyllite is light grey in colour and consists mainly of quartz and feldspar, but also muscovite and graphite. The quartz segregations are larger, but fewer than in the micaschist. The quartzitic phyllite is more foliated than the micaschist. Contact metamorphic minerals (andalusite±cordierite) and quartzitic lenses are observed within both varieties.

Based on the correlation with a terrigenous sequence on Sardinia and the Apuan Alps, Duranti et al. (1992) have suggested an Cambrian-Ordovician age of this lithology. Puxeddu et al. (1984) suggest that the Capo d'Arco Schists are reworked porphyroids, while Bortolotti et al. (2001a) propose a correlation with the silver-grey phyllites and quartzites.

Blackish quartzites and phyllites

The blackish quartzites and phyllites (Fig. 14c) crop out between the southern side of the Ortano Valley in the north and the Capo d'Arco residence in the south. The lithology appear as a fine-grained, dark grey metasandstone-metasiltstone or as metaconglomerate. Foliation on the cm- to dm-scale is present, and quartz veins parallel to and crosscutting the foliation can be observed. The thickness of the blackish quartzites and phyllites varies between 0 and 10 meters (Bortolotti et al., 2001a). Duranti et al. (1992) defined the blackish quartzites and phyllites as a part of the Ortano Porphyroid, and suggested a Middle Ordovician age of this lithology based on correlations from Sardinia.

Phyllites and metasiltstones

The phyllites and metasiltstones (Fig. 14d) comprise the largest part of the Acquadolce Unit in Complex II with a thickness of about 300 meters (Bortolotti et al., 2001a). This lithology can be observed in the Ortano Valley and Rio Marina-Porticiello on eastern Elba and around Golfo Stella on central Elba. The phyllites and metasiltstones are mainly made up of dark grey to

grey-greenish phyllites that are well foliated. More massive and lighter coloured metasiltstones are interlayering the phyllites.

Lenses of calcschist are abundant in this lithology and skarn mineralization is present in some of these lenses. Duranti et al. (1992) have suggested that the age of this lithology is the upper part of Lower Cretaceous based on traces of microfossils. Based on this, Duranti et al. (1992) suggest that the phyllites and metasiltstones could be linked to the Ligurian-Piedmontese domain instead of the Tuscan domain. This is also supported by structural data from Elter and Pandeli (2001). They also suggest that the Acquadolce Unit was emplaced onto the Tuscan succession in the Ortano Unit.

Rio Marina Formation

The Rio Marina Formation (Fig. 14e) crops out mainly from the road between Rio Marina and Cavo, across Mt. Fico and to the Ortano Valley. This formation is made up of black to grey phyllites and metasandstones with sericite in the foliation planes. On the mm-scale, biotite±andalusite may be observed.

A littoral-deltaic depositional environment of late Carboniferous-early Permian age has been suggested by e.g. Vai (1978; *in* Bortolotti et al., 2001a) based on fossil content and sedimentological and lithological features. The thickness of the Rio Marina Formation varies between 40 and 250 meters and this variation could have a structural reason (Bortolotti et al., 2001a).

Verruca Formation

The Verruca Formation (Fig. 14f) is cropping out from the coast around Topinetti Beach in the north, in the Rio Marina Mines, across Mt. Fico and it wedges out in the Ortano Valley. The Verruca Formation can be divided into 3 main lithotypes, alternating at dm- to m-scale: a) Violet-red-green phyllites and metasiltstones; b) grey-pink-green quartzites and c) pink-white metaconglomerates.

These deposits have been correlated to the Verrucano Succession on Mt. Pisani and were there interpreted as meandering river deposits of Middle-Upper Triassic age (Rau and Tongiorgi, 1974; *in* Bortolotti et al., 2001a).

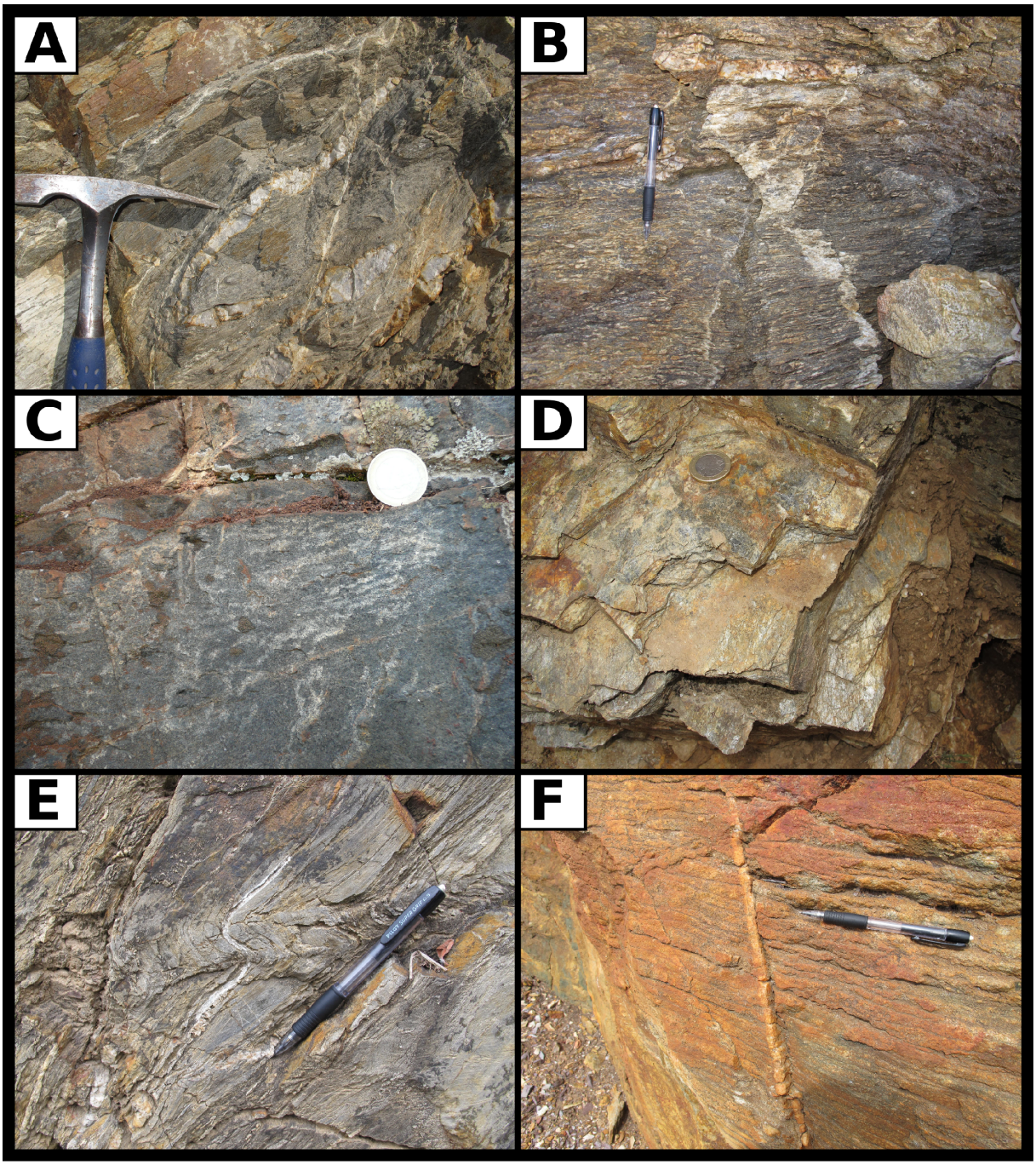

Fig. 14: Field occurance of main lithologies sampled and analysed in this project. **a)** Mt. Calamita Schist; **b)** Capo d'Arco Schist; **c)** Blackish quartzites and phyllites (Photo by A. Ksienzyk); **d)** Phyllites and metasiltstones; **e)** Rio Marina Formation; **f)** Verruca Formation.

3 Fundamentals of detrital zircon analysis

Analyses of heavy minerals ($\rho > 2.80\, g/cm^3$) in sand fractions have been used as a diagnostic tool for determining the provenance of the sediment for a long time (Morton, 1991). Because zircons are refractory minerals at the surface of the Earth, they are present in nearly all kinds of sedimentary rocks (Fedo et al., 2003). By applying precise single-grain analyzing techniques, it is possible to distinguish differences in composition of selected heavy minerals such as zircons. This could therefore be used to determine a possible source region, as well as constraining the transport, depositition and the dispersal patterns of the sediments (Morton, 1991).

Zircon is the Zr-rich endmember of the zircon (Zr) - hafnium (Hf) solid-solution serie. Zircons have the formulae $ZrSiO_4$, and the substitution between Zr and Hf is limited in extent (Morton, 1991). Zircon contains trace amounts of the rare-earth elements (REEs) and phosphorus (P), as well as long-lived radioactive isotopes (10-1000 ppm uranium (U) and 1-100 ppm thorium (Th)) that can be used for radiometric dating (Hoskin and Schaltegger, 2003; Parrish and Noble, 2003). ^{238}U decays to ^{206}Pb with a half-life $\left(t_{1/2}\right)$ of $4.468 * 10^9\, yr$, ^{235}U decays to ^{207}Pb with $t_{1/2} = 0.704{*}10^9\, yr$ (Davis et al., 2003) and ^{232}Th decays to ^{208}Pb with $t_{1/2} = 1.41{*}10^{10}\, yr$ (Nesse, 2009). Due to its chemical and physical properties, zircon is highly resistant to many geological processes, including volcanic cycles, high-grade metamorphism, erosion and transport. Also, it has the ability to preserve the original amount of radioactive U and the accumulated amount of radiometric Pb during remelting events (Davis et al., 2003). Because of these properties, zircons are well-suited for detrital studies.

3.1 Laser Ablation-Inductively Coupled Plasma Mass Spectrometry

The first attempts to use a Laser Ablation-Inductively Coupled Plasma Mass Spectrometer (LA-ICPMS) were carried out during the mid-eighties (Košler and Sylvester, 2003). The introduction of the LA-ICPMS technique allowed for much faster U/Pb dating of zircons. Košler et al. (2002) compared the LA-ICPMS with Secondary Ion Mass Spectrometry (SIMS). They found that the SIMS method tends to be 1.5-2 times more precise when it comes to U/Pb dating of zircons, but because a high number of analyses are needed for detrital studies, the LA-ICPMS appears as a well-suited technique for this.

The LA-ICPMS consists of a laser ablation cell, an ICP-torch and a mass spectrometer. The ICPMS can be divided into 4 major parts: the ion source, the vacuum system, the mass filter and the detector system (Košler and Sylvester, 2003). A schematic figure of an ICPMS is shown in Fig. 15. The first stage of the analysis is the ablation of the zircons. During this stage, a laser-beam converts small parts of the sample into an aerosol which is transported from the ablation cell towards the ICPMS with a Ar-He carrier gas mixture. This mixture is used to enhance the sensitivity with respect to Pb with a factor of 2-4 (Eggins et al., 1998; Günther and Heinrich, 1999). The aerosol is injected into a hot plasma ($8000 - 10000°K$) (Košler and Sylvester, 2003) that desolvates the aerosol into gaseous atoms and further into ions (Wolf, 2005). This stage is therefore known as the ion source.

The ions are transported towards the mass spectrometer, passing the sample- and skimmer-cones in order to reduce the pressure from atmospheric pressure to $10^{-4} - 10^{-5}\,torr$ (Košler and Sylvester, 2003). According to Košler and Sylvester (2003), only 1% of the sample passes through the cones and reaches the mass spectrometer. The ion beam is focused with the use of electrostatic lenses. Mass filtering by a magnetic sector is commonly used in order to discriminate the ions based on the mass-to-charge ratio (Wolf, 2005). A magnetic field is used to deflect the ions from their straight trajectory, based on their mass-to-charge ratio (Košler and Sylvester, 2003). Finally, the signal is recorded with a single-cup detector.

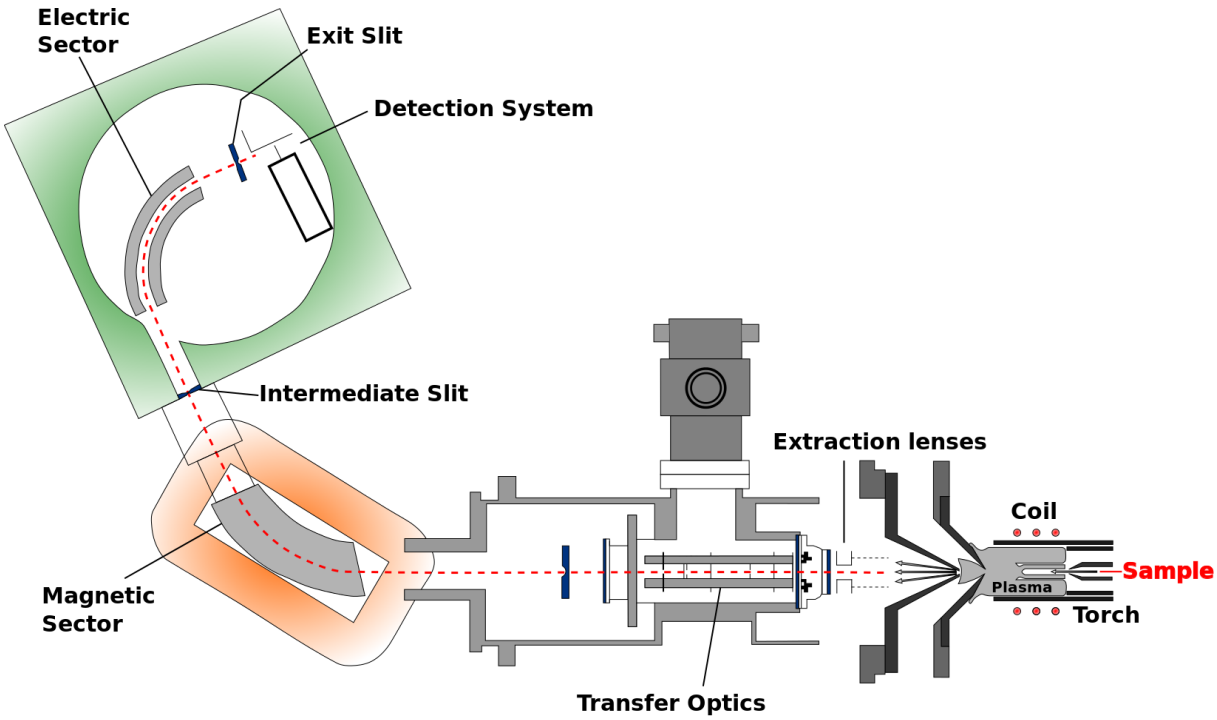

Fig. 15: Schematic figure showing the principle of the ICPMS system starting with the introduction of the sample into the plasma. The ion beam is then moving through the extraction lenses and the transfer optics before moving through the magnetic and electric sectors before the isotopes are detected. Modified after Košler and Sylvester (2003) and Wolf (2005).

Fryer et al. (1993) identified problems with the LA-ICPMS concerning variable isotope discrimination (mass bias). Elemental or isotopic fractionation is another problem that has been described by e.g. Hirata and Nesbitt (1995) and Sylvester (2008). Elemental fractionations are time-dependant changes in elemental ratios (Guillong and Günther, 2002). Several hypotheses have been proposed for elemental fractionation. Hirata and Nesbitt (1995) suggested that it might be because Pb has a greater volatility than U, while Machado and Simonetti (2001) proposed that is may be a result of large thermal gradients above the ablation pit. By comparing ages from the measured Pb/U-ratio at the different solid, red lines in Fig. 16, the difference in Pb/U-ratio will correspond to a shift in age of about 700 Ma as a result of elemental fractionation. Hirata and Nesbitt (1995) have proposed that active focusing of the laser beam during ablation will minimize the

elemental fraction effect. However, Košler and Sylvester (2003) have suggested that Eq. 1 could be used to correct for both Pb/U-ratio fractionation and mass bias at the same time. In that case, an external standard is used for correction. In Eq. 1, $R_{Sample_{True}}$ is the corrected Pb/U ratio, $R_{Sample_{Measured}}$ and $R_{Std_{Measured}}$ are average measured values of the sample and standard, respectively. $R_{Std_{True}}$ is the known isotopic ratio of the standard.

$$R_{Sample_{True}} = R_{Sample_{Measured}} * \left(\frac{R_{Std_{True}}}{R_{Std_{Measured}}} \right) \tag{1}$$

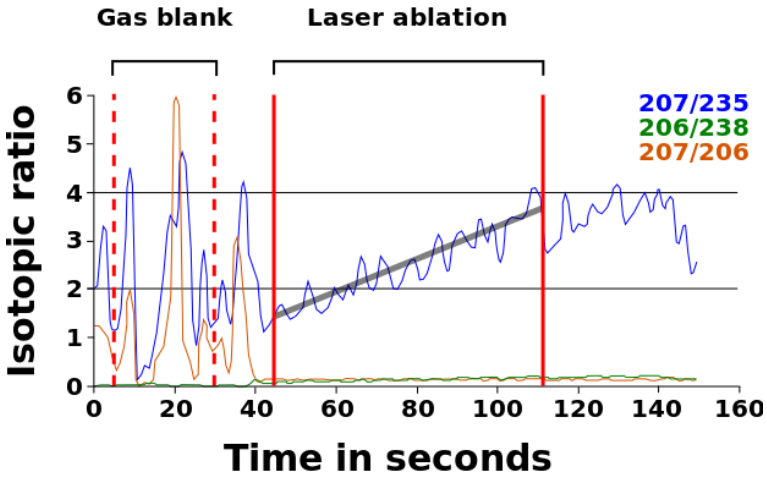

Fig. 16: A signal showing elemental fractionation that has been processed. The area between the dashed, red lines represents the selected range for the gas blank, while the area between the solid, red lines represents the selected range of signal. Faint, black line represents the trend of the signal during ablation.

4 Methods

The present study is based on fieldwork, mineral separation, mount preparation and analyses of zircons. As the fundamentals of detrital zircon studies have been described in the previous chapter, the method of the fieldwork and processing will be described in this chapter.

4.1 Fieldwork and sampling

Fieldwork was carried out on eastern Elba Island in May, 2012. Thirteen samples were obtained for detrital zircon analyses and petrographic analyses. Additionaly, three samples (EAK-01, EJ-49 and EJ-50) were collected in May 2011 by A. Ksienzyk and J. Jacobs. Sample localities were selected mainly on the basis of the lithology. Veins were avoided during sampling. Structural data were recorded for all outcrops. Sampling localities are shown in Fig. 17. An overview of the different samples, including lithology, locality and UTM coordinates, is given in Table 2. The structural data are presented in Appendix 1.

The samples obtained in this study are from eastern Elba. Samples from the Mt. Calamita Schist (EHS-01, EHS-02, EHS-03 and EHS-04) are all from the Mt. Calamita peninsula. As this study has a special focus on the Capo d'Arco Schist (Complex II), four geochronology samples (EHS-08, EHS-12, EHS-13 and EHS-15) and two thin-section samples (EHS-07 and EHS-14) were obtained from different varieties of this lithology.

In order to avoid contamination, all samples used for detrital zircon studies were crushed on the outcrop into pieces small enough to feed directly into the discmill for crushing.

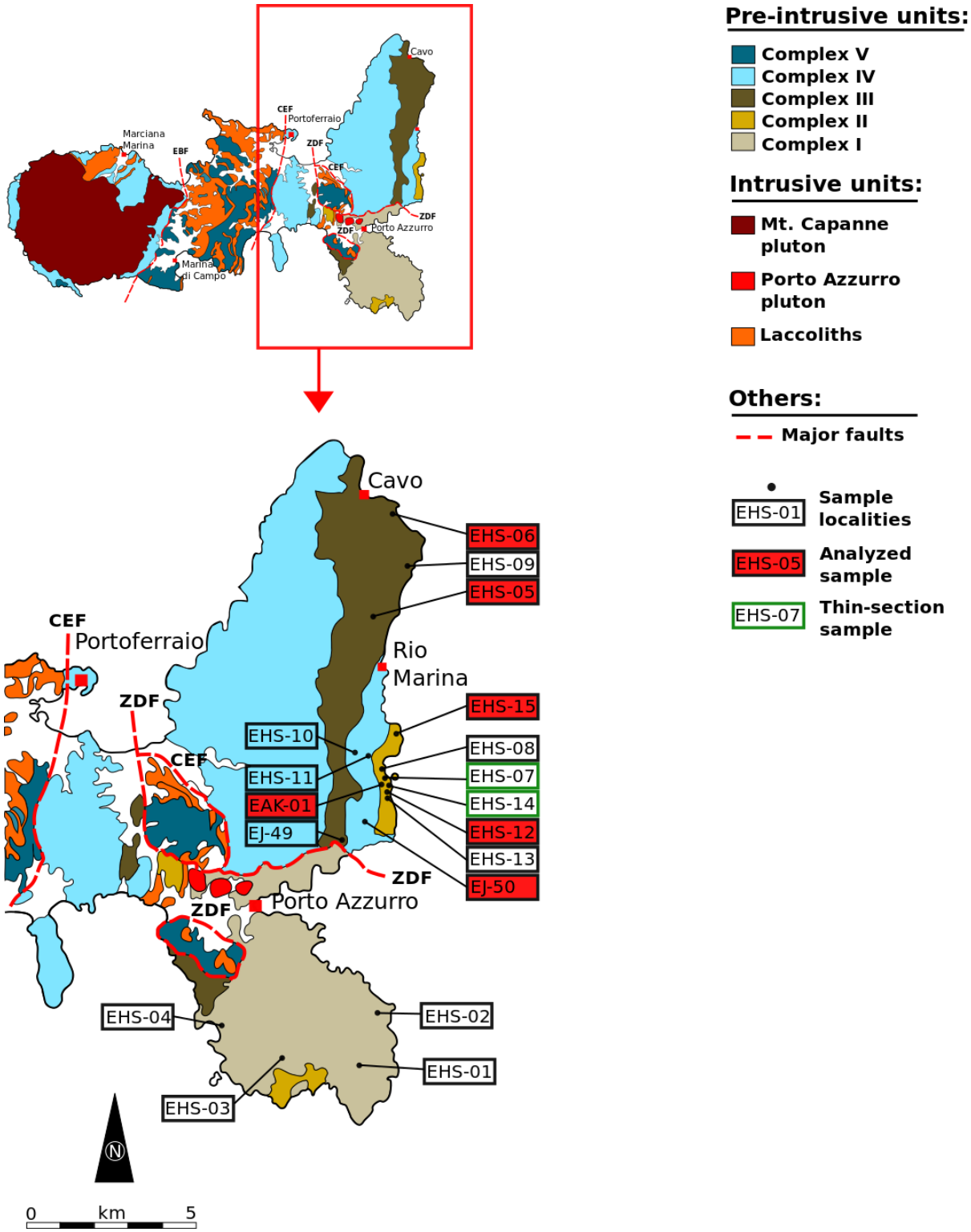

Fig. 17: Simplified map of eastern Elba showing all sample localities. Sample numbers with green borders represent samples obtained only for thin-sections. Red boxes refer to samples that were used for U/Pb zircon dating. The map is modified after Westerman et al. (2003).

Table 2: Lithology, locality descriptions and GPS coordinates for all samples that were obtained and processed. A more detailed outcrop description is shown in Appendix 1.

Sample	Lithology	Complex	Locality description	Coordinates
EAK-01	Blackish quartzites and phyllites	II	Roadcut SW of Isolotto d'Ortano	32T 0616902 UTM 4738349
EHS-01	Mt. Calamita Schist	I	Outcrop along tennis-field	32T 0616253 UTM 4730584
EHS-02	Mt. Calamita Schist	I	Roadcut on E-side of Mt. Calamita Promontory	32T 0616977 UTM 4731947
EHS-03	Mt. Calamita Schist	I	Roadcut on SW-side of Mt. Calamita Promontory	32T 0614251 UTM 4730877
EHS-04	Quartz and mica-rich lens in the Mt. Calamita Schist	I	Coastal outcrop	32T 0612544 UTM 4731645
EHS-05	Verruca Formation	III	Upper parts of the Rio Marina Mines	32T 0616219 UTM 4742620
EHS-06	Rio Marina Formation	III	Beach outcrop Le Fornacelle	32T 0617267 UTM 4745421
EHS-07	Quartzitic lens in Capo d'Arco Schist	II	Coastal outcrop between Ortano Beach and Isolotto d'Ortano	32T 0617039 UTM 4738538
EHS-08	Capo d'Arco Schist	II	Coastal outcrop between Ortano Beach and Isolotto d'Ortano	32T 0616993 UTM 4738663
EHS-09	Verruca Formation	III	Cliff at Topinetti Beach	32T 0617494 UTM 4743719
EHS-10	Rio Marina Formation	III	Roadcut in Ortano Valley	32T 0615865 UTM 4739541
EHS-11	Phyllites and metasiltstones	II	Roadcut in Ortano Valley	32T 0616257 UTM 4739320
EHS-12	Quartzitic phyllite (Capo d'Arco Schists)	II	Coastal outcrop south of Isolotto d'Ortano	32T 0617163 UTM 4738281
EHS-13	Capo d'Arco Schists	II	Coastal outcrop south of Isolotto d'Ortano	32T 0617128 UTM 4738245
EHS-14	Pyroxene-rich vein in Capo d'Arco Schists	II	Coastal outcrop south of Isolotto d'Ortano	32T 0617158 UTM 4738348
EHS-15	Biotite-rich micaschist (Capo d'Arco Schists)	II	Coastal outcrop NE of Ex. Vedetta	32T 0617443 UTM 4739411
EJ-49	Verruca Formation	III	Outcrop close to the contact to Rio Marina Formation	32T 0615659 UTM 4736837
EJ-50	Phyllites and metasiltstones	II	100 m SW from entrance of gate to Capo d'Arco Residence	32T 0616394 UTM 4737507

4.2 Sample preparation

4.2.1 Crushing and mineral separation

Mineral separation and sample preparation were carried out at the University of Bergen. The samples were crushed with a Fritsch Pulverisette 13 discmill (Fig. 18a). Particles larger than 315 μm were removed by sieving. The heavy minerals in the fraction smaller than 315 μm were concentrated using a Holman-Wilfley shaking table (Fig. 18b). The purpose of this step was to remove dust from the crushing. The dust was included in fraction 3 and removed. Fraction 1 and 2 were saved, but only fraction 1 was processed further as this was the one that included zircons.

The heavy fractions from the shaking table were subjected to magnetic separation (Fig. 18c). First, the ferromagnetic minerals were removed by a hand magnet. Further on, the Frantz Magnetic Separator was used in order to remove weakly ferromagnetic minerals, such as hematite. A current of 0.3 A and a forward and sideways tilt of 15° was used. The remaining fraction of the sample was then separated further with the heavy-liquid Sodium Polytungstate (SPT), setting the density to $2.80 - 2.90\,\mathrm{g/cm^3}$ (Fig. 18d). In the SPT liquid, quartz ($2.66\,g/cm^3$) and feldspars ($2.55-2.75\,g/cm^3$, depending on composition) will float, while zircons ($4.60 - 4.70\,g/cm^3$) and apatites ($3.10 - 3.20\,g/cm^3$) will sink. Both fractions were thoroughly rinsed with deionized water. Next, the heavy minerals were again subjected to magnetic separation. In order to remove even weaker magnetic minerals than previously, a current of 1.2 A and the same tilt was used. Finally, a second heavy-liquid, di-iodomethane (DIM), was used in order to separate the apatites from the zircons (Fig. 18e). Due to its density of $3.31\,\mathrm{g/cm^3}$, the zircons will sink and the apatites will float. All fractions were rinsed with acetone.

4.2.2 Mount preparation

After the mineral separation, the zircons were handpicked. Because some of the samples did not contain enough zircons, 7 samples were selected for further studies. Metamict grains were not selected during the handpicking. 250-300 grains were picked for each sample. By considering a worst-case scenario, Vermeesch (2004) suggests that at least 117 grains should be analysed in a detrital study in order to be 95% confident that all zircon populations are covered.

Subsequently, the samples were embedded in Buehler epoxy and ground with SIKA powders of $800\,\mu m$, $1000\,\mu m$ and $1200\,\mu m$. This was done in order to split the zircons in half. Finally, the mounts were polished with a diamond paste of $6\,\mu m$ and aluminum oxide powder of $0.05\,\mu m$, in order to get a polished surface that is suitable for analyses.

4.2.3 Cathodoluminescence imaging

Cathodoluminescence (CL) imaging was done in order to reveal the internal structure of the zircons. Prior to the CL-imaging, all mounts were coated with carbon. The zircons were photographed on a Zeiss Supra 55VP Scanning Electron Microscope, equipped with a CL detector, at the University of Bergen.

The zonation shown in CL-imaging can be used to distinguish between magmatic and metamorphic events in the grain. It is therefore desirable to use cathodoluminescence imaging to determine the ablation lines for the LA-ICPMS. Because mixed ages are not wanted, the ablation lines were selected in parts of the grain that are interpreted as being associated with the same magmatic or metamorphic event, but also so that fractures and inclusions were avoided. Cathodoluminescence images were also taken after the laser ablation for some of the characteristic grains in order to check the ablation lines.

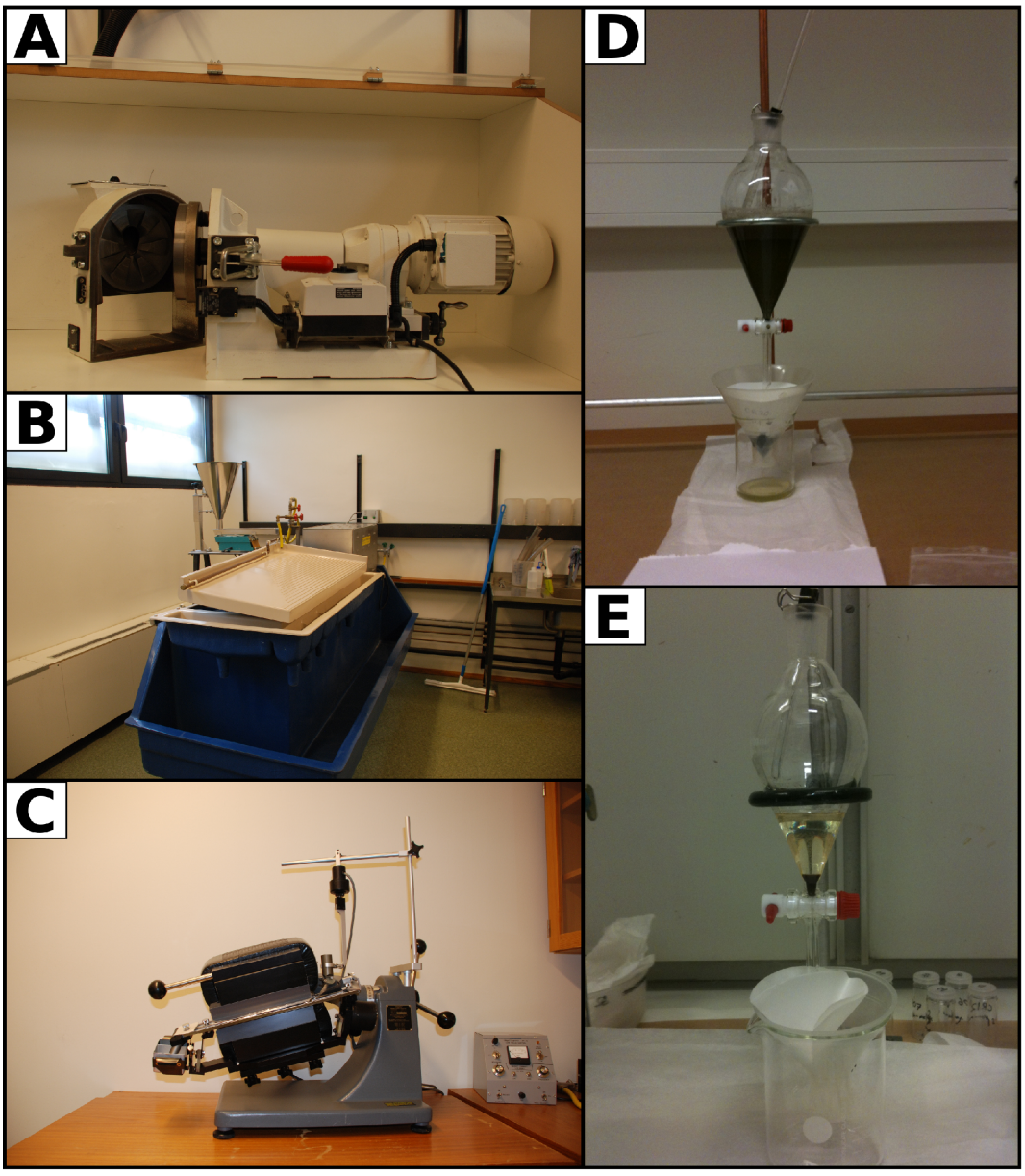

Fig. 18: The different stages in the crushing and mineral separation process. **a)** Fritsch Pulverisette 13 discmill **b)** Holman-Wilfley shaking table **c)** Frantz Magnetic Separator **d)** Heavy-liquid separation with SPT (Photo by C. Rønnevik) **e)** Heavy-liquid separation with DIM (Photo by C. Rønnevik).

4.3 Detrital zircon analysis

4.3.1 LA-ICPMS analysis

This study presents U/Pb analyses of zircons obtained by LA-ICPMS at the University of Bergen, following the method described in Košler et al. (2002). The sample mounts were cleaned first with 5% HNO_3, then in ultrasonic bath in de-ionized water prior to the analyses. The analysed grains and shot-lines were selected on the basis cathodoluminescence images and imaging in reflected light. The number of analysed zircons in the different samples are summarized in table 3. Due to time constraints, samples from the Ortano, Acquadolce and Monticiano-Roccastrada units were prioritized on expense of the samples from the Mt. Calamita Schists.

The Thermo-Finnigan Element 2 sector field ICPMS coupled with a 193 nm ArF Excimer Resonetics RESOlution M-50 LR laser was used to measure the Pb/U and Pb isotopic ratios in the zircons (Fig. 19a and 19b). The sample introduction system was modified to enable simultaneous nebulisation of the laser ablation of the solid sample and a tracer solution (Horn et al., 2000). The tracer solution consisted of natural Tl ($^{205}Tl/^{203}Tl = 2.3871$; Dunstan et al., 1980), ^{209}Bi and enriched ^{233}U and $^{237}Np > 99\%$). The tracer solution was calibrated against the Plešovice standard (337 Ma; Sláma et al., 2008) and aspirated to the plasma in an argon-helium carrier gas mixture. The laser produced a energy density of approximately $5 - 7\,^{J}/_{cm^2}$ with a repetition rate of 5 Hz. The sample was placed in a Laurin two-volume sample cell which was mounted on a computer-driven motorised stage of a microscope (Fig. 19c). During the ablation, the stage was moved beneath the stationary laser beam to produce a linear raster of approximately 19x60 μm in the sample. Each acquisition consisted of a 35 second measurement of the analytes in the aspirated solution (particularly $^{203}Tl-$, $^{205}Tl-$, ^{209}Bi, ^{233}U and ^{237}Np) and the gas blank. This was followed by 110 seconds of measurement of U and Pb signals from the zircon, as well as the continous signal from the aspirated solution. A 45 second wash-out was done in the end. The data from the first 145 seconds were acquired in time resolved-peak jumping-pulse counting mode with 1 point measured per peak for masses 202 (flyback), 203 and 205 (Tl), 206 and 207 (Pb), 209 (Bi), 233 (U), 237 (Np), 238 (U), 249 (^{233}U oxide), 253 (^{237}Np oxide) and 254 (^{238}U oxide).

During the LA-ICPMS analyses two different age standards were used prior to, during and after the analyses of the unknown zircons. The standards used were the GJ-1 and Plešovice standards. The GJ-1 zircon is a large zircon ($\sim 1\,cm$) that has an age of $609\,Ma$ (Jackson et al., 2004).The Plešovice zircon has a size of $1 - 6\,mm$ and has, based on ID-TIMS, SIMS and LA-ICPMS, an age of $337\,Ma$ (Sláma et al., 2008). For the present study, the Plešovice standard has been used as the primary standard as this is close to the expected age of the grains.

Prior to the analyses of the samples, the GJ-1 and Plešovice standards were analysed two times with spot sizes of $26\,\mu m$ and $19\,\mu m$, respectively. The unknowns were abladed with a spot size of $19\,\mu m$. After about every 15 analyses of the sample, a new round of standards were analysed. During this stage, the GJ-1 and Plešovice standards were analysed once. At the end of each session, the GJ-1 standard was analysed twice and the Plešovice zircon was analysed once with the same spot sizes as earlier. The analysed standards yielded mean ages of 596±2 Ma and

338±1 Ma, respectively. The tune parameters for the ICPMS are summarized in Appendix 2.

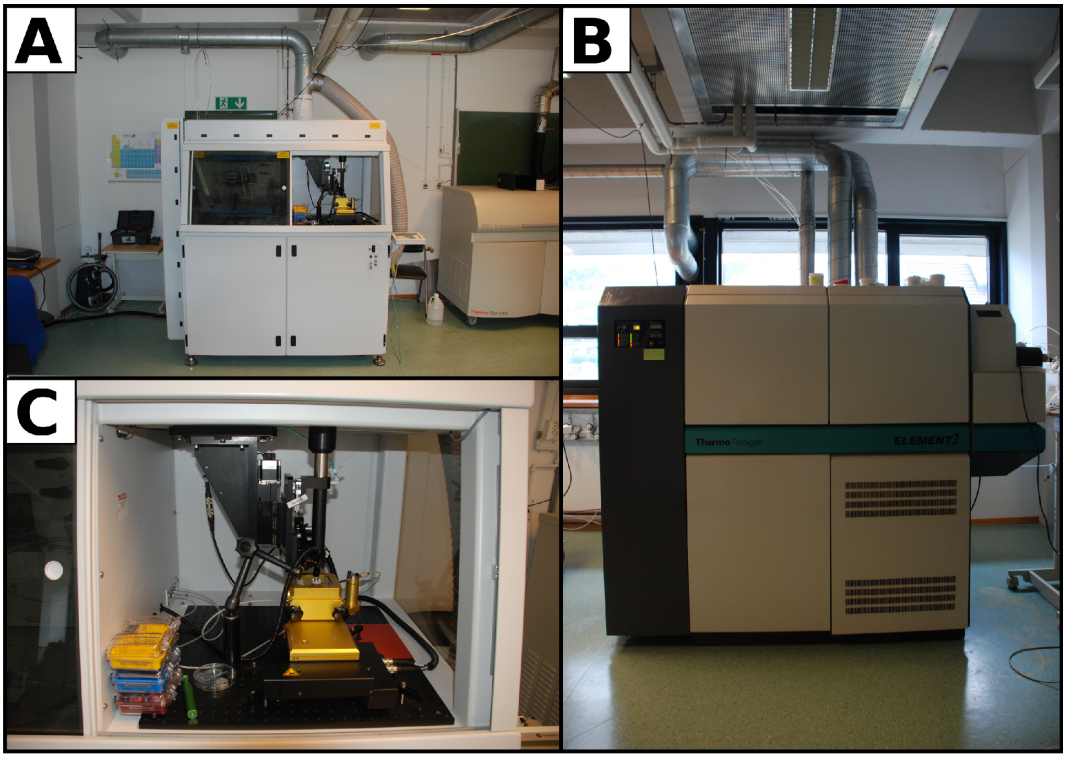

Fig. 19: Instruments used for U/Pb analyses at University of Bergen. **a)** 193 nm ArF Excimer Resonetics RESOlution M-50 LR laser; **b)** Thermo-Finnigan Element 2 sector field ICPMS; **c)** Laurin two-volume sample cell.

4.3.2 Data processing

The raw data were corrected for dead time of the electron multiplier and processed in the spreadsheet-based program Lamdate (Košler et al., 2002). The processing involved selecting limits for the gas blanks and the signal in each analysis. The limits of the signal were defined according to the stability of the signal, as well as trying to obtain as low relative standard errors (RSE) as possible. No common Pb correction was applied to the data. The data reduction is described in detail in Košler et al. (2002) and Košler and Sylvester (2003). Isoplot (Ludwig, 2012) was used for further data processing. Isoplot was used to plot concordia-diagrams of the standards, calculating the concordant ages and the probability of concordance of the different standards in each session. The standard reproducibility was calculated for all standards.

The ages of the unknown samples were calibrated against the the known ages for the standards. Grains fulfilling at least one of the following criteria were filtered out:

1. Grains that were more than 10% discordant.
2. 2σ of the isotopic ratio exceeded 20% (for either $\frac{^{207}Pb}{^{206}Pb}$, $\frac{^{207}Pb}{^{235}U}$ *or* $\frac{^{206}Pb}{^{238}U}$).

After the process of filtering grains, Isoplot was used to create probability density plots and histograms for the remaining grains. Isoplot was also used to make concordia-diagrams for the unknown samples.

4.3.3 Statistics

In detrital studies, the main goal is to determine the source of the sediments. In order to draw statistically sound conclusions, it is important that enough zircons are analysed. A quantity between 50 and 83 zircons has been proposed by Morton et al. (1996), Whitehouse et al. (1997) and Fernández-Suárez et al. (2000). To make sure that all zircon populations are analysed, Košler et al. (2002) suggest that 80-100 grains should be dated while Vermeesch (2004) suggests a minimum of 117 grains, based on a worst-case scenario. Andersen (2005) suggests that the probablity of not detecting a given population of zircons are given by Eq. 2. In this equation, p_{n_i} refers to the probability of detecting a given quantity of zircons from population i and X_i refers to the abundance of the given zircon population in the sediment.

$$p_{n_i=0} = (1 - X_i)^n \tag{2}$$

By developing Eq. 2 into Eq. 3, Andersen (2005) proposes that the detection limit is be given by Eq. 3. In this equation, the abundance limit of populations (X_L) is given by a probability of the detection limit (p_L).

$$X_L = 1 - (1 - p_L)^{1/n} \tag{3}$$

The number of zircons given in table 3 are the amount of grains that are left after data processing. The criterias for the data filtering are described in section 4.3.2. By comparing the number of analysed grains in table 3 by the numbers given by e.g. Vermeesch (2004), it can be seen that the number of analysed zircons is significantly lower. However, the number of analysed zircons given in table 3 are all within the range that are accepted by Morton et al. (1996), Whitehouse et al. (1997) and Fernández-Suárez et al. (2000), although, in some cases, the number of accepted grains are significantly lower than suggested.

Table 3: The probability of not detecting zircons from a population i ($p_{n_i=0}$) and the limit of abundance of a population (X_L). All numbers are calculated based on Eq. 2 and 3 given by Andersen (2005). I.e. if the abundance of a given zircon population in sample EAK-01 is 5%, the probability of not detecting the population is 1.7%. Also, the relative population size of the smallest population has to be at least 3.7% in order to be 95% confident that the population is discovered.

Sample	Lithology	Analysed grains	Accepted grains	$p_{n_i=0}$ (%) for different X_i (%)			X_L for different p_L		
				1	2	5	95	90	80
EAK-01	Blackish quartzites and phyllites	143	80	44.8	19.9	1.7	0.037	0.028	0.020
EHS-05	Verruca Formation	105	50	60.5	36.4	7.7	0.058	0.045	0.032
EHS-06	Rio Marina Formation	107	21	81.0	65.4	34.1	0.133	0.104	0.074
EHS-12	Quartzitic phyllite (Capo d'Arco Schists)	68	28	75.5	56.8	23.8	0.101	0.079	0.056
EHS-15	Biotite-rich micaschist (Capo d'Arco Schists)	107	54	58.1	33.6	6.3	0.054	0.042	0.029
EJ-50	Phyllites and metasiltstones	152	62	53.6	28.6	4.2	0.047	0.036	0.026

p_{n_i}: Probability of not detecting a given quantity of zircons in population i (X_i)
X_i: Abundance of given zircon population in sediment
X_L: Relative population size of the smallest population that is detected
p_L: Probability of detecting the smallest population

5 Results

5.1 Capo d'Arco Schist (EHS-12 and EHS-15)

At least two different varieties of the Capo d'Arco Schists can be distinguished. These are the biotite-rich micaschist (sample EHS-15) and the overlying quartzitic phyllite (samples EHS-12 and EHS-13). Detrital zircon ages, thin-section descriptions and zircon characterization from both varieties are presented separately below. These two samples are both from the quartzitic phyllite. In addition, the micaschist is crosscut by pyroxene-rich veins on the cm- to dm-scale. Sample EHS-14 represents sample from one of these veins and is described together with EHS-15.

EHS-15 - Micaschist

The biotite-rich micaschist has a well-developed foliation, both on the meso- and microscale (Fig. 20). Mono-mineralogic bands of quartz with grains up to 0.5 mm and polymineralogic bands of sericite, fine-grained biotite and quartz/albite can be observed on the microscale. Simple and polysynthetic twinning is observed in the albites. The polymineralogic bands also contain single, larger crystals of white mica. Opaque minerals are present as accessory phases.

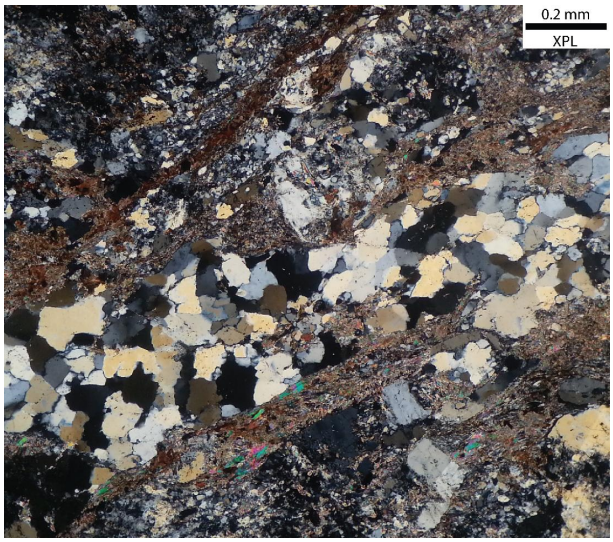

Fig. 20: Thin-section photograph of the biotite-rich micaschist, showing the banding of the quartz/feldspars and the sericitic matrix. Larger crystals of white mica are also observed. Sample EHS-15, cross-polarized light, 10x magnification.

The veins that are crosscutting the biotite-rich micaschists have a metaporphyritic texture. The groundmass in these consists of plagioclase and relict pyroxenes. Elongated crystals of plagioclase appear in parts of the groundmass. The rest of the groundmass appears very altered compared to the plagioclases. Phenocrysts of plagioclase with exsolution lamellae, orthopyroxene and aggregates of large quartz grains are present in the sample. Some of the feldspars include possible columnar grains of apatite. Biotite can be observed in smaller amounts. Rutile are observed as an accessory mineral, and about 3% of the sample is represented by opaque minerals.

The analysed zircon grains have lengths of 100 to 270 μm and widths of 30 to 100 μm. The grains are elongated with a mean length-width ratio of 2.7. Most of the zircons are idiomorphic to subhedral, but rounded grains are also present. About 15% of the grains are fractured and 40% of the grains have inclusions. The zircons in the Capo d'Arco micaschist present a great variety of zoning (Fig. 21). The majority of the grains have oscillatory zoned rims with a more complex texture in the core. The cores vary from complex to elongated zoning, like typical dioritic-granodioritic zoning presented in Corfu et al. (2003). Most of the grains show well-defined boundaries between the core and the rim, indicating multi-stage growth of the zircons.

A total amount of 107 grains were analysed in sample EHS-15. 60 of these grains were relatively concordant and precise and passed the quality filters applied to the data. The zircons have an age span between 400 and 1040 Ma. A probability density plot and histogram are shown in Fig. 22. A single grain gave an age of 1040 Ma. Also, some grains scatter between 450 Ma and 700 Ma, but the majority of grains cluster around 430 Ma.

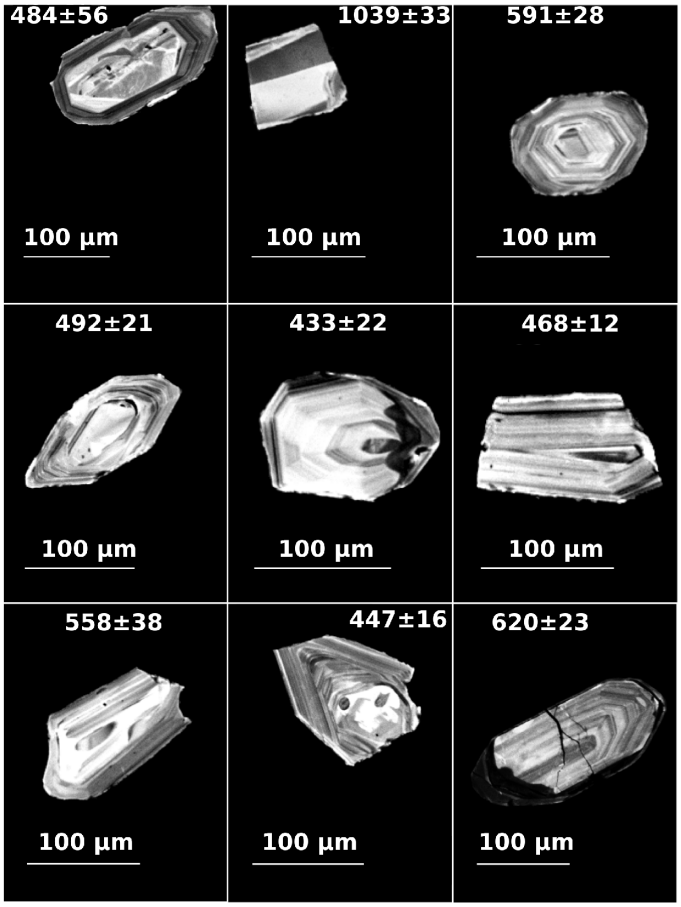

Fig. 21: Cathodoluminescence imaging of some of the characteristic grains from the biotite-rich micaschist. Oscillatory zoning and c-axis parallel zoning is dominating the sample.

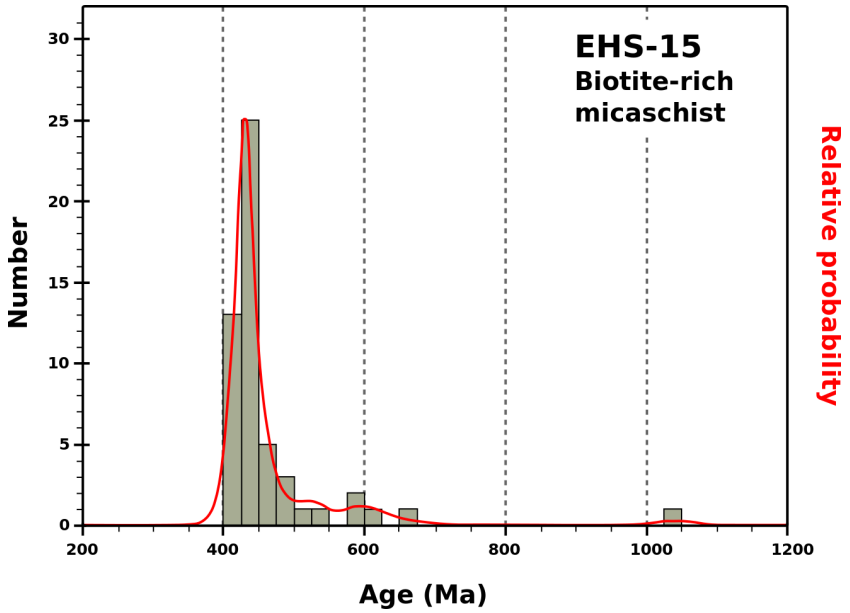

Fig. 22: Probability density plot and histogram for the biotite-rich Capo d'Arco Schist (sample EHS-15), showing a dominating peak around 430 Ma. Additional grains fall between ca. 450 and 700 Ma and one zircon yielded an age of 1040 Ma.

EHS-12 - Quartzitic phyllite

On the microscale, the quartzitic phyllite only differs slightly from the biotite-rich micaschist. This sample contains less biotite and lacks the well-developed foliation that can be observed in the micaschist (Fig. 23). Some of the bands that are observed contain only quartz, but most of the bands consist of a mixture of quartz (smaller than 0.5 mm), feldspar, biotite, sericite and some larger white mica crystals (smaller than 0.2 mm). Many of the quartz grains look a bit diffuse and have lots of small inclusions. Rutile and opaque minerals are present as accessory minerals.

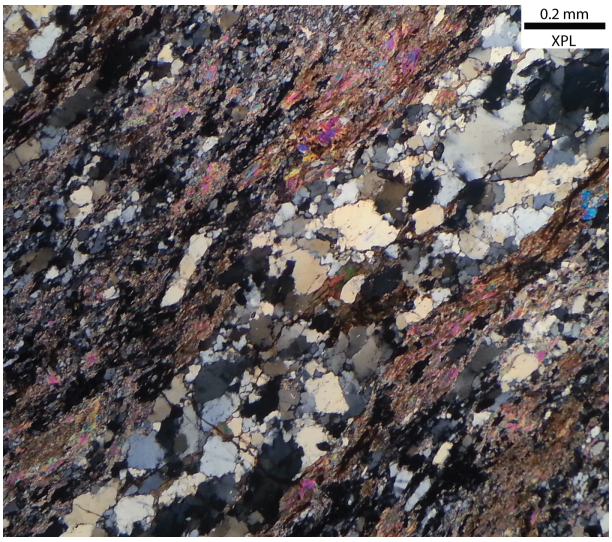

Fig. 23: Thin-section photograph of the quartzitic phyllite. Bands of quartz, feldspar, biotite and sericite are observed in the thin-section. Also, crystals of white mica (<0.2 mm) are present. Sample EHS-13, cross-polarized light, 10x magnification.

The analysed zircons have lengths between 70 and 190 μm and widths between 35 and 100 μm, giving a mean length-width ratio of approximately 2.3. Even though most grains are subhedral, some idiomorphic grains are also present. One third of the grains are slightly fractured and half of the grains contain inclusions. The zoning in EHS-12 is less prominant than in the other samples (Fig. 24). Most zircons lack cores and the zonation is, in most cases, elongated and parallel to the c-axis of the grain. In addition to this, some grains also show sector zoning, oscillatory zoning or a combination of a sector zoned core and a oscillatory zoned rim. The last may be indicating a reworked metamorphic core with a magmatic rim.

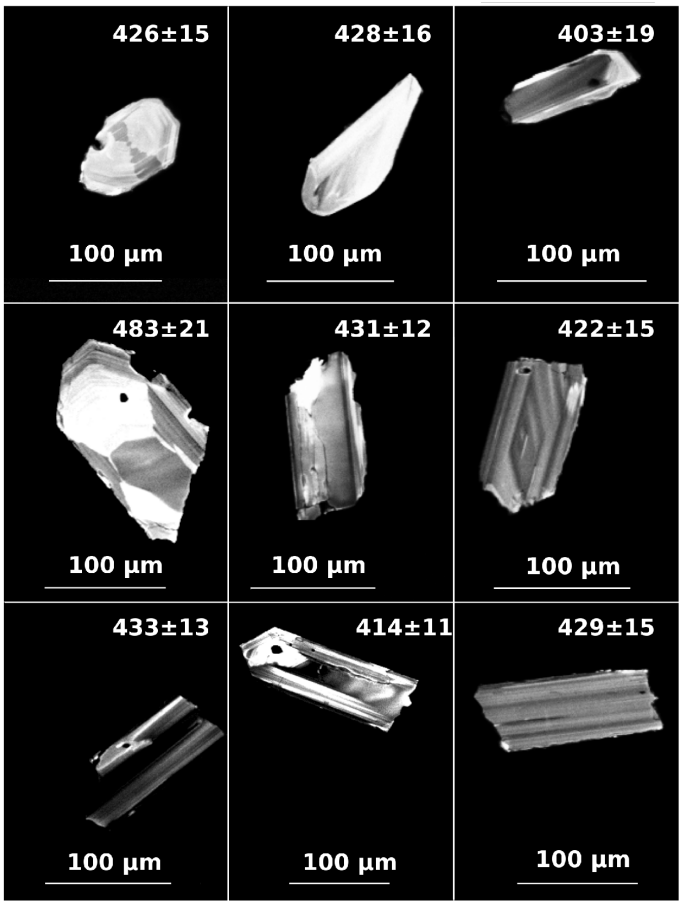

Fig. 24: Cathodoluminescence images of zircons that were analysed. C-axis parallel zoning is dominating the zircon population within sample EHS-12.

After analysing 68 zircons, only 28 grains gave concordant and precise ages that passed the quality filtering of the data. These grains show a unimodal, Gaussian distribution with ages between 397 and 451 Ma. The peak of the probability density curve is located at ca. 420 Ma (Fig. 25).

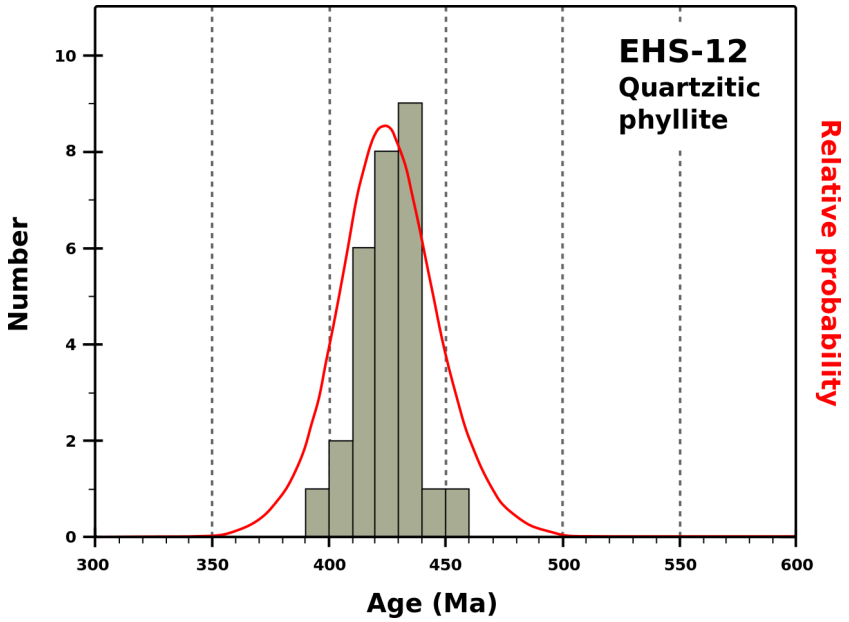

Fig. 25: Probability density plot and histogram for the quartizitic phyllite variety of the Capo d'Arco Schists. The probability density plot shows a Gaussian age distribution that indicates only one zircon population with a peak around 420 Ma.

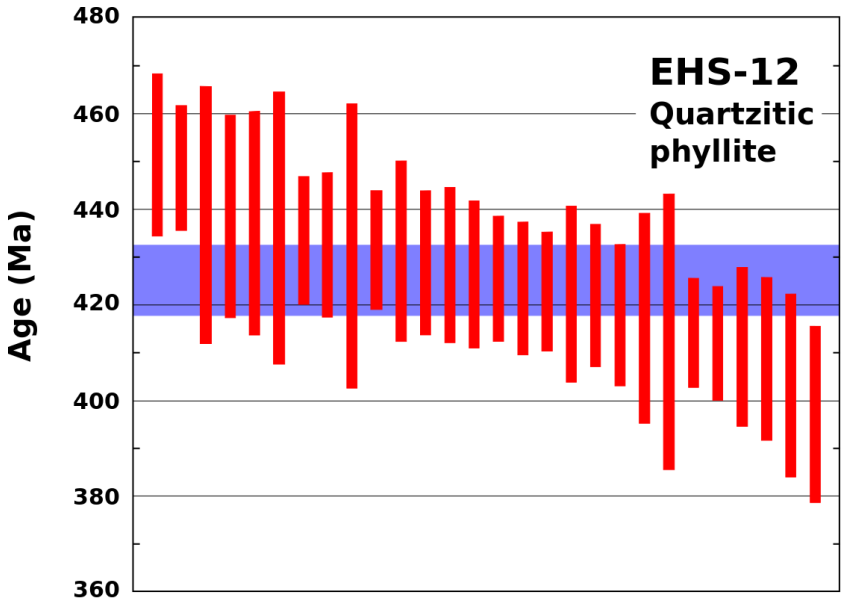

Fig. 26: Crystallization age of the Capo d'Arco Schist with a 95% confidence. The crystallization age is calculated from the TuffZirc algorithm from Ludwig and Mundil (2002). Box heights represent 1σ and the blue belt is interpreted as presenting the calculated crystallization age with errors.

Because of the unimodal distribution of the zircons (Fig. 25), the simple zoning and the lack of cores, the zircons are interpreted to be of magmatic origin. The TuffZirc algorithm (Ludwig and Mundil, 2002) in Isoplot has been used to calculate an age of 422±8 Ma that is interpreted as the crystallization age of the protolith to the quartzitic phyllite (Fig. 26).

5.2 Blackish quartzites and phyllites (EAK-01)

The blackish quartzites and phyllites show only a weak foliation in thin-section (Fig. 27). The sample contains mainly sericite and quartz, but also smaller amounts of feldspar and biotite. The feldspars are generally altered to sericite. 2-3% of the grains are opaque minerals that occur in clusters or veins. Quartz grains often contain inclusions of minerals with high interference colours, but these are too small to be identified. Also, an unidentified accessory mineral that is fibrous and radially growing is observed. This mineral has a colourless to brownish pleochroism and does not change colour in cross-polarized light.

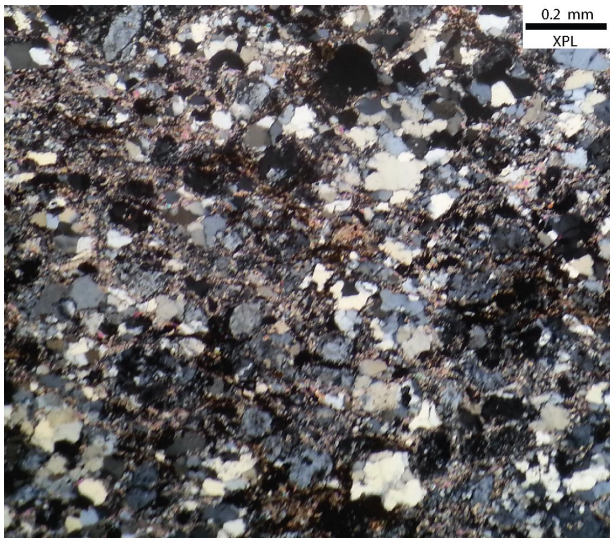

Fig. 27: Thin-section photograph of the blackish quartzites and phyllites, showing mainly quartz and sericite. Smaller amounts of biotite and feldspar are also present in the sample. Sample EAK-01, cross-polarized light, 10x magnification.

The analysed zircons have lenghts between 90 and 330 μm and widths between 50 and 150 μm. This gives an average length-width ratio of 1.8. Subhedral and anhedral grains are abundant in this sample. Some grains are subrounded, but the majority are rounded. About 40% of the analysed grains are fractured. Approximately one third of the zircons have inclusions. The internal structure for the zircons is dominated by a zonation that is parallel to the c-axis of the grain, but many grains additionally have oscillatory zoned rims (Fig. 28). Most of the grains that are older than 600 Ma show sector zoning throughout the whole grain, or oscillatory zoned tips or rims combined with sector zoned cores. In addition to this, homogenous or weakly zoned grains are also present in the sample.

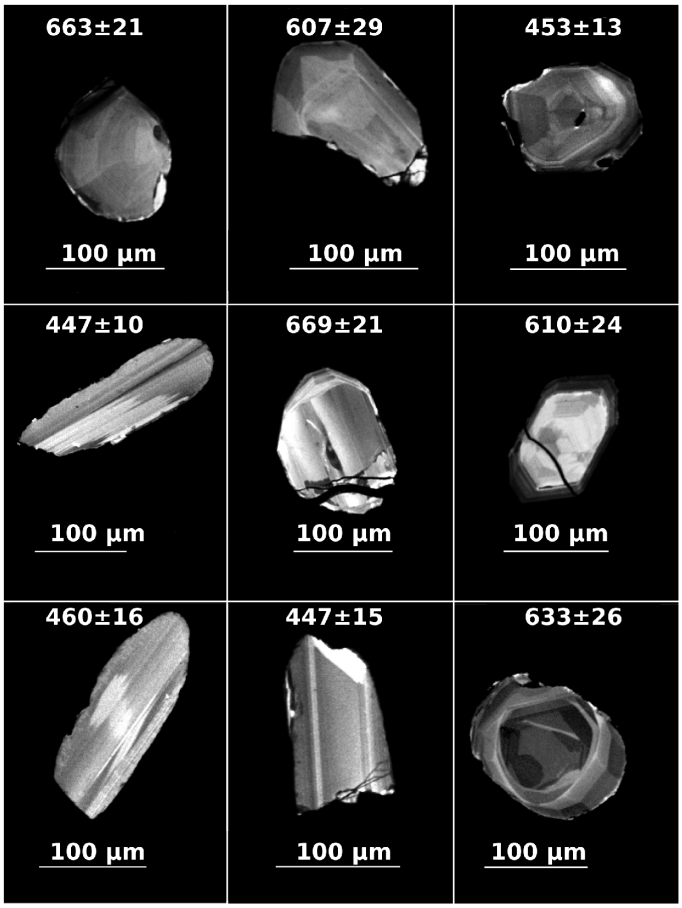

Fig. 28: Cathodoluminescence images of the zircons in the blackish quartzites and phyllites. Zircons older than about 600 Ma show clearly sector zoned cores or a combination between sector zoned cores and oscillatory zoned tips.

Of a total of 143 analyses of the blackish quartzites and phyllites, 80 grains passed the quality check. The ages of the zircons reach from 386 to 1005 Ma, but 89% of the grains have an age between 386 and 500 Ma. The probability density plot (Fig. 29) shows a bimodal distribution with the dominating peak around 450 Ma and a smaller, secondary peak around 620 Ma. Single grains gave Neoproterozoic ages at ca. 810 Ma, 960 Ma and 1000 Ma.

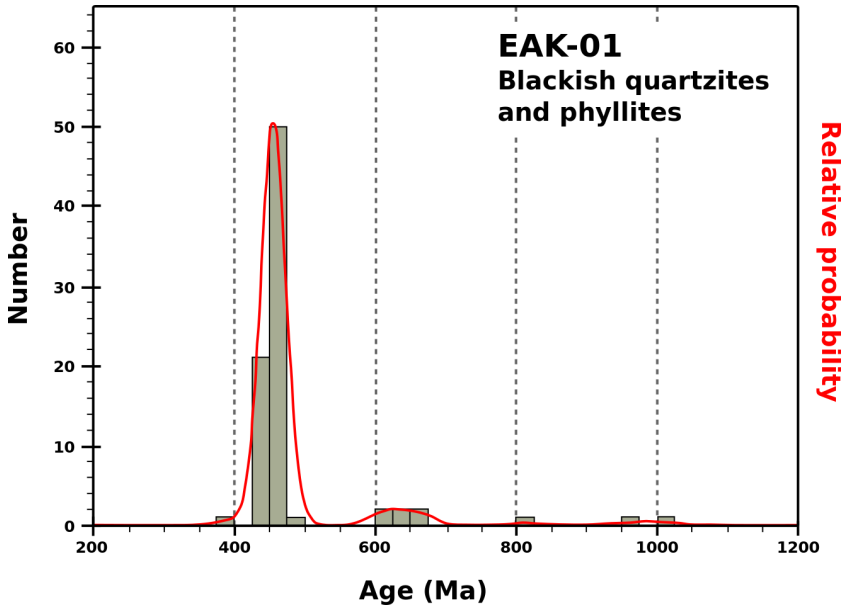

Fig. 29: The histogram and probability density diagram of the blackish quartzites and phyllites show a bimodal age distribution with a main peak around 450 Ma and 620 Ma. Additionally, single grains are present at ca. 810 Ma, 960 Ma and 1000 Ma.

5.3 Phyllites and metasiltstones (EJ-50)

The phyllites and metasiltstones appear as a foliated rock which is banded at microscale. Some bands consist of fine-grained quartz with opaque minerals in between, while other bands are composed mainly of sericite and larger crystals of white mica, biotite and chlorite (Fig. 30). Opaque minerals are present as accessory minerals. Some veins can also be observed around areas where the rock appears oxidized.

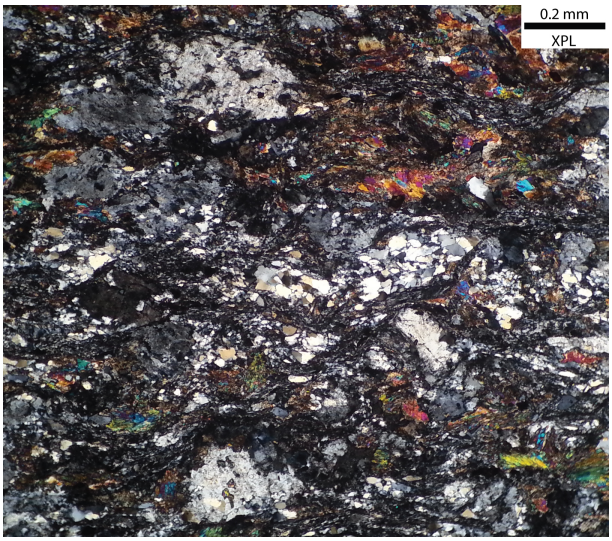

Fig. 30: Thin-section photograph from sample EJ-50. Banding on microscale can be observed. Some of the bands consist of fine-grained quartz and opaque minerals, while others mainly consist of sericite, chlorite and biotite. Sample EJ-50, cross-polarized light, 10x magnification.

152 zircons were analysed from this sample, and 62 of these were accepted after the data processing and filtering. The ages of the zircons in this sample fall mainly between 251 and 2691 Ma. However, there is also one concordant grain with an age of 32 Ma. In addition to this, 44 grains yielded $^{238}U/^{206}Pb$-ages between 29 and 71 Ma. Based on only the difference in $^{238}U/^{206}Pb$- and $^{207}Pb/^{206}Pb$-ages, these grains appear as strongly discordant, thus they were rejected in the standard data filtering. It is likely, that the high discordancy is due to the unreliability of the $^{207}Pb/^{206}Pb$-ages for very young samples. Thus, a probability of concordance has been calculated following Ludwig (2012), and all analyses with a probability of concordance above 0.01 have been accepted.

A probability density plot with histogram for the grains older than 100 Ma is presented in Fig. 31, showing a polymodal age distribution. The most dominant age group, represented by 90% of the grains, shows a continuous distribution between 250 and 1000 Ma with the largest peak at 460 Ma. It also includes peaks around 280, 610 and 800 Ma. In addition to this, three grains cluster around 1850 Ma and single zircons gave ages of ca. 2100 Ma and ca. 2700 Ma.

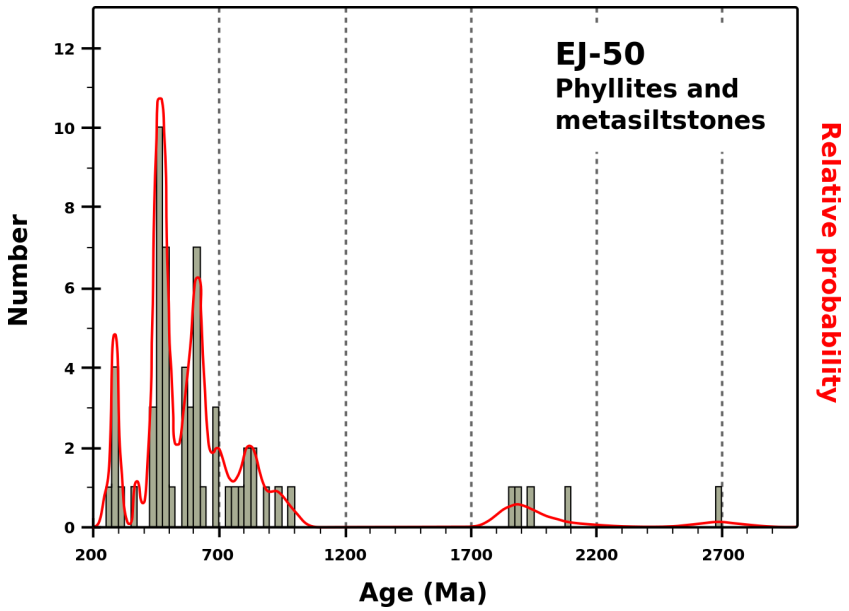

Fig. 31: Probability density plot and histogram showing the polymodal age distribution in the phyllites and metasiltstones. In addition to these ages, a group of zircons with ages between 28.5 and 71 Ma is present in the sample (Fig. 33 and 34). Here, distinct peaks are present at ca. 280 Ma, 460 Ma, 610 Ma, 800 Ma and 1850 Ma.

The analysed zircons with ages above 100 Ma have lengths between 80 and 200 μm and widths between 40 and 125 μm, giving a mean length-width ratio of 2. The concordant grains are mainly subhedral and, in some cases, subrounded to rounded. The internal structure of the concordant grains appears complex with oscillatory zoning (Fig. 32).

The population of young grains that were excluded in the standard data processing appears as zircons with a length between 70 and 190 μm and a width of 30 to 100 μm. This results in a length-width ratio of 1.5-2. The majority of the grains are idiomorphic and free of inclusions and fractures (Fig. 32). The zircons show mainly oscillatory zoned rims, which are more dominant than in the older, concordant zircons. Small, unzoned cores can be found in some zircons. The

morphology, age and internal structure is markedly different from the older grains and points clearly towards a magmatic origin, possibly with recycled cores.

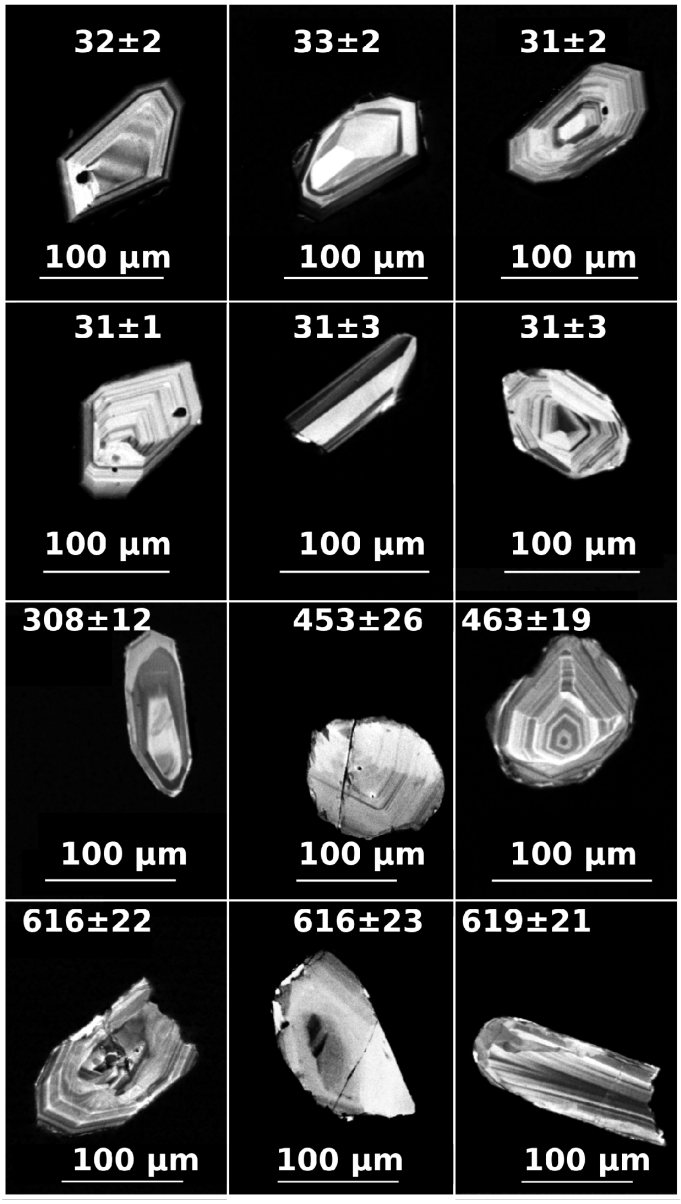

Fig. 32: Cathodoluminescence images of selected zircons in the phyllites and metasiltstones. The young population is characterized by idiomorphic zircons with distinct, oscillatory zoning. The older grains appear more rounded and weathered around the rim of the zircon.

The grains from the young population are excluded from Fig. 31. In this subpopulation, all grains with an age younger than 80 Ma and a probability of concordance of at least 0.01 have been included. A concordia diagram of this subpopulation is shown in Fig. 33. Although these grains are interpreted to represent a magmatic source, a common concordia age could not be calculated because of the large age span. Therefore, the TuffZirc algorithm has been applied to these grains (Ludwig and Mundil, 2002). The TuffZirc algorithm excluded the two oldest grains and calculated an age of 32±1 Ma based on the rest of the grains (Fig. 34).

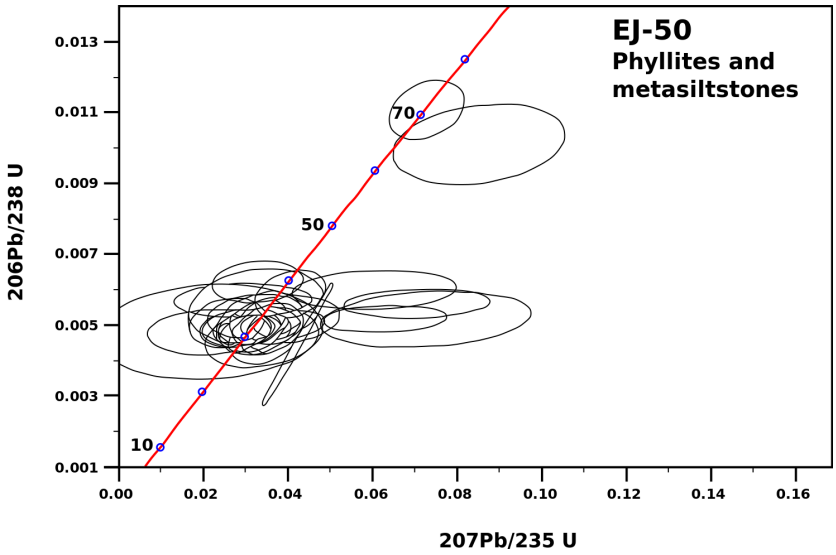

Fig. 33: Concordia diagram of the 45 youngest grains in EJ-50. 44 out of 45 zircons have discordant ages that were originally filtered out, based on the discordancy due to the unreliable $^{207}Pb/^{206}Pb$-ages. The black circles represent the discordant grains while the red circle represents the single concordant grain in this population.

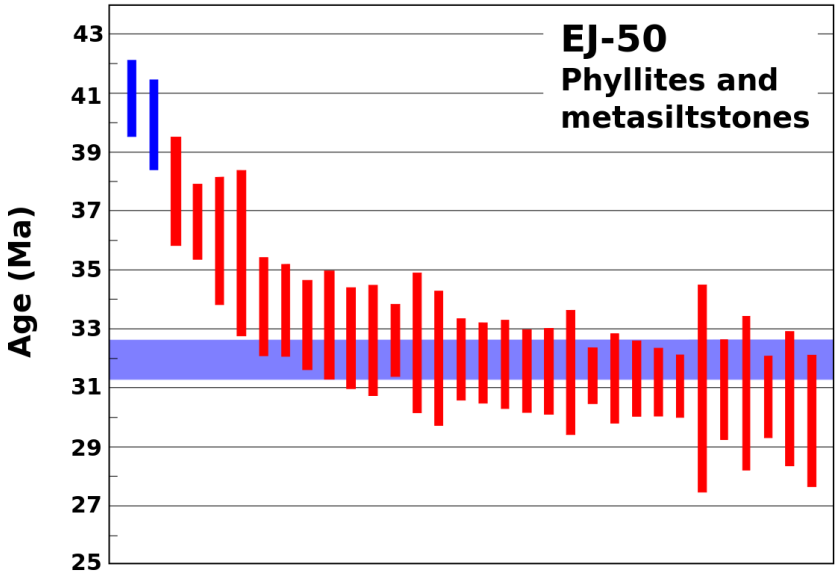

Fig. 34: Plot created by the use of the TuffZirc algorithm described by Ludwig and Mundil (2002). It is suggested by Ludwig (2012) that the red boxes represent syngenetic zircons from a magmatic event, while the blue bars may represent xenocrystic cores or grains that have experienced lead-loss. Box heights are 1σ. The age calculated by this algorithm is 32±1 Ma.

5.4 Rio Marina Formation (EHS-06)

The sample from the Rio Marina Formation was obtained from an outcrop where the lithology varied from silty on the western side to more phyllitic on the eastern side. A thin-section from the eastern side shows a well-developed foliation and a distinct open folding throughout the

whole sample (Fig. 35). The folding is also present on the mesoscale. The sample is fine-grained and appears banded on the microscale. The light bands are dominated mainly by quartz and sericite while the darker bands contain more biotite. Some crystals of white mica and opaque minerals are also present with an abundance of approximately 2% each. The sample from the silty variety is similiar to the phyllitic one with respect to the mineralogy. The matrix consists of sericite, biotite and fine-grained quartz/feldspar. Some larger quartz grains are present. Also, some white grains with high relief that may be rutile can be observed. Folding is also present in the silty sample from the western side of the outcrop, but the folding is less prominent and can only be seen in the micas.

Fig. 35: Thin-section (PPL) from the eastern side of the outcrop. A distinct open folding is present in the sample. The sample consists mainly lighter bands dominated by quartz and sericite and darker bands with a higher content of biotite. Sample EHS-06, plane-polarized light, 10x magnification.

The zircons vary in size with a length between and 60 and 215 μm and a width between 20 and 110 μm. The grains are mostly elongated with a length-width ratio of 2. The morphology of the zircons spans from well rounded to idiomorphic, possibly indicating variable amount of transportation (Fig. 36). About one third of the grains are fractured, ranging from slightly fractured to heavily fractured. 25% of the grains are broken, resulting in missing parts of the zircon. The majority of the zircons (about 75%) are free of inclusions. Oscillatory zoning is present in most of the grains, pointing towards magmatic rocks in the source region of the sediment (Corfu et al., 2003). Hence, the age given will represent the crystallization age of the source rock. Even though most of the grains show oscillatory zoning, other types of zoning can also be identified. Sector zoning is present both in whole grains and in rounded, xenocrystic cores.

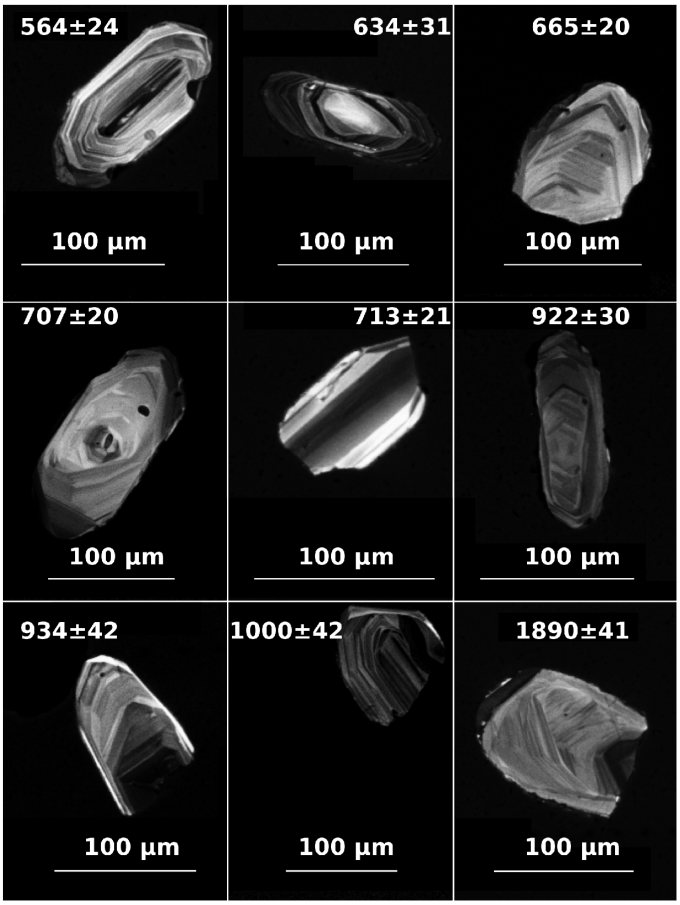

Fig. 36: Cathodoluminescence images of the zircons in the Rio Marina Formation. The zonation in the zircons are mainly oscillatory, but grains with c-axis parallel zoning are also present in the sample.

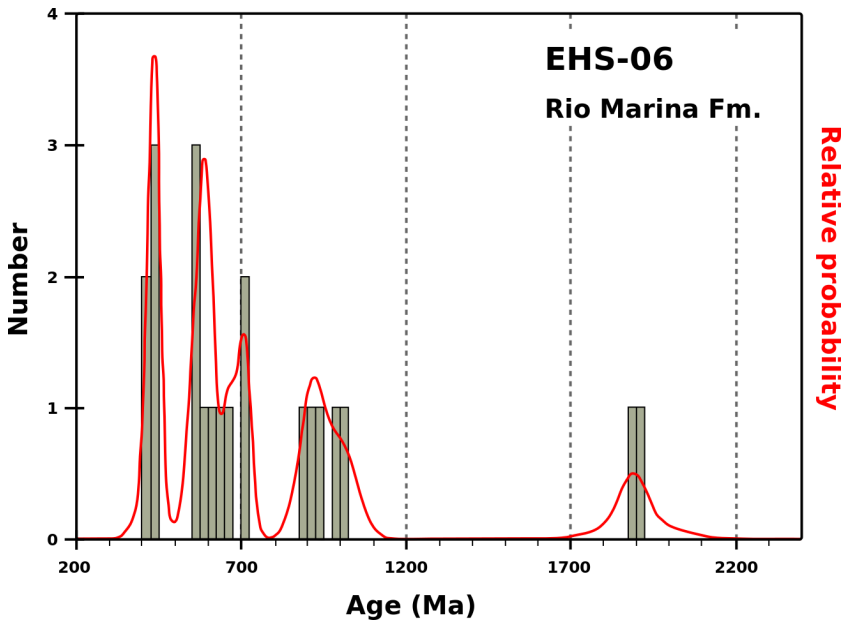

Fig. 37: The polymodal age distribution of the Rio Marina Formation presented in a probability density plot and the associated histogram indicating at least three different age populations between 433 and 1906 Ma. Probability peaks are present around 430 Ma, 590 Ma, 700 Ma, 910 Ma and 1900 Ma.

During this study, 107 grains were selected for analyses. Only 21 of these zircons were accepted during data filtering. The probability density plot for this sample (Fig. 37) shows a polymodal distribution of ages where three age groups can be distinguished. The first group comprises 71% of the grains and has an age range from 420 Ma to around 750 Ma. It includes probability peaks at approximately 430, 590 and 700 Ma, with the first as the most dominating one. The second group includes 19% of the accepted grains. This group spans from around 850 to 1050 Ma, and has an age peak at 910 Ma. The last group consists of 2 grains with ages around 1900 Ma.

5.5 Verruca Formation (EHS-05)

Sample EHS-05 consists of larger quartz grains in a sericitic matrix (Fig. 38). Also in this sample, small inclusions with high interference colours are present in the quartz, but they are too small to be identified. Minor amounts of opaque minerals and of biotite appear randomly distributed. Rutile and white mica are accessory minerals in this sample.

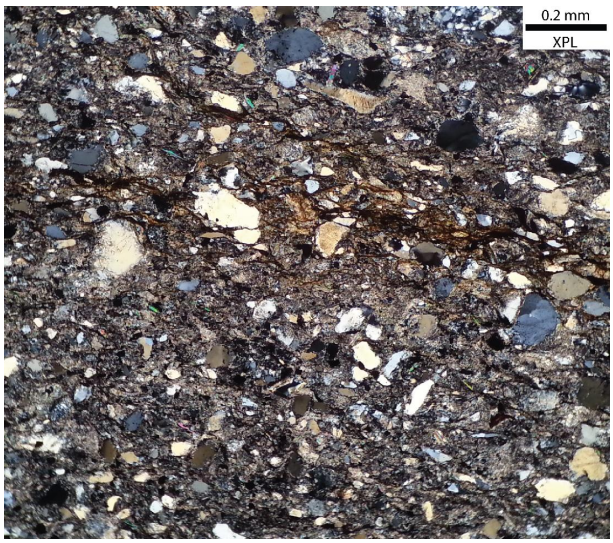

Fig. 38: Thin-section photograph of the sample from the Rio Marina Formation. Larger quartz grains in a sericitic matrix are present. Minor amounts of biotite and opaque minerals are randomly distributed. Sample EHS-05, cross-polarized light, 10x magnification.

The zircons in the Verruca Formation have lengths between 100 and 250 μm and widths between 40 and 130 μm. This gives a mean length-width ratio of approximately 2. The majority of the zircons are subhedral, but anhedral and idiomorphic grains also appear in very small amounts. 20% of the grains are fractured, while one third of the zircons have inclusions. Most of the grains show oscillatory zoning, even though sector zoning or grains with sector zoned cores and oscillatory zoned rims also occur (Fig. 39). The latter grains have a clear boundary between the core and the rim. Zircons with zoning parallel to the c-axis, with homogenous cores and zircons with less predominant zoning are present in small amounts in the sample. These grains indicate that some grains have a metamorphic origin, while others have a magmatic origin.

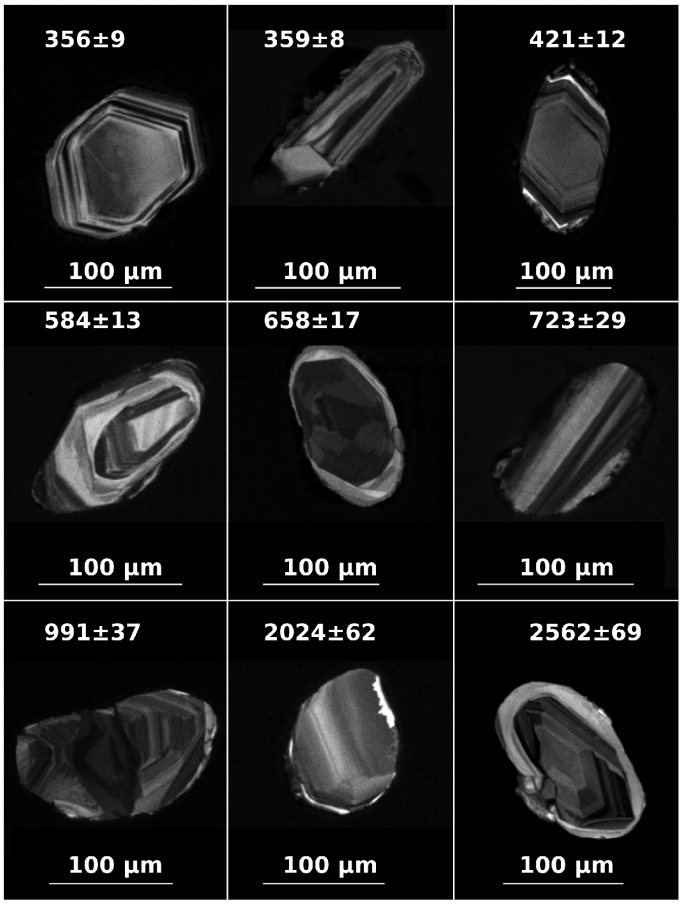

Fig. 39: Cathodoluminescence images of the zircons in the Verruca Formation. Both oscillatory zoning and c-axis parallel zoning are present in the sample. Clear boundaries between core and rim can be observed.

A total number of 105 zircons were analysed from the Verruca Formation. 50 zircons passed the data filtering. The age spans from 259 to 2562 Ma. The probability density plot with histogram for the zircons shows a polymodal population distribution with three distinctive groups (Fig. 40). 75% of the grains belong to the youngest group with an almost continuous age distribution between 250 and 1000 Ma. Several probability peaks can be observed in this group. The most dominant one is around 280 Ma, but peaks around 360, 450, 580, 680 and 940 Ma are also present in the youngest group. The second group includes 16% of the grains. This group has an age distribution between 1650 and 2050 Ma. An age peak around 1930 Ma is present in this group. The third group comprises 9% of the grains. The age distribution in this group is between 2350 and almost 2600 Ma with the probability peak around 2500 Ma. Even though the peaks in the second and third groups are small compared to the dominant peak around 280 Ma, they show that there is a small, but significant component of Paleoproterozoic zircons in the Verruca Formation.

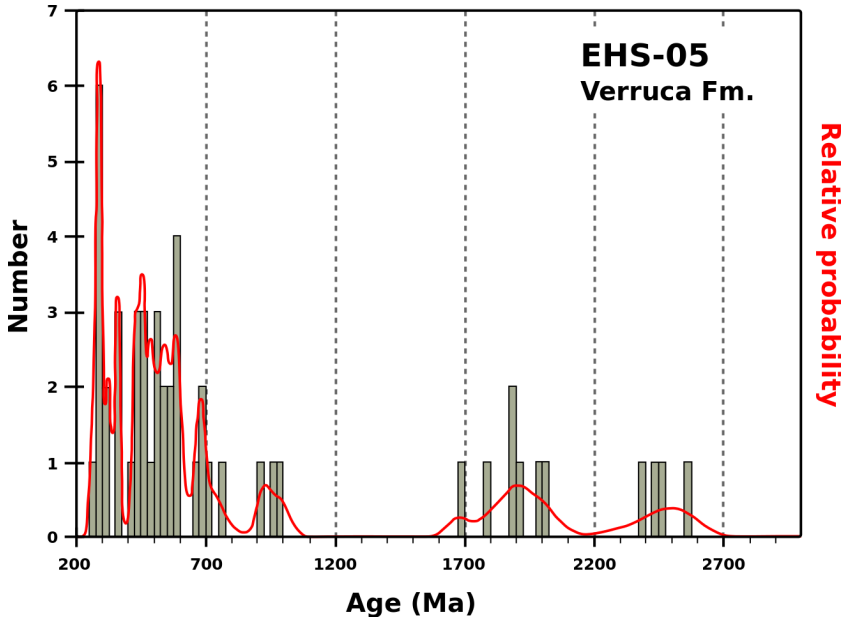

Fig. 40: Probability density plot and histogram showing the age distribution of the Verruca Formation based on the $^{238}U/^{206}Pb$- age of 50 zircons. Three different age groups with ages between 250-1000 Ma, 1650-2050 Ma and 2350-2600 Ma can be distinguished. Probability peaks are present at ca. 280 Ma, 360 Ma, 450 Ma, 580 Ma, 680 Ma and 940 Ma. Additionally, probability peaks are also present at ca. 1900 Ma and 2500 Ma.

5.6 Published work

Very few studies have previously presented U/Pb zircon ages from Elba Island. However, selected lithologies from the two lowermost units on eastern Elba have been subjects of detrital zircons studies (Fig. 41). First, Musumeci et al. (2011) provided radiometric analyses of the Mt. Calamita Schist (Porto Azzurro Unit, Complex I) and the Ortano Porphyroid (Ortano Unit, Complex II). Later, Jørgensen (2011) presented a detrital zircon study of the Mt. Calamita Schist, as well as the Capo d'Arco Schists, Ortano Porphyroids and the silver-grey phyllites and quartzites in the Ortano Unit.

The U/Pb analyses of the Capo d'Arco Schists from Jørgensen (2011) yielded a minimum age of 251 Ma, while the U/Pb analyses of the silver-grey phyllites and quartzites resulted in a minimum age of 319 Ma. Also, crystallization ages of the Ortano Porphyroids have been provided by Jørgensen (2011) and Musumeci et al. (2011). Jørgensen (2011) calculated a crystallization age of 440±7 Ma, while Musumeci et al. (2011) have suggested a Middle Ordovician age for the Ortano Porphyroids. Both Musumeci et al. (2011) and Jørgensen (2011) have correlated the Ortano Porphyroids to the Sardinian margin.

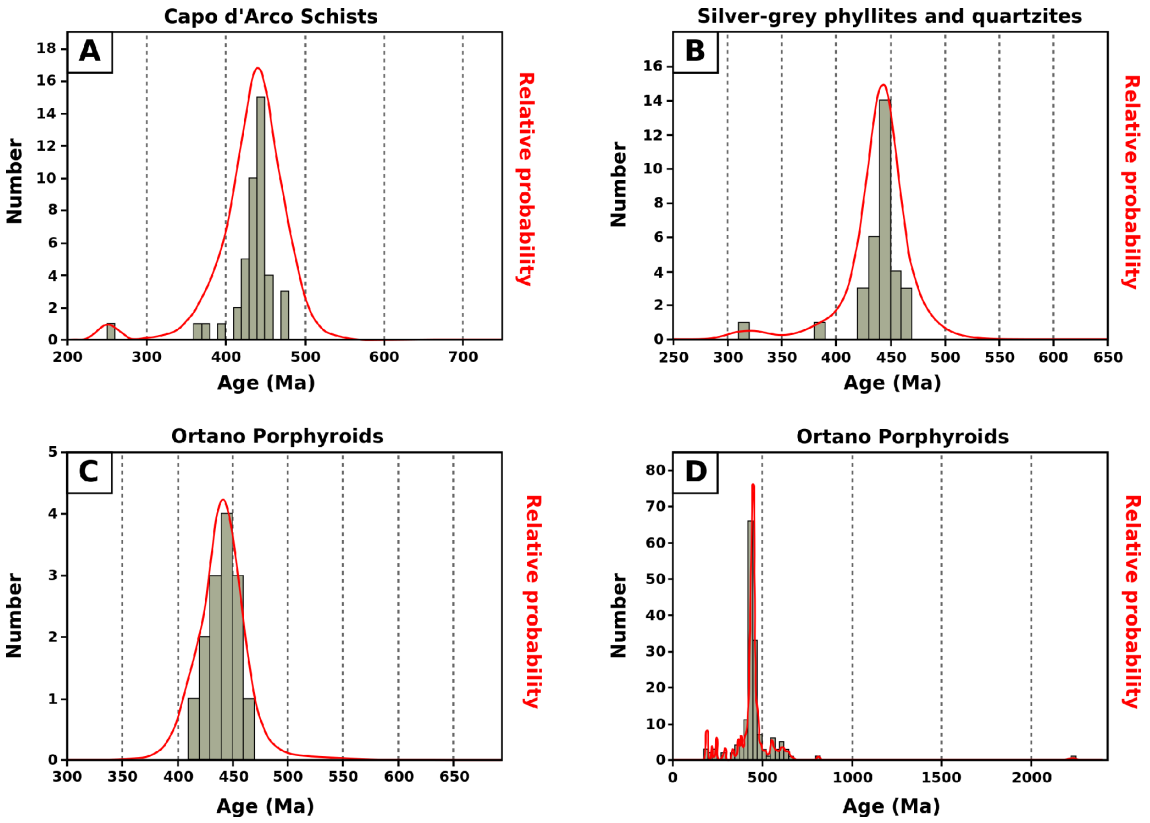

Fig. 41: Previously published work for the remaining lithologies in the Ortano Unit. Subfigure a, b and c represent the Capo d'Arco Schists, silver-grey phyllites and quartzites and the Ortano Porphyroids given by Jørgensen (2011). Subfigure d represents the Ortano Porphyroid dated by Musumeci et al. (2011).

6 Potential source regions

The U/Pb analyses of zircons that are presented in the present study reveal mainly Paleozoic ages. For the majority of the grains, oscillatory zoning is present, pointing towards a predominantly magmatic growth of the zircons. Also, all samples have distinct peaks of Variscan age. Because the Variscan Orogeny represents the final stages of the amalgamation of Gondwana with Baltica and Laurentia, it is likely that the Precambrian-lower Paleozoic zircons can be attributed to the Pan-African mobile belts or to the Neoarchean-early Paleoproterozoic cratons of the African continent. Middle-upper Paleozoic components are also present. Magmatic rocks in the Iberian Massif have earlier been dated, giving similar ages than in the present study.

Zircons are very resistant minerals that can survive several metamorphic and magmatic cycles, as well as long transportation. Due to this and the large span in ages, the zircons may have been derived from a large area. Therefore, a short summary of the geological evolution of the African continent and the Iberian Massif is presented in the forthcoming sections.

6.1 The African continent

It has been suggested that the Rodinia supercontinent was a result of the accretion of the fragments from a previous supercontinent known as Columbia (Rogers and Santosh, 2002). Columbia was a Paleo-Mesoproterozoic supercontinent that was assembled through a series of global-scale collisions of Archean cratons between 2.1 and 1.8 Ga (Rogers and Santosh, 2002; Zhao et al., 2003). This assembly resulted in several orogens, including the Transamazonian Orogen in South America and the Eburnean Orogen in West Africa (2.1-2.0 Ga), the Limpopo Belt in Southern Africa (~2.0 Ga), the Nagssugtoqidain and Trans-Hudsonian orogens in Laurentia (1.9-1.8 Ga), the Akitkan Orogen in Siberia (1.9-1.8 Ga), the Kola-Karelia Orogen in Baltica, the Trans-North China Orogen in North China (~1.85 Ga) and the Central Indian Tectonic Zone in India (~1.8 Ga) (Zhao et al., 2003). After the final amalgamation of Columbia at ~1.8 Ga, a period of magmatic accretion, lasting 600 million years, affected the continental margin of Columbia (Zhao et al., 2003). It has been suggested that the Columbia supercontinent started to break up at the end of the Paleoproterozoic. This led to continental rifting and emplacement of mafic dyke swarms (LeCheminant and Heaman, 1989; Zhao et al., 2002, 2003). Shortly after the break-up of Columbia, a new supercontinent, Rodinia, started to form (Zhao et al., 2004; Li et al., 2008).

The Rodinia supercontinent was assembled during a series of orogenic events between the middle Mesoproterozoic and the early Neoproterozoic (Li et al., 2008). During this assembly, most continents existing at that time were included in the supercontinent. Due to its surrounding Neoproterozoic passive margins, the Laurentian plate was probably located in the center of Rodinia (Condie, 2003; Pisarevsky et al., 2003; Zhao et al., 2004; Li et al., 2008). It is generally agreed that Rodinia is the result of Grenville-age orogenies (~1.1-1.0 Ga) (Meert and Torsvik, 2003; Zhao et al., 2004). According to e.g. Meert and Torsvik (2003), it is believed the sutures between the different elements in the Rodinian supercontinent are represented by the

Sveconorwegian, Grenvillian and the slightly older Kibaran orogenic belts. Dalziel et al. (2000) suggest that the accretion of arcs and other terranes during Mesoproterozoic times ended in a period of convergence and collision between the Laurentia and Kalahari cratons between 1150 and 950 Ma, resulting in the formation of the Namaqua Orogen of South Africa and Namibia and the Grenvillian-Lano Orogen of Texas. The rifting of the northern margin of Rodinia probably started between 820 and 720 Ma, while the rifting along then eastern margin started later (Pisarevsky et al., 2003). Rift-related magmatism is documented in eastern Laurentia between 760 and 550 Ma (Bingen et al., 1998). The final break-up of the Rodinia supercontinent took place at approximately 750 Ma (Cordani et al., 2003).

The rifting of Rodinia resulted in Laurentia and other smaller fragments that could be considered as the nuclei of Asia and Europe. In addition to this, it produced East Gondwana and the fragments that later formed West Gondwana (Rogers et al., 1995). According to Emmel et al. (2008), East Gondwana comprised present-day India, Antarctica and Australia while West Gondwana was made up of present-day Africa and South America. Shortly after the final break-up of Rodinia, the new, but smaller Gondwana supercontinent formed (Meert and Torsvik, 2003). Convergence along a network of Pan-African-Brasiliano orogenic belts during the Ediacaran and Cambrian resulted in the final assembly of Gondwana at 520 Ma (Grunow, 1999; Cordani et al., 2003; Bingen et al., 2009). The Pan-African Orogeny is described as a series of orogenic events between approximately 950 and 500 Ma (Muhongo and Lenoir, 1994). The East African-Antarctic Orogen is probably one of the Earth's largest orogenic belts (Jacobs et al., 2003a), and extends for more than 8000 km from Arabia-Egypt in the north, through East Africa, Madagascar and Mozambique and towards Dronning Maud Land in East Antarctica in the south (Jacobs et al., 2008). It formed during the continent-continent collision between parts of West and East Gondwana during a Pan-African event at 650-510 Ma (Jacobs et al., 2003b).

The Mozambique Belt (Fig. 42) extends from northern Kenya to Mozambique and was formed due to the closure of the "Mozambique ocean" and the amalgamation of West and East Gondwana (Jacobs et al., 1998; Muhongo et al., 2001). The Mozambique Belt is composed of metasedimentary and metaigneous gneisses and granulites, as well as post-kinematic granites and pegmatites in parts of the belt (Muhongo et al., 2001). It is suggested by Muhongo et al. (2001) that the orthogneisses with a granitoid origin were emplaced during Neoarchean times (2740-2608 Ma). The study of Muhongo et al. (2001) also reveals Paleoproterozoic xenocryst ages in metaplutonic (2025 and 1750 Ma) and metavolcanic (1880 Ma) gneisses in the Usambara Mountains. Xenocryst ages in the same metavolcanic gneisses also reveal Mesoproterozoic ages (1225 and 1095 Ma). Ages between 841 and 656 Ma are probably linked to a period of depositional and magmatic activity in the Mozambique Belt that can be correlated with other parts of the Belt (Muhongo et al., 2001). A study carried out by Kröner et al. (2001) in the Mozambique Belt reveals three distinctive magmatic and metamorphic events: 1) A calc-alkaline granitoid intrusion (1040-929 Ma) that is correlated with the Kibaran Orogeny during the assembly of Rodinia, 2) Pan-African calc-alkaline granitoid intrusions (710-555 Ma) and 3) a thermal peak during the Pan-African high-grade metamorphism (571-549 Ma).

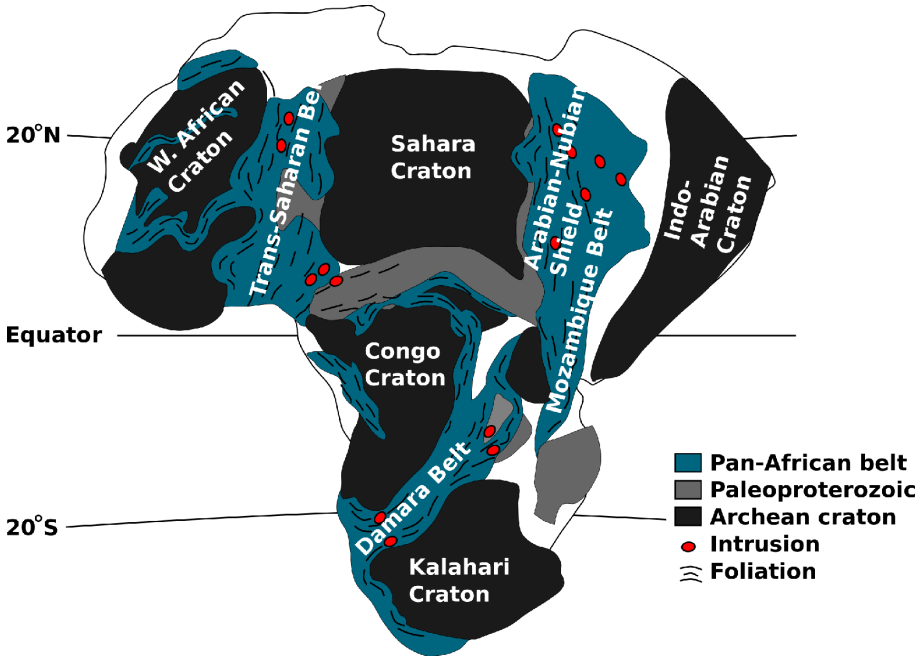

Fig. 42: Sketch of the basement of the African continent, showing the different cratons and the Paleoproterozoic and Pan-African belts. Modified after Johnson and Woldehaimanot (2003) and Seranne et al. (2008)

The Arabian-Nubian shield represents an early accretionary phase of the East Africa-Antarctica Orogen. This shield is probably one of the best exposed and preserved examples of Neoproterozoic juvenile continental crust on the Earth with a size of at least 6 million km^2. Hargrove et al. (2006) suggest that some of the youngest tectonic and magmatic events in the East African Orogen are recorded in the Arabian-Nubian shield, represented by crystallization ages between 830 and 550 Ma. It is also suggested that the extraction of the crust from the mantle started at 870 Ma, but most of the extraction took place between 830 and 740 Ma (Hargrove et al., 2006). According to Johnson and Woldehaimanot (2003), the Arabian-Nubian shield accreted through four stages at 780-760 Ma, 750-660 Ma, 680-640 Ma and 650-600 Ma, starting with arc-arc convergence around 780 Ma and resulting in terrane amalgamation around 600 Ma. Between 750 and 500 Ma, the collision between the East Saharan block, the Congo craton and the West African craton resulted in the formation of the Neoproterozoic Trans-Saharan Belt, a belt extending for 3000 km between Mali and Saudi Arabia (Black and Liegeois, 1993; Ferré et al., 2002). Accreted island arcs composed of tonalite, granodiorite and trondhjemite characterize parts of this orogenic belt. It is also characterized by reactivated Archean and Paleoproterozoic terranes, ophiolitic sutures and large shear zones that are parallel to the margin of the cratons (Black and Liegeois, 1993).

During the collision between the Kalahari and Congo cratons, the Damara Belt (Fig. 42) was formed (Johnson et al., 2006). U/Pb dating of zircons point towards a syn-tectonic crystallization age of ca. 550 Ma (Johnson et al., 2006), interpreted as the age for the main collisional phase of the south central zone of the Damara Belt. The Congo craton is located in the northern part of the Central African Fold Belt (Toteu et al., 2001). The tectonic evolution of the Congo craton starts with crust formation during late Archean times. This is supported by Nd isotopic signatures of xenocrystic zircons (Toteu et al., 2001). U/Pb ages from plutonic and sedimentary

rocks point towards a metamorphic event during the Eburnian Orogeny around 2100 Ma. Toteu et al. (2001) interprets the late Neoproterozoic (630-580 Ma) metamorphic minerals and zircons in syn-tectonic granitoids as parts of the assembly of West Gondwana. Alkaline granites have been dated by Toteu et al. (2001). Rb/Sr ages of 550-500 Ma document the emplacement of post-tectonic alkaline granitoids in the Central African Fold Belt and can be related to the uplift of the Pan-African Belt (Toteu et al., 2001).

The terrane detachment from the northern margin of Gondwana started during Late Ordovician times and is associated with the opening of back-arc basins (von Raumer et al., 2002). Von Raumer et al. (2002) have suggested that the terranes were detached during three stages. First, the Avalonia blocks detached from Gondwana in a transform margin setting during the early Ordovician (von Raumer et al., 2002; Stampfli et al., 2002b, 2006). This was followed by the the detachment of the European Hunic terranes (late Silurian) and then the Asiatic Hunic terranes (early Devonian) (von Raumer et al., 2002; Stampfli et al., 2002b).

6.2 Iberian Massif

The evolution of the pre-Variscan terranes can be traced back to the subduction of the oceanic ridge in the Proto-Tethys beneath the Gondwana margin, which started during the late Neoproterozoic (Stampfli et al., 2002b). Volcanic arcs were formed along the border of the future microcontinents on the Gondwanan margin, representing an early stage of the Cadomian Orogeny (Fernández-Suárez et al., 2000; Stampfli et al., 2002b).

The basement of the Iberian Massif can be associated both with the Pan-African (Quesada, 1991) and Cadomian orogenies. The Cadomian Fold Belt constitutes the basement in large parts of western and central Europe. In addition to the Cadomian basement units, evidence of different stages of late Precambrian to early Paleozoic tectonism can be distinguished. These include successive stages of oceanic crust development, active margins, collision zones and volcanic arcs (Stampfli et al., 2002b). Fernández-Suárez et al. (2000) suggest that northwestern Iberia was a part of a Neoproterozoic assemblage of terranes that comprises the Cadomian-Avalonian terranes, formed on an active Gondwana margin. The Cadomian Orogeny is still preserved in the Ossa-Morena Zone in SW Iberia (Fig. 43). The Ossa-Morena Zone is interpreted as an accretion of continental arcs in central Iberia during Neoproterozoic-earliest Cambrian times (Sánchez-García et al., 2003; Romeo et al., 2006). The oldest calc-alkaline rocks in the Ossa-Morena Zone have U/Pb ages between 611 and 550 Ma. These rocks correspond to the main stage of the magmatism related to the Cadomian Orogeny (Romeo et al., 2006).

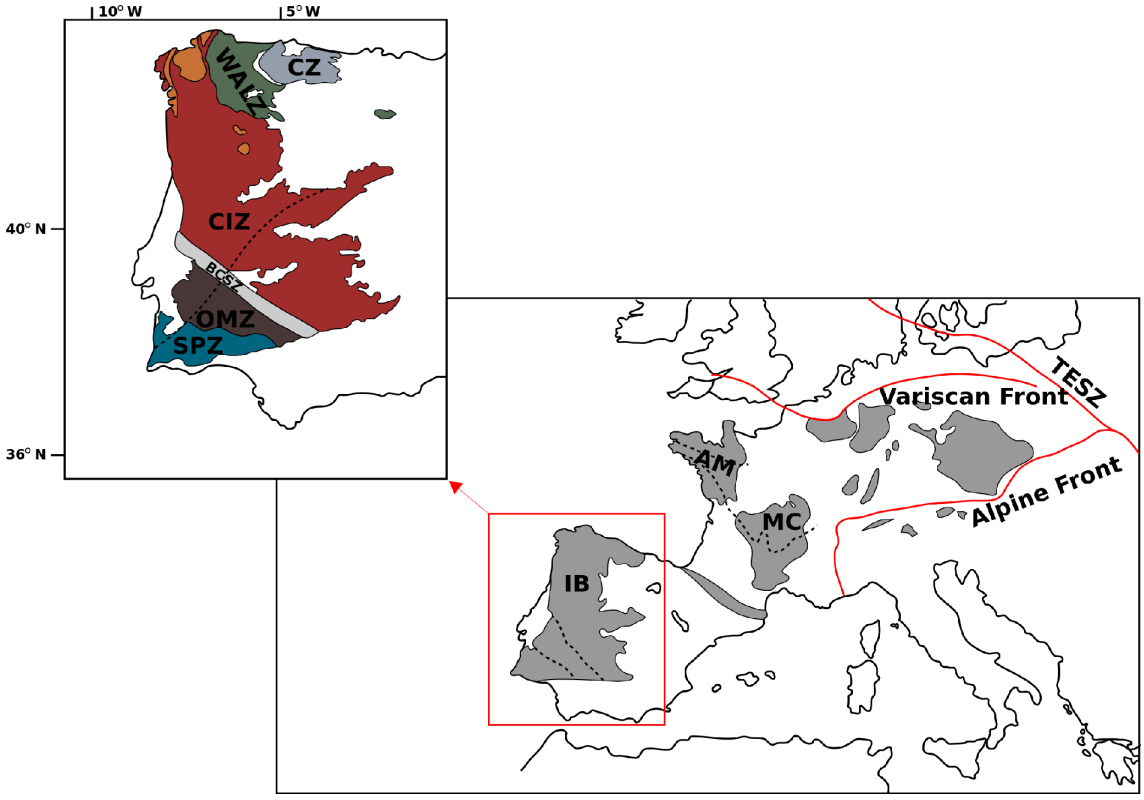

Fig. 43: Simplified map of the European Variscan Massifs. A detailed sketch of the Iberian Massif is shown in the left figure. **AM:** Armorica Massif; **BCSZ:** Badajoz-Cordoba Shear Zone; **CIZ:** Central Iberian Zone; **CZ:** Cantabrian Zone; **IB:** Iberian Massif; **MC:** Massif Central; **OMZ:** Ossa-Morena Zone; **SPZ:** South Portuguese Zone; **TESZ:** Trans European Suture Zone; **WALZ:** West Asturian-Leonese Zone. Modified after Carrigan et al. (2005) and Valle Aguado et al. (2005).

It is suggested by e.g. Sánchez-García et al. (2003) that the Cambrian-Ordovician rifting event that ended with the formation of a part of the Paleozoic Rheic ocean. This event is recorded in the Ossa-Morena Zone (Sánchez-García et al., 2003; Romeo et al., 2006). Most of the volcanic rocks that were emplaced during the late Cambrian-early Ordovician are rift-related mafic to felsic rocks that are associated with the opening of the Rheic ocean and the drifting of Avalonia (Stampfli et al., 2002b; Gutiérrez-Alonso et al., 2008).

The pre-Variscan basement blocks in central Europe were reorganized during the Variscan and the Alpine orogenic events (von Raumer et al., 2002). The Variscan Orogeny in Europe represents the final stages of the amalgamation of Laurentia and Baltica with Gondwana prior to the formation of the supercontinent Pangea between 480 and 250 Ma (Behr et al., 1984; Carrigan et al., 2005; Rossi et al., 2009). The Variscan Orogeny commenced during mid-Devonian times with an oblique subduction of the Rheic ocean below the southern part of the Ossa-Morena Zone (Romeo et al., 2006). The westernmost outcrops of the Variscan Orogenic Belt in Europe are located in the Iberian Massif (Quesada, 1990; Romeo et al., 2006). Together with the Central Iberia Zone and Galicia, the Ossa-Morena Zone represents the pre-orogenic successions in the Iberian Massif (Quesada, 1990). By moving the Corsican-Sardinian and Iberian blocks back to their pre-Mesozoic positions and linking them with the stable massifs (Armorican,

Ardennes-Rhenohercynian, Bohemian and French Massif Central), it is possible to reconstruct a continuous Variscan Belt between the Bohemian and Iberian massifs (Matte, 1986). Paleomagnetic data suggest that the collision between Laurasia and Gondwana did not happen before Carboniferous times (Stampfli and Borel, 2002). The margins of the Iberian plate are mainly a result of the Mesozoic opening of the North Atlantic and Tethys, as well as the amalgamation of Pangea during the late Paleozoic (Sánchez-García et al., 2003).

Since the Middle Jurassic, the motion of Iberia with respect to Europe has been subject to fluctuations. This is indicated by a Middle Jurassic-Lower Cretaceous sinistral strike-slip movement of more than 200 km, a late Cretaceous convergence, a quiet period during the Paleocene, a short period of dextral strike-slip movement with a total displacement of 60-70 km and an Eocene-Oligocene convergence (Rosenbaum et al., 2002). Since late Cretaceous times, a total convergence of 160-170 km between Europe and Iberia is suggested. At the same time, Gondwanan fragments were accreted onto the European margin (Rosenbaum et al., 2002). A counter-clockwise rotation of Corsica-Sardinia during Oligocene-Miocene times was responsible for the opening of back-arc basins (Speranza et al., 2002). It is generally accepted that the Corsica-Sardinia microplate was a part of southern France-northern Iberia and that it was detached during the opening of the Liguro-Provençal basin during early Oligocene times (Turco et al., 2012). During the Oligocene-early Miocene, the Adriatic plate was subducted below the margin of Corsica-Sardinia, resulting in the imbrication of the Adriatic plate. The Ligurian accretionary wedge was also thrust onto the Tuscan continental margin (Bortolotti et al., 2001a).

Corsica is divided into the autochtonous Variscan (or Hercynian) Corsica and the Alpine Corsica domains (Molli, 2008). The rocks on Corsica cover a large time span, ranging from early Paleozoic to Miocene. The Variscan Corsica is made up of an early Paleozoic metamorphic basement, intruded by late Carboniferous-Permian granites and covered by sedimentary rocks of up to Eocene age (Jolivet et al., 1998; Molli, 2008). According to Molli (2008), the Alpine Corsica is composed of three major groups of rocks. 1) Variscan granitoids and series of Permian-Eocene metasedimentary rocks that are parts of the strongly deformed Corsican continental margin (i.e. the Tenda Massif) (Molli et al., 2006). 2) The "Schistes Lustrés" nappe that contains the Ligurian Tethys-derived ophiolitic units, made up of gabbros, pillow lavas, ultramafic rocks and Jurassic-Cretaceous metasedimentary rocks. This unit has been correlated with the Acquadolce Unit on Elba. 3) A low-grade assemblage of ophiolithic and continental units resting above the "Schistes Lustrés" in the nappe stack (Molli, 2008). The Tenda Massif consist mainly of late Variscan granitoids that are intruded by gabbroic intrusions of lower Permian age and crosscut by basaltic to rhyolitic dykes (Molli et al., 2006). According to Molli et al. (2006), the Tenda Massif has a polyphase deformation history, including two generations of isoclinal folds that are overprinted by a late phase of open and kink folds. The main metamorphic and magmatic features on Corsica and Sardinia are associated with continent-continent collision during the Variscan Orogeny. Remnants of the pre-Variscan basement are present in the Tenda Massif. However, these are only present as scattered fragments (Molli et al., 2006). In Ordovician and Silurian times, two periods of igneous activity occured on Sardinia. During the first period, only acidic volcanic rocks were emplaced, while acidic to basic volcanic rocks were emplaced during the second period. These rocks have been dated to ~450 Ma (Beccaluva et al., 1985;

in Tommasini et al., 1995) and are correlated with the orthogneisses in the Corsican basement (Tommasini et al., 1995).

The collision between Corsica-Sardinia and the Adriatic plate during the Eocene-early Miocene resulted in the northern Apennine thrust wedge. The lowermost levels that are exposed can be found in the Apuan Alps on the mainland of Tuscany (Molli et al., 2000). As a result of this convergence, oceanic Liguride units were emplaced on the Adriatic margin. These units are now present in the Tuscan Nappe (Molli et al., 2000) and are also evident on Elba Island. During late Oligocene-early Miocene times, shearing of the Adriatic continental margin occured (Bortolotti et al., 2001a). The Apuane Alps represent a tectonic window through the allochtonous cover sequence of the Tuscan Paleozoic basement (Carmignani et al., 1978). These units include the Permian-Oligocene Apuane Metamorphic Complex at the base, the Tuscan Nappes and the Liguride Units at the top (Carmignani et al., 1978; Dini et al., 2001). The Apuane Metamorphic Complex comprises two main units consisting of the Paleozoic basement unconformably overlain by either Upper Triassic to Oligocene (Apuane Unit) or Upper Triassic-Lower Cretaceous (Massa Unit) metasedimentary covers (Molli et al., 2000; Dini et al., 2001). The Paleozoic basement below the Apuane and Massa units represents a late Cambrian-Devonian lithostratigraphic succession. According to Conti et al. (1993; *in* Dini et al., 2001), the Paleozoic basement is, from bottom to top, composed of the lower quartzites and phyllites (late Cambrian-early Ordovician), middle Ordovician porphyroids and porphyritic schists, late Ordovician metasandstones, quartzites and phyllites and late Silurian-Devonian graphitic phyllites, dolostones, calcschists and metalimestones. It has been suggested by Pandeli and Puxeddu (1990) that non-fossiliferous phyllites and quartzites in the Ortano Unit, which has been subject to this study, have an early Paleozoic age because of the correlations with the Ordovician successions in the Apuane Alps and on Sardinia. Both Pandeli and Puxeddu (1990) and Musumeci et al. (2011) suggest a correlation to the middle Ordovician porphyroids on Sardinia. This is also supported by Jørgensen (2011), suggesting that the Ortano Unit is derived from the Corsica-Sardinia magmatic and siliciclastic successions.

7 Discussion

Earlier work by Musumeci et al. (2011) and Jørgensen (2011) have provided detrital zircon ages of the Mt. Calamita Schists in Complex I and the Ortano Porphyroids in Complex II. In addition to this, Jørgensen (2011) has presented a detrital zircon study of the silver-grey phyllites and quartzites and the Capo d'Arco Schists within the Ortano Unit in Complex II. A refined model for the origin of the cover sequence of the Tuscan basement on Elba Island is suggested in the present study. A special focus is given to selected lithologies within the Ortano, Acquadolce and Monticiano-Roccastrada units in Complex II and III, including the Capo d'Arco Schists, the blackish quartzites and phyllites, the phyllites and metasiltstones and the Rio Marina and Verruca formations.

The age distribution tend to become more complex with respect to the implied stratigraphical position (Fig. 44). This is indicated by the unimodal and bimodal age distributions for the samples in the Ortano Unit, while the samples from the Acquadolce and Monticiano-Roccastrada units show polymodal age distributions. The different units will be discussed in the following sections, based on their present-day stratigraphic position.

Earlier work have correlated the lithologies within the Ortano Unit to the Paleozoic successions in Tuscany and on Sardinia due to petrographical, geochemical and microstructural similarities (Pandeli and Puxeddu, 1990). The Acquadolce Unit has previously been attributed to the upper part of the Lower Cretaceous successions in the Apuane Alps (Barberi et al., 1967*; in* Bortolotti et al., 2001a; Duranti et al., 1992). The Verruca Formation has traditionally been correlated to the Verrucano succession in the Mt. Pisani area on the mainland of Tuscany (Rau and Tongiorgi, 1974*; in* Bortolotti et al., 2001a). Based on the age signature and internal structure, the present study suggests different affinities for the different lithologies sampled within these units.

Maximum depositional ages have earlier been proposed for the Capo d'Arco Schists and the silver-grey phyllites and quartzites by Jørgensen (2011). This study presents a more refined study of the Capo d'Arco Schists, including a zircon crystallization age for the source rock of the zircons in the quartzitic phyllites within the Capo d'Arco Schists. In addition to this, a maximum age of deposition is suggested for all other samples on the basis of the three youngest grains in the samples or zircon crystallization ages. The three youngest ages are used in order to use a more robust constraint on the maximum deposition ages.

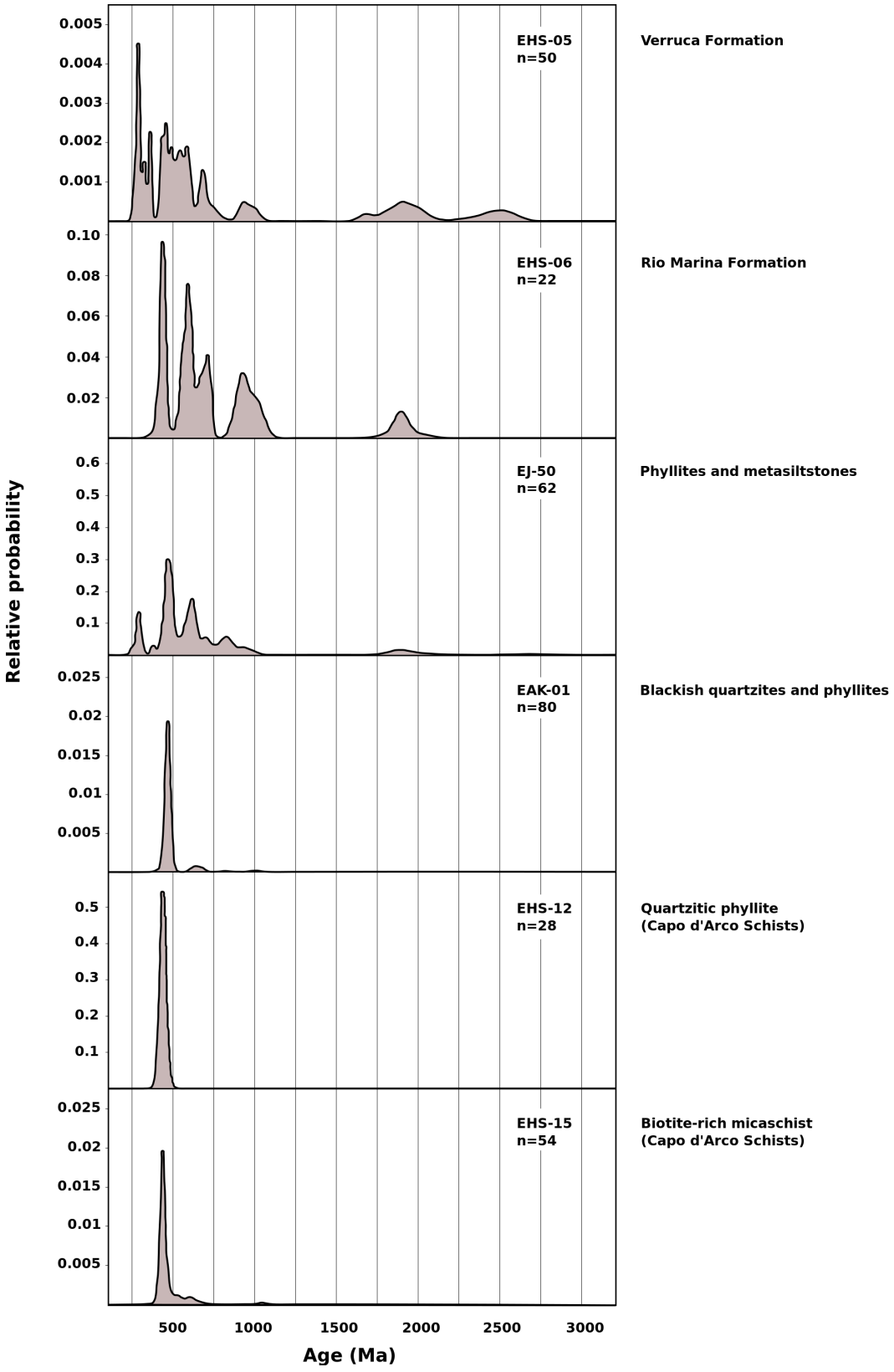

Fig. 44: Compilation of probability density plots for all samples that were analysed during this study, sorted with respect to their implied stratigraphic position. Only ages older than 100 Ma are included. A more complex and widespread distribution occurs from bottom to top in the stratigraphy.

7.1 Ortano Unit

Based on petrographic similarities, Boccaletti et al. (1980*; in* Pandeli and Puxeddu, 1990) considered Complex II as a southward extension of the Apuane zone. An early Paleozoic age for all non-fossiliferous rocks within the Ortano Unit was later proposed by Pandeli and Puxeddu (1990). Pandeli and Puxeddu (1990) suggest a correlation between the Ortano Unit and the Paleozoic sequences on Sardinia and in Tuscany on the basis of geochemical, microstructural and petrographical data. Thus, they exclude the possibilty of identifying the Apuane zone on Elba. In order to complement the data from the Ortano Unit given by Musumeci et al. (2011) and Jørgensen (2011), a more refined study of the Capo d'Arco Schists is presented. Also, detrital zircon ages from the blackish quartzites and phyllites are presented so that a complete record of detrital zircon ages for the Ortano Unit is now available. Probability density plots of the analysed samples from the Ortano Unit are shown in Fig. 45.

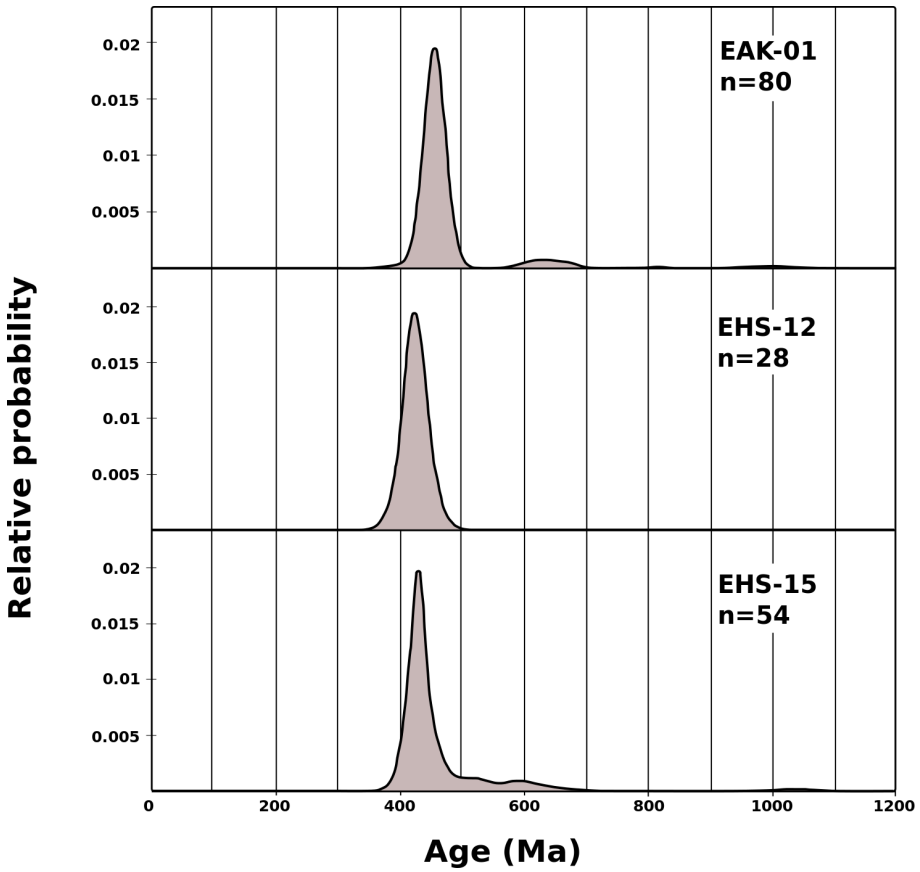

Fig. 45: Comparison of the probability density plots for the analysed lithologies in the Ortano Unit. EHS-12 and EHS-15 are from the Capo d'Arco Schists, representing the quartzitic phyllite and the biotite-rich micashist. EAK-01 is the sample from the blackish quartzites and phyllites. Peaks are present at 420 Ma, 430 Ma and 450 Ma for the quartzitic phyllite, the biotite-rich micaschist and the blackish quartzites and phyllites, respectively.

Different hypotheses exist on the origin of the Capo d'Arco Schists (also known as Ortano Schists in e.g. Puxeddu et al., 1984). Puxeddu et al. (1984) have suggested that the Capo d'Arco Schist

represent reworked porphyroids of lower-middle Carboniferous age, while Pandeli and Puxeddu (1990) and Duranti et al. (1992) suggest a correlation to the Cambro-Ordovician shales and metasandstones on central-southern Sardinia. However, later work by i.e. Pandeli et al. (2006) suggest an Ordovician age for the Capo d'Arco Schists. Recently, Jørgensen (2011) presented the first radiometric dating of zircons in the metasandstones in the Capo d'Arco Schists. These results yielded a maximum depositional age of 251±13 Ma, and Jørgensen (2011) correlated it to the Variscan Orogenic cycle. During the present study, two different varieties of the Capo d'Arco Schists have been analysed. These are the biotite-rich micaschist and the quartzitic phyllite. This was done in order to examine if there were any differences between these two sub-lithologies with respect to their age.

The zircons in the biotite-rich micaschist appear mostly as oscillatory zoned grains with a more complex core, pointing towards a magmatic origin of the sediment (Corfu et al., 2003). This indicates multi-stage growth of the zircons. Well-defined boundaries between the cores and the rims also support this interpretation. 98% of the zircons give ages between 400 and 700 Ma. However, one single grain has an age around 1040. Most of the grains that yielded ages close to or above 500 Ma were analysed in the inherited cores. The probability density plot gives an age peak around 430 Ma, indicating a middle Silurian age for the main source of the sediments.

Most of the zircons that were dated in the quartzitic phyllites show either oscillatory zoning or zoning parallel to the c-axis of the crystal, indicating a magmatic origin of the zircons in the sample (Corfu et al., 2003). A magmatic origin is also supported by the unimodal age distribution of the grains. A middle Silurian age is suggested also for this sample. Because of the unimodal age distribution and magmatic texture of the grains, a crystallization age of 422±8 Ma was obtained by the use of the TuffZirc algorithm from Ludwig and Mundil (2002).

By comparing the quartzitic phyllite with the biotite-rich micaschist, one can see that the age distribution is slightly different. Both samples show a distinct peak during early Silurian times. While the quartzitic phyllite shows a Gaussian age distribution with ages between 397 and 451 Ma, the age distribution of the micaschist is more dispersed with a continuous age distribution between 400 and 700 Ma. In addition to the clear peak at 430 Ma, it also has a smaller probability peak around 560 Ma. One grain of Meso- to Neoproteroic age is responsible for the probability peak at 1040 Ma. Both the morphology and the internal structure of the zircons in the two samples differ. The zircons in the quartzitic phyllite are generally shorter and show a less distinct zoning than the biotite-rich micaschist. There are no significant differences in the rounding of the zircons. Because of the similarities in the internal structures, but differences in age distribution, it is suggested that the quartzitic phyllites are derived from magmatic source, while the biotite-rich micaschists are derived from a metasediment with a magmatic protolith.

The zircons in the blackish quartzites and phyllites are responsible for the most dispersed age distribution for the Ortano Unit samples analysed in this study. However, even though a polymodal tendency is present, only the two youngest peaks at 450 and 620 Ma dominate. The majority of the grains that are younger than 600 Ma show oscillatory zoning or c-axis parallel zoning. Except for the single grain with an age of 1005 Ma with distinct oscillatory zoning, sector zoning is present in parts or in whole grains for the zircons with ages above 600 Ma. Based on

the zonation, it is interpreted that the younger grains and the oldest grain represent magmatic events (Corfu et al., 2003).

U/Pb ages from the metavolcanic rocks in the Central Iberian Zone have been presented by Valverde-Vaquero and Dunning (2000). These ages range from 468 to 488 Ma. Helbing and Tiepolo (2005) have obtained U/Pb ages from zircons in metavolcanic rocks on Sardinia, ranging from 456 to 474 Ma. Due to this, the metavolcanic rocks on Sardinia have been attributed to the Central Iberian Zone. The magmatic activity in the Central Iberian Zone and on Sardinia have been related to magmatism associated with the break-up of Gondwana and the opening of the Rheic Ocean (Valverde-Vaquero and Dunning, 2000). By dating lower Paleozoic rocks on Sardinia, Oggiano et al. (2010) have distinguished three volcanic events associated with the North Gondwana margin. 1) Late Cambrian-early Ordovician intermediate-felsic volcanic event, 2) Middle Ordovician calc-alkaline volcanic event and 3) uppermost Ordovician-lowermost Silurian (∼440 Ma) alkaline volcanic event (Oggiano et al., 2010; Gaggero et al., 2012). The samples from the Ortano Unit show a relatively simple age distribution with dominating peaks between 420 and 450 Ma, and small peaks between 560 and 1040 Ma. Due to the stratigraphic position and the previously suggested ages in Bortolotti et al. (2001a), it is likely that the similar ages between the lithologies can be interpreted as being derived from the same source. It is here interpreted that the source responsible for the major peak in the samples from the Capo d'Arco Schists and the blackish quartzites and phyllites is the same for the three samples. This source is most likely related to the late Ordovician-early Silurian magmatic cycle on Sardinia (Gaggero et al., 2012).

The second age group is characterized by probability peaks at 560 and 620 Ma in the biotite-rich micaschist and in the blackish quartzites and phyllites, respectively. The oldest grains in the Ossa Morena Zone (Iberian Massif) have similar ages, and those grains have previously been correlated to the main magmatic phase of the Cadomian Orogeny (Romeo et al., 2006). Based on only the age signatures, a correlation to the main magmatic phase of the Cadomian Orogeny can be proposed. The zonation in the zircons within this age range does not clearly point towards a magmatic origin. Faint, sector-like zoning and c-axis parallel zoning occurs. Sector zoning may point towards a metamorphic growth of the zircons, but Corfu et al. (2003) also report that sector-like zoning can be present in igneous zircons. Because of this and the fact that c-axis parallel zoning occurs, a magmatic origin is suggested for these grains. In addition to these age groups, the blackish quartzites and phyllites also include one grain with an age of 812 and two grains with ages around 1.0 Ga. These two latter grains can be correlated with the grain with the same age in the biotite-rich micaschist. Hargrove et al. (2006) have proposed crystallization ages of 573-813 Ma, recording the earliest magmatic events in the East African Orogen in the Ariabian-Nubian Shield. Based on this, it is interpreted that the 812 Ma grain is correlated to this event. Magmatic events between 1040 and 929 Ma have been documented in the Mozambique Belt by Kröner et al. (2001). This event has earlier been correlated to the assembly of Rodinia and the Kibaran Orogeny. Thus, a correlation between the oldest grains analysed in the present study and this magmatic event is proposed. A summary of the tectonic events responsible for the different zircon populations is shown in Fig. 46.

Bortolotti et al. (2001a) have earlier suggested an Ordovician age for the Ortano Unit. The

three youngest concordant ages in the sample are used to infer the earliest possible age of deposition. The three youngest zircons within the blackish quartzites and phyllites have ages of 386±21, 430±12 and 443±17 Ma. Based on this, it is suggested that the earliest possible time of deposition was during the uppermost Silurian. The three youngest grains in the biotite-rich micaschist yielded minumum ages of 403±21, 410±14 and 411±11 Ma, while the three youngest grains in the quartzitic phyllite have ages of 397±18, 403±10 and 409±17 Ma. Due to this, a Lower Devonian age is suggested for the earliest possible age of deposition of the Capo d'Arco Schist. The age distribution from Jørgensen (2011) of the Capo d'Arco Schist is similar to the age distribution in this study. Both the age distributions from the present study and from Jørgensen (2011) show primary peaks in the age distribution between 430 and 440 Ma. The analyses of EHS-12 and EHS-15 also show some grains with Meso- to Neoproterozoic ages, while the analysis of the sample from Jørgensen (2011) mainly shows Paleozoic ages. In addition to this, the sample from Jørgensen (2011) has a secondary probability peak around 250 Ma. According to Jørgensen (2011), this is due to a concordant grain with a $\frac{^{206}Pb}{^{238}U}$-age of 251±13. Based on this grain, the maximum depositional age for the Capo d'Arco Schists is placed at the Permian-Triassic boundary. However, this grain is highly discordant (∼40% discordancy) and has a relative standard error (RSE) of 11.8. Because of its relatively high discordancy and high relative standard error, it is here suggested that this grain should have been excluded. Therefore, it is suggested that a younger maximum depositional age than the Lower Devonian cannot be constrained.

Bortolotti et al. (2001a) have proposed the hypothesis that the Ortano Unit consist of a large isoclinally folded sequence with the Ortano Porphyroids as the oldest rocks. They also suggest that the Capo d'Arco Schists represent the same horizon as the silver-grey phyllites and quartzites, which are now overlying both blackish quartzites and phyllites and the Ortano Porphyroids. If this hypothesis is correct, the silver-grey phyllites and quartzites must have the same age signature and similar internal structure as the Capo d'Arco Schists. As this study does not include either analyses or cathodoluminescence imaging of the Ortano Porphyroids or the silver-grey phyllites and quartzites, the results and properties from those lithologies are mainly based on the work by Jørgensen (2011), but also the work by Musumeci et al. (2011). In addition to this, an unpublished SIMS age for the Ortano Porphyroids from Jacobs (pers.comm.) is presented. By comparing the internal structure of the zircons in the silver-grey phyllites and quartzites from Jørgensen (2011) with the ones from Capo d'Arco Schists in this study, it is evident that they look similar as oscillatory zoning and c-axis parallel zoning are present in both samples. By comparing the age distribution from the silver-grey phyllites and quartzites and the Capo d'Arco Schists, there are only minor differences. The samples have peaks around 420-440 Ma, but the silver-grey phyllites and quartzites also have a single grain with an age of 319±18 Ma. However, similar to the young grain in the Capo d'Arco Schists from Jørgensen (2011), this grain is highly discordant (∼27% discordancy). It is therefore suggested that also this grain should have been excluded. Based on the age and internal structure, a correlation between the silver-grey phyllites and quartzites and the Capo d'Arco Schists is proposed. If the hypothesis from Bortolotti et al. (2001a) is correct, the age of the Ortano Porphyroids has to be older. In the present study, a crystallization age of 422±8 Ma for the quartzitic phyllite has been established. Jørgensen (2011)

suggested a crystallization age of 440±7 Ma for the Ortano Porphyroids, based on LA-ICPMS analyses. However, a more precise, unpublished SIMS age of 460±3 Ma from the same sample is given by Jacobs (pers.comm.). Nevertheless, the crystallization ages given by Jørgensen (2011) and Jacobs (pers.comm.) are both older than the crystallization age of the quartzitic phyllite. These findings are in agreement with the hypothesis of Bortolotti et al. (2001a), indicating that the silver-grey phyllites and quartzites and the Capo d'Arco Schists form the two limbs of a pre-thermometamorphic, east-vergent fold with the older Ortano Porphyroids in its core. Results from this study, as well as results from Jørgensen (2011) and Jacobs (pers.comm.), agree with the hypothesis of Bortolotti et al. (2001a), indicating that the Ortano Porphyroids should be considered as the core of the fold and therefore being regarded as the oldest stratigraphic unit in the Ortano Unit.

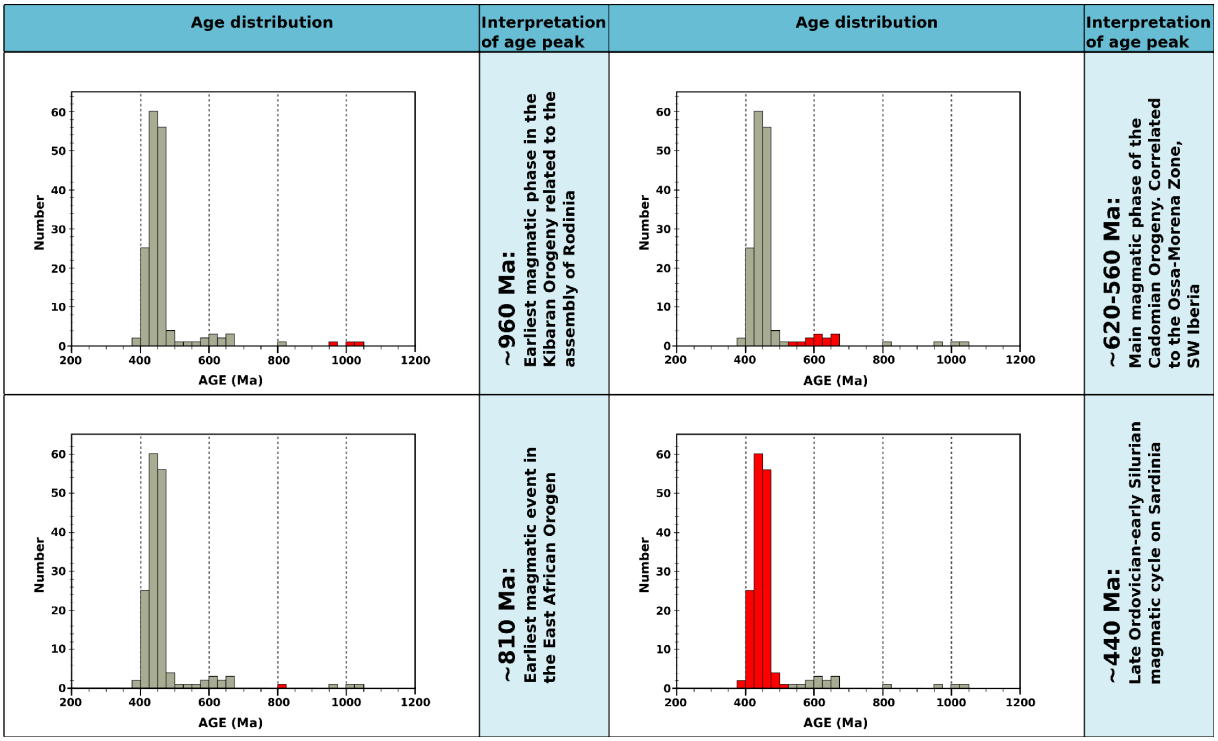

Fig. 46: Cumulative histograms for the samples from the Ortano Unit, presenting an overview of the interpretation of the origin of the zircons for the different age intervals. Red boxes represent grains correlated to the specific event. The other boxes are not correlated to that specific event.

7.2 Acquadolce Unit

The phyllites and metasiltstones in the Acquadolce Unit have previously been correlated to the epimetamorphic Mesozoic-(Tertiary?) successions in the Apuane Alps (Barberi et al., 1967*; in* Bortolotti et al., 2001a). Later work by Duranti et al. (1992) revealed microfossils that are correlated to the upper part of the Lower Cretaceous.

The analyses of the zircons from the phyllites and metasiltstones yielded a polymodal age distribution, spanning between 32 and 2691 Ma for the concordant grains. 90% of the grains are located within an age interval between 250 and 1000 with a dominant peak at around 460 Ma.

Six groups of zircons are detected, based on age signature. The five oldest peaks are presented in Fig. 47.

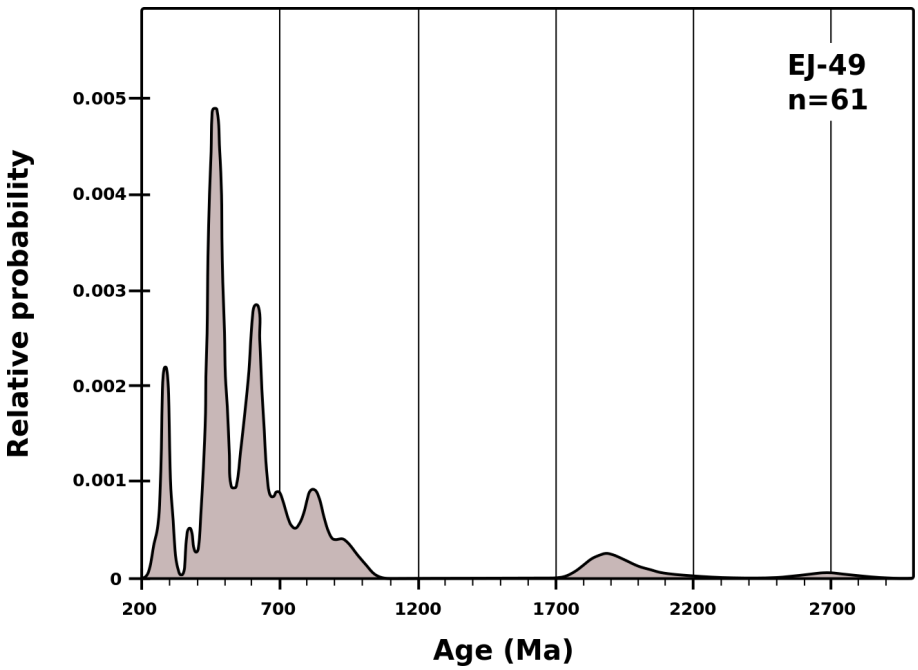

Fig. 47: Probability density plot of the analysed grains older than 200 Ma from the phyllites and metasiltstones in the Acquadolce Unit. Plots for the zircons younger than 200 Ma are shown in Fig. 33 and 34.

The first and largest group of the zircons in the phyllites and metasiltstones shows very young $\frac{^{206}Pb}{^{238}U}$-ages from 29 to 71 Ma. All of these grains, except for one single grain, were originally regarded as discordant. Thus, they were filtered out from the dataset. Due to the young ages and very low Pb/U-ratio, the uncertainty in the Pb/Pb-ratio is rather large. A large uncertainty in Pb/Pb-ratio will result in almost random Pb/Pb ages. This is probably the case in this study. It is a matter of debate whether these grains should be included or not, but the grains with a probability of concordance of at least 0.01 have been included. However, they have been plotted separately. With respect to the internal structure, the cathodoluminescence imaging shows mainly distinct oscillatory zoning. This points towards a magmatic origin of the zircons. Special care was taken during sampling so that no magmatic veins were sampled. Also, the thin-section do not show any signs of veins. Therefore, it is proposed that these grains are detrital from an igneous source. The age of 32±1 Ma obtained from the TuffZirc algorithm (Ludwig and Mundil, 2002) is interpreted as representing the crystallization age of the source of these zircons. Some of the oldest grains within this subpopulation were excluded by the TuffZirc algorithm because they were interpreted as being xenocrystic. This was due to the high age compared to the majority of the zircons in the subpopulation (Ludwig and Mundil, 2002). Cathodoluminescence imaging reveals that the morphology of the grains are, in most cases, idiomorphic. The internal structure and the morphology of the grains indicate young grains that have been transported only a relatively short distance.

There are different possibilities when it comes to interpreting the origin of the zircons. Blueschist-

facies metamorphism dated at 45-32 Ma has been reported from Corsica (Brunet et al., 2000). Between 33 and 22 Ma, rifting of the Tyrrhenian Sea and the Liguro Provençal basins occured. Meanwhile, HP-LT metamorphism was recorded in the Apuane Alps and in the eastern part of the Tuscan Archipelago (Brunet et al., 2000). However, by studying the thin-sections and the cathodoluminescence images for the young population of zircons, no signs of high-pressure metamorphism is evident. Therefore, this option is no longer considered as a valid explanation for the young grains. Another possibility is related to the Apenninic Orogeny and is interpreted as being a result of the west- to northwest-directed subduction of oceanic lithosphere starting during late Eocene times (Mattioli et al., 2012). Any evidence of volcanism associated with this subduction has been completely removed by erosion. However, volcanoclastic sediments deposited in the Val d'Aveto and Petrignacola sandstone formations have been used as an indirect record of the volcanic activity (Mattioli et al., 2002). Mattioli et al. (2002) also suggest that the Val d'Aveto-Petrignacola volcanism is possibly related to a continental volcanic arc that is presently eroded or covered by sediments within the Canetolo Sub-Ligurian domain in northern Italy. By comparing biostratigraphic data and Ar/Ar data, Mattioli et al. (2002) suggest that the Val d'Aveto-Petrignacola arc/basin setting formed in a closed sedimentary system where large amounts of volcanoclastic sediments could have been deposited during a short time interval.

The third possibility is linked to Sardinia. Two periods of Cenozoic igneous activity are present on Sardinia (Morra et al., 1997; Lustrino et al., 2004). The first period lasted from ∼32 Ma to ∼15 Ma, while the second period of igneous activity was between ∼5 Ma and ∼0.1 Ma (Lustrino et al., 2004). However, based on Ar/Ar dating of feldspars from basaltic to andesitic igneous rocks on Sardinia, Lustrino et al. (2009) suggests that the initiation of the first period of igneous activity should be shifted back to the late Eocene, while the end should be during middle Miocene times. The igneous activity of this phase corresponds well to the crystallization age of the young zircon population in the phyllites and metasiltstones. Based on the idiomorphic morphology, the lack of fractures and inclusions and the young crystallization age of the source rock, a correlation with the magmatic activity related to the collision between Africa+Adria and Europe+Iberia during late Eocene-early Miocene times is suggested for this subpopulation.

According to Bortolotti et al. (2001a), the phyllites and metasiltstones were affected by thermo-metamorphism during the emplacement of the La Serra-Porto Azzurro monzo- granite, possibly leading to lead-loss. Because the grains have, on the basis of probability of concordance, been regarded as concordant, only a complete resetting of the age can be a possibility. However, the La Serra-Porto Azzurro pluton has an age around 5.9 Ma (e.g. Maineri et al., 2003) and can therefore not be regarded as the reason for a possible lead-loss event, resulting in a complete resetting of the ages. It is therefore suggested that the random Pb/Pb ages are related to low Pb-concentrations and uncertainties in the Pb/Pb-ratio in the young zircons instead of lead-loss.

It was earlier suggested that the phyllites and metasiltstones were deposited in the upper part of the Lower Cretaceous (Duranti et al., 1992). However, by including the young grains from the present study, a younger depositional age can be constrained. A maximum age of deposition of early Oligocene times is therefore suggested on the basis of what is interpreted as the crystallization age of an igneous source. The deposition of the sediments can possibly be related to the Oligocene-early Miocene stages of the continent-continent collisional phase between

the Corsican and Adriatic margins (Bortolotti et al., 2001a).

Other subpopulations of zircons are also present in the phyllites and metasiltstones. The sample shows a continuous age distribution between 250 and 1000 Ma, including four probability peaks, as well as peaks at 1850 and 2700 Ma. The age groups within the 250-1000 Ma age range are hereafter referred to as the second to the fifth age group. Most of the zircons are oscillatory zoned, but less prominent than in the young grains. The second age group of the phyllites and metasiltstones is characterized by a peak around 280 Ma. It is suggested by Fernández-Suárez et al. (2006) that the Iberian lower crust underwent a period of melting and recrystallization between 312 and 277 Ma. Post-tectonic igneous activity related to the Variscan Orogeny have been documented by Fernández-Suárez et al. (2000) in the Iberian Massif, characterized by intrusions emplaced between 295 and 285 Ma. The melting of the crust is either related to lithospheric delamination (Fernández-Suárez et al., 2000) or increased radioactive heat production after crustal thickening (Villaseca et al., 1999). The youngest grain in this population has an age of 251±17 Ma, very similar to concordant ages of zircons given by Fernández-Suárez et al. (2006). These ages are interpreted to represent the crystallization age of emplaced alkaline dykes in the Iberian Massif. Due to these constraints, it is likely that the zircons within this age range are derived from the post-tectonic igneous activity in the Iberian Massif. The third age group is the most dominating age group. This group is characterized by a probability peak around 460 Ma. The age signature and internal structure indicate that the source for these grains might be related to the source for the analysed samples in the Ortano Unit. Due to this similarity, a correlation to the Middle Ordovician calc-alkaline magmatic cycle on Sardinia (Oggiano et al., 2010; Gaggero et al., 2012) is therfore suggested for the grains yielding these ages. The fourth age group has a peak around 610 Ma. As with the rest of the concordant grains in this sample, these grains show oscillatory zoning. Even though the zoning is less prominent than in the young grains, a magmatic origin is suggested for these zircons. The age signature of these is quite similar as the 620 Ma peak for the blackish quartzites and phyllites. Based on this age signature and the magmatic texture of the zircons, it is proposed that also this population of grains can be correlated to the main igneous phase of the Cadomian Orogeny. The fifth age group has a probability peak around 800 Ma. This peak is characterized by a continuous age distribution of grains between 727 and 986 Ma. The zircons within this age interval can possibly be correlated to the assembly of Rodinia (1300-900 Ma). According to Kröner et al. (2001), calc-alkaline intrusions with ages between 1040 and 929 Ma have been associated with the Kibaran Orogeny and the assembly of Rodinia. Also, 40-60 Ma after the final assembly of Rodinia, widespread rifting of the supercontinent took place. This resulted in three episodic plume events at approximately 825 Ma, 780 Ma and 750 Ma (Li et al., 2008). It is suggested, on the basis of the oscillatory zoning and age signature, that these zircons can be correlated to the African continent. The old grains in this sample tend to have a very complex internal structure, possibly a result of multiple phases of growth. The sixth age group is composed of five of the grains in the sample. These have Paleoproterozoic to Archean ages. As zircons of these ages are present in many continents, it is hard to conclusively identify the origin of these grains. However, based on the interpretation of the origin of the other zircons in this sample, an African origin is suggested. For the youngest part of this subpopulation, a correlation to the amalgamation

of the Columbia supercontinent may be proposed. For the older grains, it is possible that they can be correlated to Neoarchean granitoid emplacements in the Mozambique Belt. According to Muhongo et al. (2001), these granitoids have ages between 2608 and 2740 Ma.

Based on the age signature from this sample, it is suggested that the origin of the phyllites and metasiltstones can be correlated to the Iberian plate. For the older samples, it is likely that the zircons originated from the African continent because the Iberian plate was located at the northern Gondwana margin during Neoproterozoic times. Even though these correlations have been suggested, it is very hard to conclude on the oldest grains because grains of these ages are present on nearly all continents. However, because the younger zircons have been correlated to the Iberian plate, it is also suggested that the older ones are. A summary of the interpretations are shown in Fig. 48.

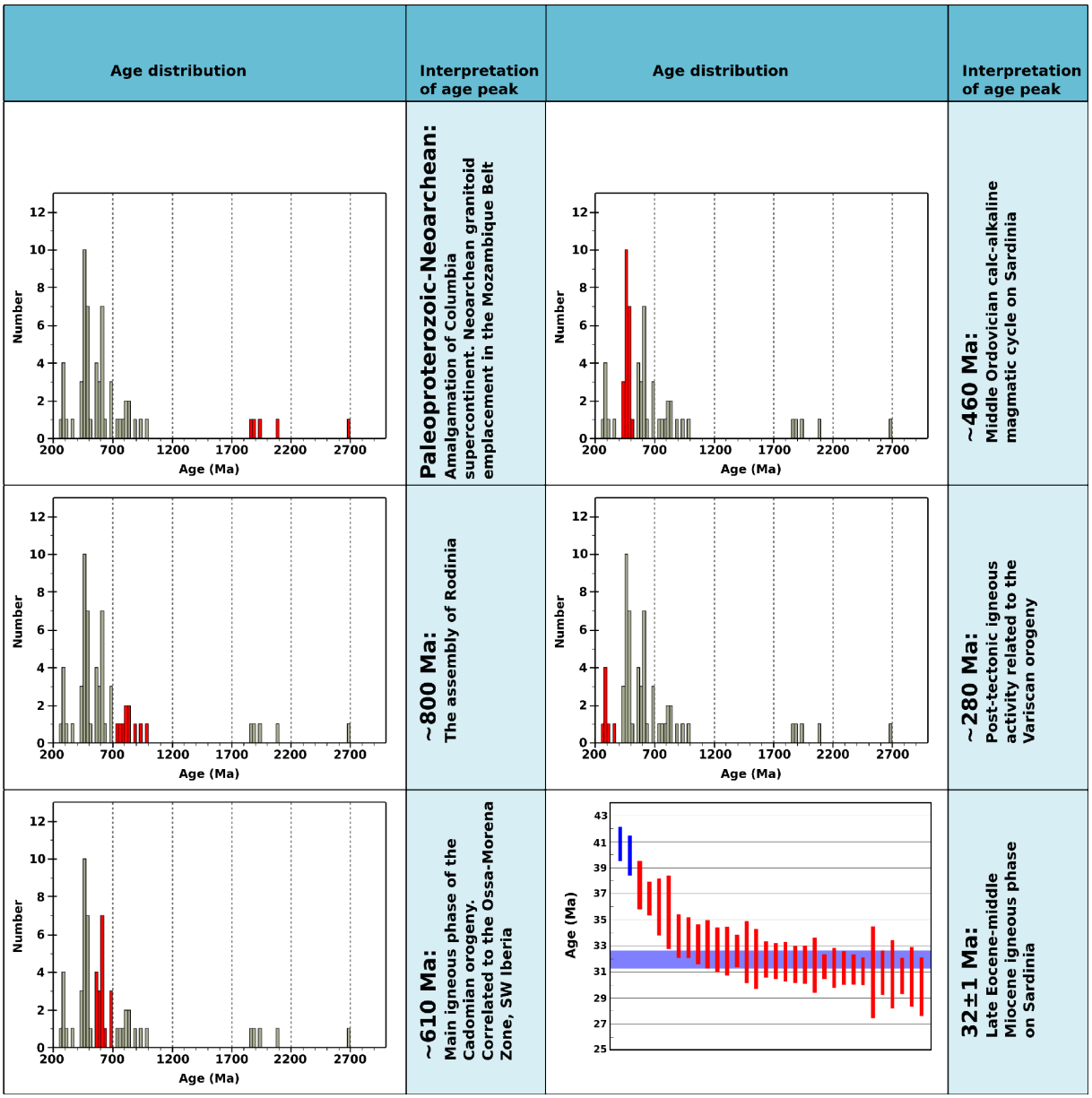

Fig. 48: Summary of the interpretations for the different zircon population. The age shown in the figure is representing the age of the probability peak. Red boxes represent ages belonging to the probability peak, while the green boxes does not represent that specific age population. The lowermost right plot presents the crystallization age with the blue band. Box heights are 1σ. Red boxes are interpreted as belonging to the same magmatic event, while the blue boxes are interpret as being xenocrystic.

7.3 Monticiano-Roccastrada Unit

The analysed samples from the Monticiano-Roccastrada Unit are from the Rio Marina (EHS-06) and Verruca (EHS-05) formations. By comparing the age distribution of these two samples (Fig. 49) with the samples from the Ortano Unit, it is evident that these samples show a much more complicated and dispersed age distribution (Fig. 44). Bortolotti et al. (2001a) have proposed that the Monticiano-Roccastrada Unit spans from Carboniferous to a Paleogene age. The Rio Marina and Verruca formations are the two lowermost lithologies in the Monticiano-Roccastrada Unit with suggested Cretaceous-Permian and Triassic ages, respectively (Bortolotti et al., 2001a).

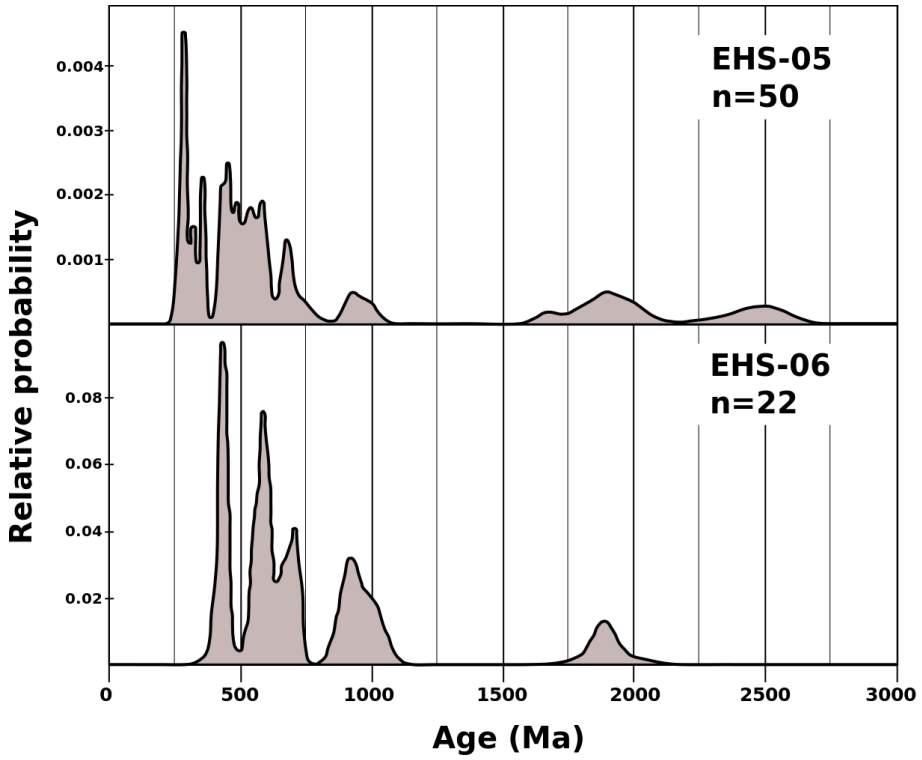

Fig. 49: Comparison of the probability density plots for the analysed samples in the Monticiano-Roccastrada Unit in Complex III. EHS-05 represents the Verruca Formation and EHS-06 represents the Rio Marina Formation.

The zircons from the Rio Marina Formation that passed the data filtering show either oscillatory zoning or zoning parallel to the c-axis of the grain. Based on the internal structure, all accepted zircons from this lithology are interpreted as the product of continuous magmatic growth. The morphology spans from idiomorphic to well rounded, indicating variable amount of transportation. Based on the age of the zircons in the Rio Marina Formation, three subpopulations can be distinguished. 71% of the grains comprise the first group, spanning from 420 to 750 Ma. With decreasing relative probability, probability peaks at 430 Ma, 590 Ma and 700 Ma are present within this subpopulation. 19% of the zircons yielded ages within the second age group. This group has an age peak around 930 Ma and reaches from 850 to 1050 Ma. The last age group is composed of two Paleoproterozoic grains with ages of 1890 Ma and 1906 Ma, resulting in an age peak around 1900 Ma.

The Verruca Formation contains zircons that are mainly oscillatory zoned or have zoning parallel

to the c-axis. Sector zoning may be present in one of the accepted grains, but the zonation in that specific grain is very weak so it will not be given further attention. Also, Corfu et al. (2003) present zircons with sector zoning interpreted as magmatic zircons. It is therefore interpreted that the source of the zircons in this sample is magmatic. Based on the U/Pb ages of the 50 concordant zircons from the Verruca Formation, a complex age distribution is present for the zircons, spanning from 259 to 2562 Ma. Based on the age, three subpopulations have been identified. 75% of the grains are included in the youngest age group. This age group shows an almost continuous age distribution between 259 and 991 Ma. Compared to the older age groups, this age group shows a complex age distribution with probability peaks present around 280 Ma, 360 Ma, 450 Ma, 580 Ma, 680 Ma and 940 Ma. The rest of the zircons can be put in the age group between 1676 and 2024 Ma or in the age group between 2380 and 2562 Ma with probability peaks around 1930 and 2500 Ma, respectively.

By comparing the age distribution of the zircons in the Verruca and Rio Marina formations in the Monticiano-Roccastrada Unit, it is evident that the age distribution in the Verruca Formation appear much more complex than in the Rio Marina Formation (Fig. 49). All populations that are present in the Rio Marina Formation are also present in the Verruca Formation. In addition to peaks of the same age as in the Rio Marina Formation, zircons in the Verruca Formation also have ages responsible for two younger peaks. A larger portion of grains with ages above 1500 Ma is also present in the Verruca Formation. As none or very few of the zircons have been interpreted as being metamorphic, all ages given for the samples analysed in the Monticiano-Roccastrada Unit are believed to be corresponding to magmatic events. Because of the stratigraphic position for the Rio Marina and Verruca formations, it is very likely that zircons with the same age are derived from the same source. The youngest zircon populations from the Monticiano-Roccastrada Unit analysed in this study are both from the Verruca Formation, represented by age peaks around 280 Ma and 360 Ma. The 280 Ma peak can be correlated to the 280 Ma peak that is present in the phyllites and metasiltstones in the Acquadolce Unit. Similarly, it can be correlated to the post-tectonic igneous activity related to the Variscan Orogeny in the Iberian Massif that is suggested by Fernández-Suárez et al. (2000). The second probability peak is located around 360 Ma, including grains with ages between 350 and 359 Ma. Romeo et al. (2006) have earlier suggested that the Cala granite (352±4 Ma) in the Ossa-Morena Zone in SW-Iberia was a result of an early magmatic pulse from the same source as the Santa Olalla Complex in the same region. Therefore, a possible correlation to this event is suggested. Both samples obtained from the Monticiano-Roccastrada Unit have age peaks around 430 Ma (Rio Marina Formation) and 450 Ma (Verruca Formation). Based on the magmatic signature of the internal structure and the similarity in age with all of the other analysed samples in the present study, a correlation to the Cambro-Silurian magmatic cycles on Sardinia is proposed. It is suggested that the subpopulation within these two formations can be correlated to the uppermost Ordovician-lowermost Silurian alkaline volcanic event, described by Oggiano et al. (2010) and Gaggero et al. (2012).

Both samples have peaks around 580-590 Ma. It is here interpreted that these zircons come from the same source as the 610-620 Ma grains from the phyllites and metasiltstones and the blackish quartzites and phyllites, respectively. The grains responsible for these peaks in the Verruca and Rio Marina formations are slightly younger than in the stratigraphically lower units dated, but

they are overlapping within their error margins. The main magmatism related to the Cadomian Orogeny happened between approximately 587 and 532 Ma, represented in the Ossa-Morena Zone in SW Iberia. It is likely that the zircons dated from the Monticiano-Roccastrada Unit are erosional products of an early phase of this magmatism.

The Verruca and Rio Marina formations show probability peaks between 680 and 700 Ma. Kröner et al. (2001) carried out a study in the Mozambique Belt, revealing two distinct magmatic events at 1040-929 Ma and 710-555 Ma and a long-lasting thermal peak of high-grade metamorphism during 571-549 Ma. It is here suggested that the zircons that are responsible for the probability peaks at 680 and 700 Ma can be correlated to the second of the magmatic events in the Mozambique Belt.

The next probability peaks in the samples from the Monticiano-Roccastrada Unit are located around 930 and 940 Ma for the Rio Marina Formation and the Verruca Formation, respectively. In the Rio Marina Formation, this age peak is a result of the continuous age distribution between 888 and 1020 Ma, while the probability peak in the Verruca Formation is a result of an age distribution between 921 and 991. During the assembly of Rodinia and the Kibaran Orogeny, calc-alkaline intrusions were emplaced. According to Kröner et al. (2001), these were emplaced between 1040 and 929 Ma. By looking at the ages and the respective errors of the zircons in this subpopulation, it can be seen that the ages of the grains are all within the age range of the emplacement of the intrusions. Based on the internal structure, the origin of the zircons have been interpreted as magmatic. Due to the internal structure and the age, it is suggested that the zircons are erosional products of the calc-alkaline intrusions of the Kibaran Orogeny during the assembly of Rodinia.

A Paleoproterozoic component is clearly present in both lithologies. The Rio Marina Formation has two grains with ages around 1900 Ma, while seven zircons between 1676 and 2024 Ma are included in the Verruca Formation. All zircons within this age group show zonation that is associated with magmatic growth. Similar to the zircons in the phyllites and metasiltstones, it is very hard to be conclusive about the origin of these zircons due to the high age and because they are present on nearly all continents. Because of the correlation of the younger zircons with the Iberian Massif, it is likely that these old zircons are derived from the pre-Iberia area. A correlation to the assembly of the Columbia Supercontinent is therfore suggested. The Columbia Supercontinent assembled between 2.1 and 1.8 Ga during large-scale collisions between Archean cratons (Rogers and Santosh, 2002; Zhao et al., 2002, 2003; Santosh, 2010). In addition to the Paleoproterozoic subpopulation, an early Paleoproterozoic-Neoarchean component is also present in the Verruca Formation. It is also hard to conclude on the source for this component, but it is interpreted that, on the basis of the other sedimentary sources within this unit, these zircons are derived from one of the early Paleoproterozoic-Neoarchean cratons of the African continent. There are very few Archean cratons in northern Africa. The Saharan Metacraton is composed of the Tuareg Shield, the Congo Craton and the Phanerozoic cover of the northern African margin (Abdelsalam et al., 2002). U/Pb ages around 2.5 Ga have been reported for the Saharan Metacraton (Abdelsalam et al., 2002, and references therein). Based on the ages of the Paleoproterozoic-Neoarchean grains, a possible correlation to the Saharan Metacraton is suggested, even though it is hard to conclude on such old grains and the limited amount of data.

Based on the fossil content and the parallel to planar cross-bedded laminations, the Rio Marina Formation has earlier been interpreted as a littoral-deltaic deposition of a late Carboniferous-early Permian age (Bortolotti et al., 2001a; Elter and Pandeli, 2001). The three youngest grains present in the sample from the Rio Marina Formation have ages of 420±14, 421±38 and 429±18 Ma. This is interpreted to be the maximum deposition age, indicating that the deposition of the sediment must have happened earliest during latest Silurian times. However, by comparing this age with the age suggested earlier by Bortolotti et al. (2001a) and Elter and Pandeli (2001), it can be seen that the maximum age of deposition from the present study is much older than what is suggested before. Because the U/Pb dating of the zircons in this study only provide an earlier maximum age of deposition than what is suggested previously, they cannot be used to obtain a better constraint on the age of deposition. Thus, the ages given by Bortolotti et al. (2001a) and Elter and Pandeli (2001) must still be regarded as valid.

The Verruca Formation on Elba Island was first correlated with the "Scisti violetti" and "Anageniti minute" members in the Verruca Formation in Mt. Pisani in the mainland of Tuscany by Rau and Tongiorgi (1974*; in* Bortolotti et al., 2001a). These members were interpreted as meandering river deposits of late Ladinian-Carnian age. The sample from this study contains zircons where the three lowest ages are 259±11, 278±16 and 280±14 Ma. Based on this, the deposition must have happened earliest during upper Permian-Lower Triassic times. The earliest possible depositional age proposed in this study is slightly older than the Middle-Upper Triassic age suggested by Rau and Tongiorgi (1974*; in* Bortolotti et al., 2001a). It is therefore proposed that the deposition of the sediments happened earliest during Lower Triassic times. Because it is not possible to get a better constraint than the earliest possible depositional age, the age proposed by Rau and Tongiorgi (1974*; in* Bortolotti et al., 2001a) cannot be disregarded. Also, if the Middle-Upper Triassic age is correct, it can be assumed that the sediments have been transported only a short distance. This argument supports the hypothesis that the zircons can be related to the post-tectonic igneous activity related to the Variscan Orogeny in the Iberian Massif. A summary of the interpretations for the Rio Marina and Verruca formations are presented in Fig. 50.

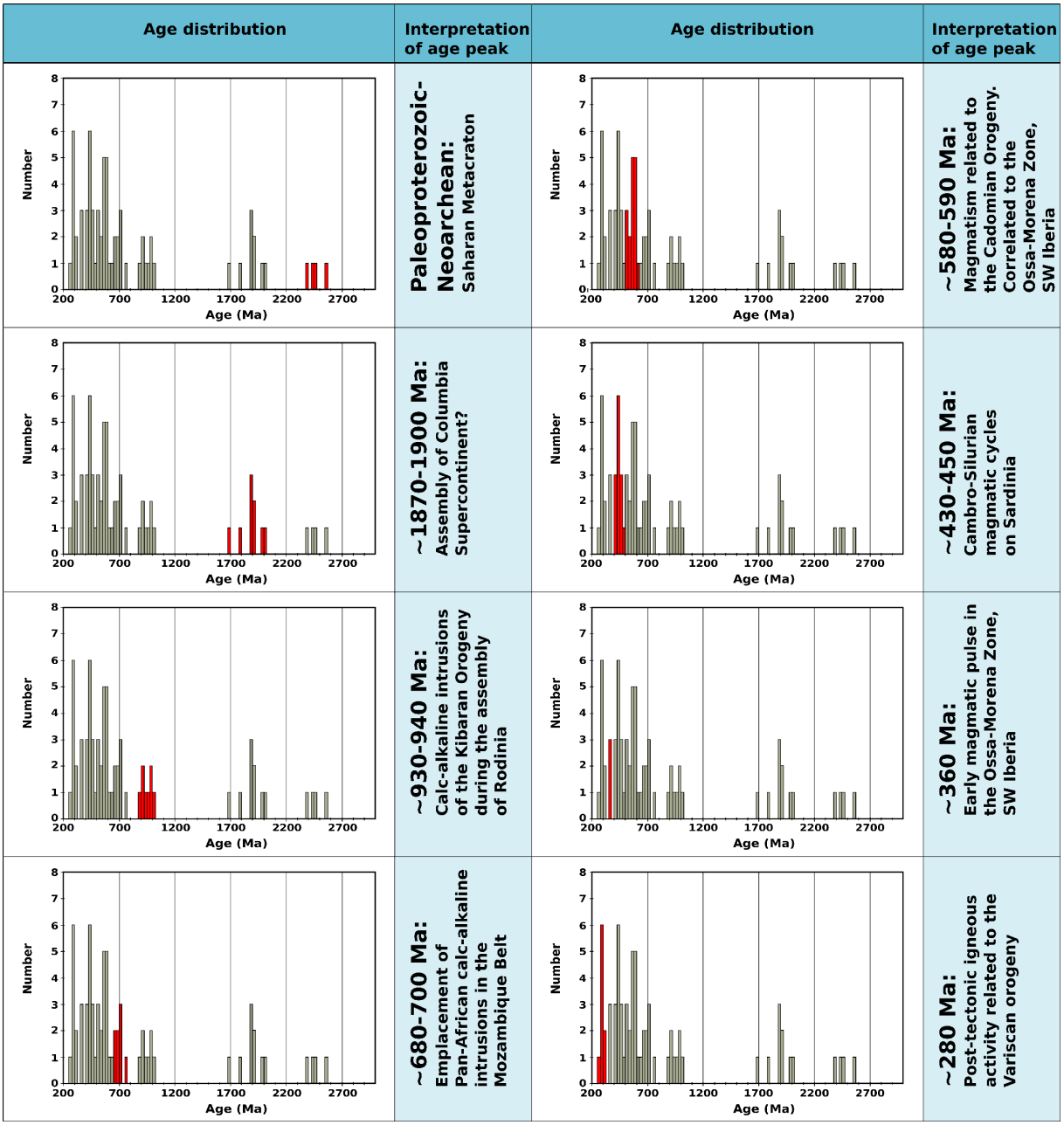

Fig. 50: Overview of the interpretations of the different zircons populations present in the Rio Marina and Verruca formations. Red boxes represent ages of grains that are correlated to the specific event. The other boxes represent ages that are associated with other events.

7.4 General interpretation

The interpretation of the present study is summarized in the following figures. Fig. 51 presents the interpreted Triassic-Paleogene situation, while Fig. 52 presents the situation for the Ordovician-Permian sediments.

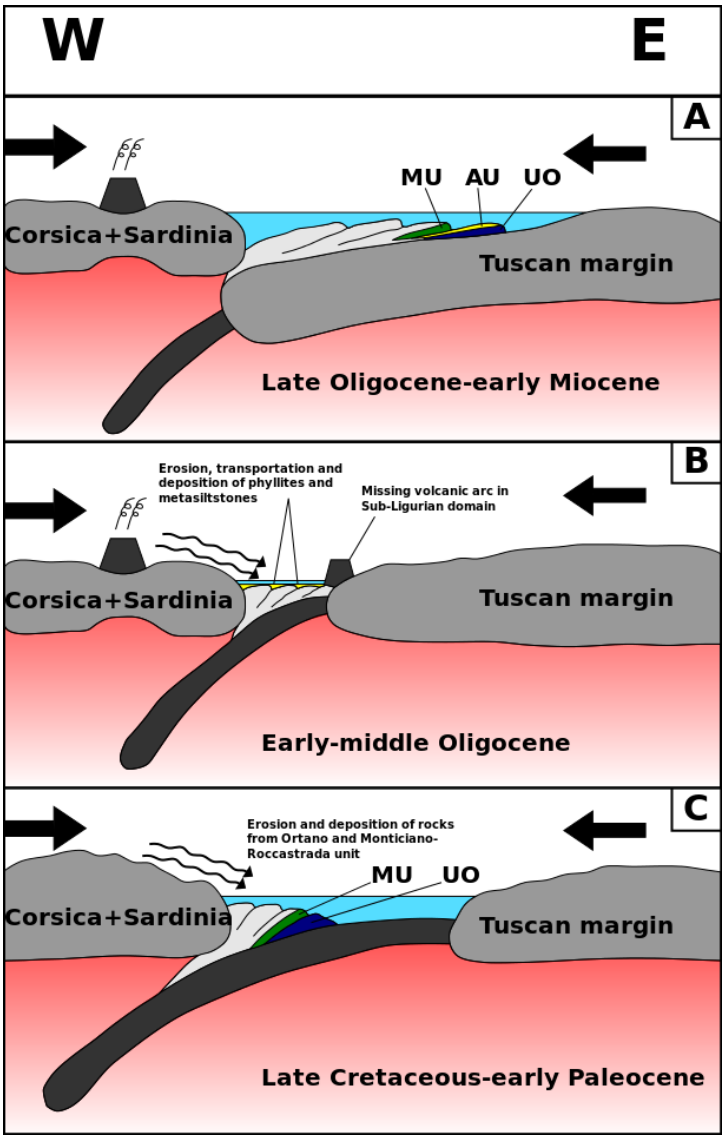

Fig. 51: Simplified schematic reconstruction of the late Cretaceous-early Miocene evolution of Corsica-Sardinia. Wavy arrows represent erosion and transportation of sediments. **UO:** Ortano Unit (blue); **AU:** Acquadolce Unit (yellow); **MU:** Monticiano-Roccastrada Unit (green). **a)** Continent-continent collision between the Corsica-Sardinia margin and the Tuscan margin during late Oligocene-early Miocene. The pile of sediments are thrusted onto the Tuscan margin**; b)** Early-middle Oligocene phase of the accretionary stage described by e.g. Bortolotti et al. (2001). The zircon population with an age of 32±1 Ma are erosional products of the magmatic activity on Corsica-Sardinia; **c)** late Cretaceous-early Paleocene reconstruction. Erosion from the Corsican-Sardinian and Tuscan margins resulted in deposition of sediments on the Alpine Tethys ocean floor. Convergence between the two margins resulted in accretion of sediments along the Corsican-Sardinian margin.

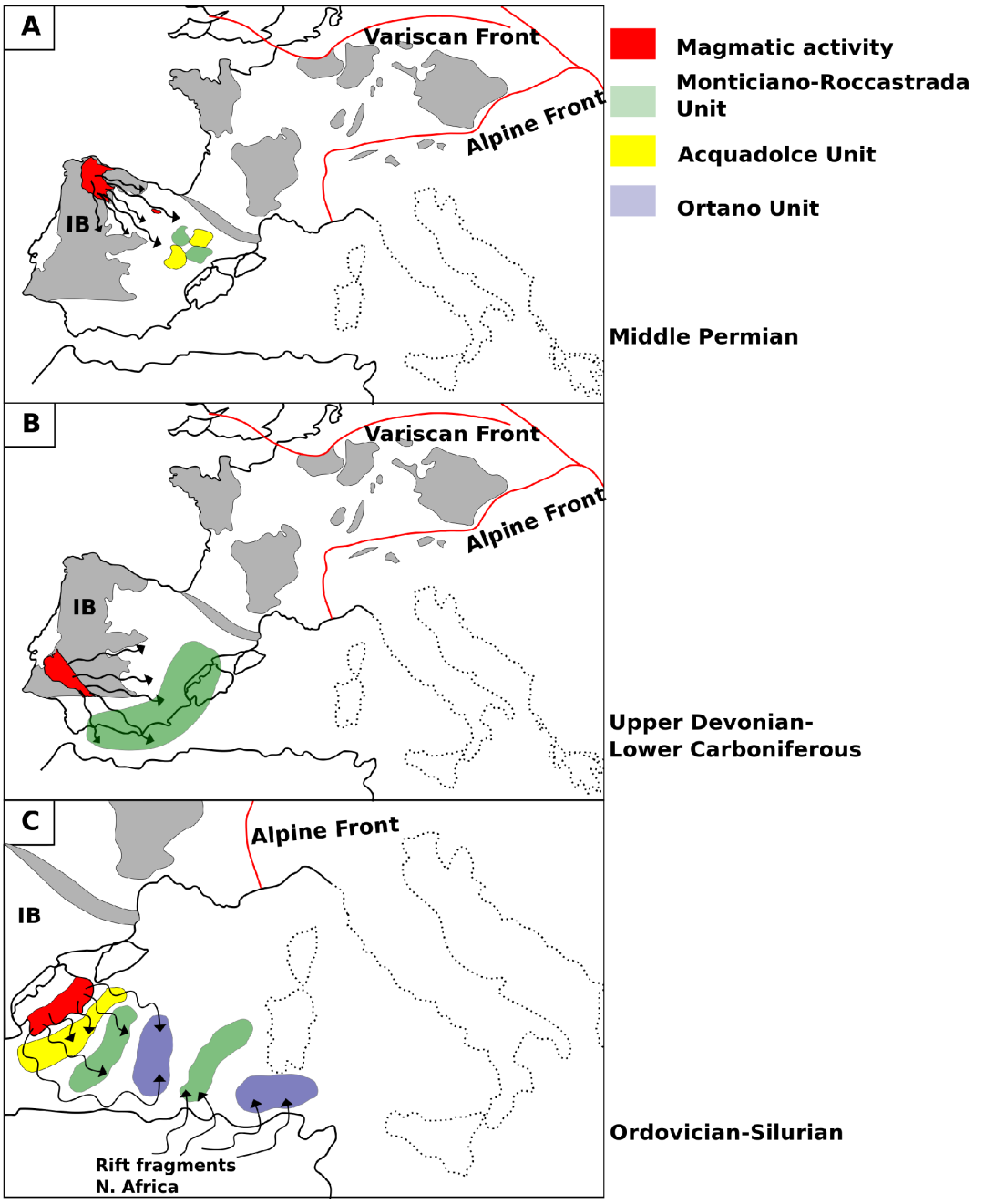

Fig. 52: Schematic Ordovician-Permian reconstruction used for illustrating the principle of the sediment provenance. Corsica-Sardinia have been rotated back to its pre-rotation position along the Iberian margin. Stippled lines show the present day location of Corsica and Italy for illustrational purposes. Red areas represent areas of magmatic activity, wavy arrows represent transportation of sediments, blue, yellow and green areas represent the areas of deposition for the Ortano, Acquadolce and Monticiano-Roccastrada units, respectively. **IB:** Iberian Massif. **a)** Erosion, transport and deposition of the sediments derived from the post-tectonic igneous activity of the Variscan orogeny in the West Asturian-Leonese Zone (NW Iberia). Only the Verruca Formation and the phyllites and metasiltstones contain zircons derived from this source; **b)** Early magmatic pulse in the Ossa-Morena Zone (SW Iberia). Sediments correlated to the Verruca Formation are interpreted as being deposited along the margin of Iberian Massif; **c)** Ordovician-Silurian magmatic cycle on Sardinia consisting of three phases. It is interpreted that these sediments were deposited to the E-SE of Corscia-Sardinia. In addition, rift fragments derived from the North African margin are deposited north of the margin.

8 Conclusion

The results from the present study reveal the age distributions and important age constraints for the Ortano, Acquadolce and Monticiano-Roccastrada units in the cover sequence of the Tuscan basement on Elba Island. U/Pb zircon dating provide new insights into the deposition- and crystallization ages for selected metasedimentary units within Complex II and III on eastern Elba. The following conclusions can be drawn from the present study:

- The age distributions get more complex upwards in the metasedimentary sequence of the cover units of the Tuscan basement, from a unimodal to polymodal age distribution. The lowermost lithologies are mainly derived from a single, possibly local source, while the uppermost lithologies are derived from multiple sources.
- A crystallization age of 422±8 Ma has been established for the source rock of the quartzophyllitic Capo d'Arco Schist on the basis U/Pb zircon dating. Due to this, and the three youngest grains in the biotite-rich micaschist, a maximum age of deposition of the Capo d'Arco Schists are placed at the Lower Devonian. An uppermost Silurian age has been established as the maximum age for deposition of the blackish quartzites and phyllites, based on the three youngest grains.
- A distinct subpopulation of late Eocene-early Oligocene age has been detected within the phyllites and metasiltstones. This indicates an igneous source with a crystallization age of 32±1 Ma. Therefore this unit must be much younger than the previously suggested upper part of Lower Cretaceous age. A maximum deposition age of late Eocene-early Oligocene times, possibly correlated with the late Eocene-middle Miocene Sardinian igneous phase is suggested.
- The previously suggested late Carboniferous-early Permian and Middle-Upper Triassic deposition ages for the Rio Marina and Verruca formations, respectively, are supported in this study on the basis of the three youngest grains in the both formations.
- It has previously been suggested that the Capo d'Arco Schists and the silver-grey phyllites and quartzites originally represented a single horizon that has been isoclinally folded with the Ortano Porphyroids in its core. This hypothesis is supported due to the age similarity between the silver-grey phyllites and quartzites and the Capo d'Arco Schists presented in this study, as well as in other studies.
- The magmatic internal structure and the age signatures suggest a correlation to magmatic events on the African continent, the Iberian Massif and Sardinia. The zircons are, most likely, derived from the late Eocene-middle Miocene igneous phase on Sardinia, emplacement of calc-alkaline dykes in the Iberian Massif, granite emplacement in the Ossa-Morena Zone (SW Iberia), the upper Cambrian-early Silurian magmatic cycles on Sardinia, the main igneous phase of the Cadomian orogeny, Pan-African intrusions in the Mozambique Belt and intrusions related to the Kibaran orogeny during the assembly of Rodinia. Some of the oldest zircons are probably derived from the Saharan Metacraton and from the rocks that formed during assembly of Columbia.

9 Future work

The present study has provided useful constraints when it comes to the age of the cover sequence of the Tuscan basement on Elba Island. By now, all lithologies within the Ortano Unit have been fairly well constrained by U/Pb dating of zircons. Possibly, other samples from different localities within the Ortano Unit could be analysed in order to strengthen the conclusions that have been drawn in this and previous studies. A crystallization age has been calculated for the quartzo-phyllitic Capo d'Arco Schist in the present study with the use of the TuffZirc algorithm (Ludwig and Mundil, 2002). It would therefore be interesting to analyse zircons from this sample further with i.e. SIMS or TIMS in order to obtain an even more precise age for the crystallization of the protolith of the sediment.

It has previously been suggested that the Ortano Unit is mainly a large, isoclinal fold with the Ortano Porphyroids as the core. Even though this is supported by this and other, previous studies, it is suggested that the Ortano Unit should be given more attention. Detailed structural mapping could be used to reveal the deformation processes within the Ortano Unit.

The analyses of the phyllites and metasiltstones yielded rather unexpected, yet very interesting results. The unexpected, young age component of 32±1 Ma should be studied in more detail. Zircons from new samples within the same lithology should be analysed in order to check the validity of the results. This population has a similar age than the volcanoclastic deposits in the Val d'Aveto and Petrignacola sandstone formations in northern Italy, but also as the late Eocene-middle Miocene metavolcanic rocks on Sardinia. The analytical set-up used in this study is well suited for rapidly providing the large amounts of data that are required for provenance studies, which also was the target for this study. However, this set-up is not well suited for providing crystallization ages or very precise analyses for such young grains. Because it was not the purpose of analysing such grains, it is suggested that more precise crystallization ages should be provided by SIMS or TIMS. It is also suggested that zircons from these localities should be analysed with respect to hafnium isotopes and trace elements in order to test a potential common source for igneous activity. This could be used to get a better constraint on the correlation between the lithologies.

The Verruca Formation in the Monticiano-Roccastrada Unit is composed of different lithotypes, and it is suggested that these are similar to the Verrucano sequence in Mt. Pisani. It is suggested that a variety of these lithotypes should be sampled and compared with the lithotypes in the Verrucano sequence that has previously been correlated with the Verruca Formation.

10 References

Abbate, E., and Sagri, M., 1982, Le unità torbiditiche Cretacee dell'Appennino settentrionale ed i margini continentali della Tetide: Memoire della Società Geologica Italiana, v. 24, no. 2, p. 115–126.

Abdelsalam, M.G., Liégeois, J.P., and Stern, R.J., 2002, The Saharan Metacraton: Journal of African Earth Sciences, v. 34, no. 3–4, p. 119–136, doi:10.1016/S0899-5362(02)00013-1.

Alvarez, W., 1972, Rotation of the Corsica–Sardinia microplate: Nature, v. 235, no. 58, p. 103–105.

Andersen, T., 2005, Detrital zircons as tracers of sedimentary provenance: limiting conditions from statistics and numerical simulation: Chemical Geology, v. 216, no. 3-4, p. 249–270.

Barberi, F., Gasparini, P., Innocenti, F., and Villari, L., 1973, Volcanism of the southern Tyrrhenian Sea and its geodynamic implications: Journal of Geophysical Research, v. 78, no. 23, p. 5221–5232.

Barberi, F., Innocenti, F., and Ricci, C.A., 1967, Il complesso scistoso di Capo Calamita (Isola d'Elba): Atti Soc. Tosc. Sci. Nat., Mem., Serie A, v. 74, p. 579–617.

Barnes, J.D., Selverstone, J., and Sharp, Z.D., 2006, Chlorine isotope chemistry of serpentinites from Elba, Italy, as an indicator of fluid source and subsequent tectonic history: Geochemistry Geophysics Geosystems, v. 7, no. 8, p. 14.

Bartole, R., 1995, The North Tyrrhenian-Northern Apennines postcollisional system: constraints for a geodynamic model: Terra Nova, v. 7, no. 1, p. 7–30.

Beccaluva, L., Civetta, L., Macciotta, G., and Ricci, C.A., 1985, Geochronology in Sardinia: results and problems: Rendiconli della Società Italiana di Mineralogia e Petrologia, v. 40, p. 57–72.

Behr, H.J., Engel, W., Franke, W., Giese, P., and Weber, K., 1984, The Variscan Belt in Central Europe: Main structures, geodynamic implications, open questions: Tectonophysics, v. 109, no. 1–2, p. 15–40, doi:10.1016/0040-1951(84)90168-9.

Benvenuti, M., Bortolotti, V., Fazzuoli, M., Pandeli, E., and Principi, G., 2001, B - Eastern Elba: Ofioliti, v. 26, no. 2A, p. 331–345.

Bingen, B., Demaiffe, D., and van Breemen, O., 1998, The 616 Ma old Egersund basaltic dike swarm, SW Norway, and Late Neoproterozoic opening of the Iapetus Ocean: The Journal of Geology, v. 106, no. 5, p. 565–574.

Bingen, B., Jacobs, J., Viola, G., Henderson, I.H.C., Skaar, Ø., Boyd, R., Thomas, R.J., Solli, A., Key, R.M., and Daudi, E.X.F., 2009, Geochronology of the Precambrian crust in the Mozambique belt in NE Mozambique, and implications for Gondwana assembly: Precambrian Research, v. 170, no. 3–4, p. 231–255, doi:10.1016/j.precamres.2009.01.005.

Black, R., and Liegeois, J.P., 1993, Cratons, mobile belts, alkaline rocks and continental lithospheric mantle: the Pan-African testimony: Journal of the Geological Society, v. 150, no. 1, p. 89–98, doi:10.1144/gsjgs.150.1.0088.

Boccaletti, M., Coli, M., Decandia, F.A., Giannini, E., and Lazzarotto, A., 1980, Evoluzione dell'Appennino settentrionale secondo un nuovo modello strutturale: Mem. Soc. Geol. It, v. 21, p. 359–373.

Bortolotti, V., Fazzuoli, M., Pandeli, E., Principi, G., Babbini, A., and Corti, S., 2001a, Geology of central and eastern Elba Island, Italy: Ofioliti, v. 26, no. 2A, p. 97–150.

Bortolotti, V., Pandeli, E., and Principi, G., 2001b, The geology of the Elba Island: an historical introduction: Ofioliti, v. 26, no. 2A, p. 79–96.

Brunet, C., Monié, P., Jolivet, L., and Cadet, J.P., 2000, Migration of compression and extension in the Tyrrhenian Sea, insights from 40Ar/39Ar ages on micas along a transect from Corsica to Tuscany: Tectonophysics, v. 321, no. 1, p. 127–155.

Carmignani, L., Giglia, G., and Kligfield, R., 1978, Structural evolution of the Apuane Alps: an example of continental margin deformation in the northern Apennines, Italy: The Journal of Geology, v. 86, no. 4, p. 487–504.

Carmignani, L., and Kligfield, R., 1990, Crustal extension in the Northern Apennines: the transition from compression to extension in the Alpi Apuane core complex: Tectonics, v. 9, no. 6, p. 1275–1303.

Carrigan, C.W., Mukasa, S.B., Haydoutov, I., and Kolcheva, K., 2005, Age of Variscan magmatism from the Balkan sector of the orogen, central Bulgaria: Lithos, v. 82, no. 1–2, p. 125–147, doi:10.1016/j.lithos.2004.12.010.

Cavazza, W., and Wezel, F.C., 2003, The Mediterranean region - a geological primer: Episodes, v. 26, no. 3, p. 160–168.

Condie, K.C., 2003, Supercontinents, superplumes and continental growth: the Neoproterozoic record: Geological Society, London, Special Publications, v. 206, no. 1, p. 1–21, doi:10.1144/GSL.SP.2003.206.01.02.

Conti, P., Pisa, A., Gattiglio, M., and Meccheri, M., 1993, The Pre-Alpine Basement in the Alpi Apuane (Northern Apennines, Italy), *in* Raumer, J.F., and Neubauer, F., eds., Pre-mesozoic geology in the alps: Springer Berlin Heidelberg, p. 609–621.

Cordani, U.G., D'Agrella-Filho, M.S., Brito-Neves, B.B., and Trindade, R.I.F., 2003, Tearing up Rodinia: the Neoproterozoic palaeogeography of South American cratonic fragments: Terra Nova, v. 15, no. 5, p. 350–359, doi:10.1046/j.1365-3121.2003.00506.x.

Corfu, F., Hanchar, J.M., Hoskin, P.W.O., and Kinny, P., 2003, Atlas of Zircon Textures: Reviews in Mineralogy and Geochemistry, v. 53, no. 1, p. 469–500, doi:10.2113/0530469.

Dalziel, I.W.D., M., S., and Gahagan, L.M., 2000, Laurentia-Kalahari collision and the assembly of Rodinia: The Journal of Geology, v. 108, no. 5, p. 499–513.

Davis, D.W., Krogh, T.E., and Williams, I.S., 2003, Historical development of zircon geochronology: Reviews in mineralogy and geochemistry, v. 53, no. 1, p. 145–181, doi:10.2113/0530145.

Dercourt, J., Zonenshain, L.P., Ricou, L.E., Kazmin, V.G., Le Pichon, X., Knipper, A.L., Grandjacquet, C., Sbortshikov, I.M., Geyssant, J., Lepvrier, C., Pechersky, D.H., Boulin, J., Sibuet, J.C., Savostin, L.A., Sorokhtin, O., Westphal, M., Bazhenov, M.L., Lauer, J.P., and Biju-Duval, B., 1986, Geological evolution of the Tethys belt from the Atlantic to the Pamirs since the LIAS: Tectonophysics, v. 123, no. 1–4, p. 241 – 315.

Dewey, J.F., Helman, M.L., Knott, S.D., Turco, E., and Hutton, D.H.W., 1989, Kinematics of the western Mediterranean: Geological Society, London, Special Publications, v. 45, no. 1, p. 265–283.

Dini, A., Benvenuti, M., Costagliola, P., and Lattanzi, P., 2001, Mercury deposits in metamorphic settings: the example of Levigliani and Ripa mines, Apuane Alps (Tuscany, Italy): Ore Geology Reviews, v. 18, no. 3–4, p. 149–167, doi:10.1016/S0169-1368(01)00026-9.

Dini, A., Innocenti, F., Rocchi, S., Tonarini, S., and Westerman, D.S., 2002, The magmatic evolution of the late Miocene laccolith-pluton-dyke granitic complex of Elba Island, Italy: Geological Magazine, v. 139, no. 3, p. 257–279.

Dunstan, L.P., Gramlich, J.W., Barnes, I.L., and Purdy, W.C., 1980, Absolute isotopic abundance and the atomic weight of a reference sample of thallium: J. Res. Natl. Bur. Stand., v. 85, no. 1, p. 1–10, cited from Kosler (mail).

Duranti, S., Palmeri, R., Pertusati, P.C., and Ricci, C.A., 1992, Geological evolution and metamorphic petrology of the basalt sequences of eastern Elba (Complex II): Acta Vulcanologica, v. 2, p. 213–229.

Eggins, S.M., Kinsley, L.P.J., and Shelley, J.M.G., 1998, Deposition and element fractionation processes during atmospheric pressure laser sampling for analysis by ICP-MS: Applied Surface Science, v. 127–129, p. 278–286, doi:10.1016/S0169-4332(97)00643-0.

Elter, F.M., and Pandeli, E., 2001, Structural evolution of anchi-/epimetamorphic units of Central and Eastern Elba (Ortano, Acquadolce, Monticiano-Roccastrada and Grassera Units): Ofioliti, v. 26, no. 2A, p. 219–228.

Elter, P., Grasso, M., Parotto, M., and Vezzani, L., 2003, Structural setting of the Apennine-Maghrebian thrust belt: Episodes, v. 26, no. 3, p. 205–211.

Emmel, B., Jöns, N., Kröner, A., Jacobs, J., Wartho, J.A., Schenk, V., Razakamanana, T., and Austegard, A., 2008, From closure of the Mozambique Ocean to Gondwana breakup: new evidence from geochronological data of the Vohibory Terrane, southwest Madagascar: The Journal of Geology, v. 116, no. 1, p. 21–38, doi:10.1086/524121.

Favre, P., and Stampfli, G.M., 1992, From rifting to passive margin: the examples of the Red Sea, Central Atlantic and Alpine Tethys: Tectonophysics, v. 215, no. 1, p. 69–97.

Fedo, C.M., Sircombe, K.N., and Rainbird, R.H., 2003, Detrital zircon analysis of the sedimentary record: Reviews in Mineralogy and Geochemistry, v. 53, no. 1, p. 277–303, doi:10.2113/0530277.

Fernández-Suárez, J., Arenas, R., Jeffries, T.E., Whitehouse, M.J., and Villaseca, C., 2006, A U-Pb Study of Zircons from a Lower Crustal Granulite Xenolith of the Spanish Central System: A Record of Iberian Lithospheric Evolution from the Neoproterozoic to the Triassic: The Journal of Geology, v. 114, no. 4, p. 471–483.

Fernández-Suárez, J., Dunning, G.R., Jenner, G.A., and Gutiérrez-Alonso, G., 2000, Variscan collisional magmatism and deformation in NW Iberia: constraints from U–Pb geochronology of granitoids: Journal of the Geological Society, v. 157, no. 3, p. 565–576, doi:10.1144/jgs.157.3.565.

Fernández-Suárez, J., Gutiérrez-Alonso, G., Jenner, G.A., and Tubrett, M.N., 2000, New ideas on the Proterozoic-Early Palaeozoic evolution of NW Iberia: insights from U–Pb detrital zircon ages: Precambrian Research, v. 102, no. 3, p. 185–206, doi:10.1016/S0301-9268(00)00065-6.

Ferré, E., Gleizes, G., and Caby, R., 2002, Obliquely convergent tectonics and granite emplacement in the Trans-Saharan belt of Eastern Nigeria: a synthesis: Precambrian Research, v. 114, no. 3–4, p. 199–219, doi:10.1016/S0301-9268(01)00226-1.

Finetti, I.R., Boccaletti, M., Bonini, M., Del Ben, A., Geletti, R., Pipan, M., and Sani, F., 2001, Crustal section based on CROP seismic data across the North Tyrrhenian-Northern Apennines-Adriatic Sea: Tectonophysics, v. 343, p. 135–163.

Frisch, W., 1981, Plate motions in the Alpine region and their correlation to the opening of the Atlantic ocean: Geologische Rundschau, v. 70, no. 2, p. 402–411.

Fryer, B.J., Jackson, S.E., and Longerich, H.P., 1993, The application of laser ablation microprobe-inductively coupled plasma-mass spectrometry (LAM-ICP-MS) to in situ (U)-Pb geochronology: Chemical Geology, v. 109, no. 1–4, p. 1–8, doi:10.1016/0009-2541(93)90058-Q.

Gaggero, L., Oggiano, G., Funedda, A., and Buzzi, L., 2012, Rifting and arc-related early Paleozoic volcanism along the North Gondwana margin: geochemical and geological evidence from Sardinia (Italy): The Journal of Geology, v. 120, no. 3, p. 273–292, doi:10.1086/664776.

Galdeano, A., Moreau, M.G., Pozzi, J.P., Berthou, P.Y., and Malod, J.A., 1989, New paleomagnetic results from Cretaceous sediments near Lisboa (Portugal) and implications for the rotation of Iberia: Earth and Planetary Science Letters, v. 92, no. 1, p. 95 – 106, doi:10.1016/0012-821X(89)90024-1.

Garfagnoli, F., Menna, F., Pandeli, E., and Principi, G., 2005, The Porto Azzurro Unit (Mt. Calamita promontory, south-eastern Elba Island, Tuscany): Stratigraphic, tectonic and metamorphic evolution: Bollettino Della Societa Geologica Italiana, p. 119–138, garfagnoli, F Menna, F Pandeli, E Principi, G 3.

Garfunkel, Z., and Derin, B., 1984, Permian-early Mesozoic tectonism and continental margin formation in Israel and its implications for the history of the Eastern Mediterranean: Geological Society, London, Special Publications, v. 17, no. 1, p. 187–201.

Grunow, A.M., 1999, Gondwana events and palæogeography: A palæomagnetic review: Journal of African Earth Sciences, v. 28, no. 1, p. 53 – 69, doi:10.1016/S0899-5362(99)00019-6.

Gueguen, E., 1995, Le Bassin Liguro–Provençal: un véritable ocean. exemple de segmentation des marges et de hiatus cinématiques. Implications sur les processus d'amincissement crustal [Ph.D. thesis]: Brest University.

Gueguen, E., Doglioni, C., and Fernandez, M., 1998, On the post-25 Ma geodynamic evolution of the western Mediterranean: Tectonophysics, v. 298, p. 259–269.

Guillong, M., and Günther, D., 2002, Effect of particle size distribution on ICP-induced elemental fractionation in laser ablation-inductively coupled plasma-mass spectrometry: Journal of Analytical Atomic Spectrometry, v. 17, p. 831–837, doi:10.1039/B202988J.

Günther, D., and Heinrich, C.A., 1999, Enhanced sensitivity in laser ablation-ICP mass spectrometry using helium-argon mixtures as aerosol carrier: Journal of Analytical Atomic Spectroscopy, v. 14, no. 9, p. 1363–1368.

Gutiérrez-Alonso, G., Murphy, J.B., Fernández-Suárez, J., and M.A. Hamilton, M.A., 2008, Rifting along the northern Gondwana margin and the evolution of the Rheic Ocean: A Devonian age for the El Castillo volcanic rocks (Salamanca, Central Iberian Zone): Tectonophysics, v. 461, no. 1–4, p. 157–165, doi:10.1016/j.tecto.2008.01.013.

Hargrove, U.S., Stern, R.J., Kimura, J.I., Manton, W.I., and Johnson, P.R., 2006, How juvenile is the Arabian–Nubian Shield? Evidence from Nd isotopes and pre-Neoproterozoic inherited zircon in the Bi'r Umq suture zone, Saudi Arabia: Earth and Planetary Science Letters, v. 252, no. 3–4, p. 308–326, doi:10.1016/j.epsl.2006.10.002.

Helbing, H., and Tiepolo, M., 2005, Age determination of Ordovician magmatism in NE Sardinia and its bearing on Variscan basement evolution: Journal of the Geological Society, v. 162, no. 4, p. 689–700, doi:10.1144/0016-764904-103.

Hirata, T., and Nesbitt, R.W., 1995, U-Pb isotope geochronology of zircon: Evaluation of the laser probe-inductively coupled plasma mass spectrometry technique: Geochimica et Cosmochimica Acta, v. 59, no. 12, p. 2491–2500, doi:10.1016/0016-7037(95)00144-1.

Horn, I., Rudnick, R.L., and McDonough, W.F., 2000, Precise elemental and isotope ratio determination by simultaneous solution nebulization and laser ablation-ICP-MS: application to U-Pb geochronology: Chemical Geology, v. 164, no. 3–4, p. 281–301, doi:10.1016/S0009-2541(99)00168-0.

Hoskin, P.W.O., and Schaltegger, U., 2003, The composition of zircon and igneous and metamorphic petrogenesis: Reviews in Mineralogy and Geochemistry, v. 53, no. 1, p. 27–62, doi:10.2113/0530027.

Jackson, S.E., Pearson, N.J., Griffin, W.L., and Belousova, E.A., 2004, The application of laser ablation-inductively coupled plasma-mass spectrometry to in situ U–Pb zircon geochronology: Chemical Geology, v. 211, no. 1–2, p. 47–69, doi:10.1016/j.chemgeo.2004.06.017.

Jacobs, J., Bauer, W., and Fanning, C.M., 2003a, Late Neoproterozoic/Early Palaeozoic events in central Dronning Maud Land and significance for the southern extension of the East African Orogen into East Antarctica: Precambrian Research, v. 126, no. 1–2, p. 27–53, doi:10.1016/S0301-9268(03)00125-6.

Jacobs, J., Bingen, B., Thomas, R.J., Bauer, W., Wingate, M.T.D., and Feitio, P., 2008, Early Palaeozoic orogenic collapse and voluminous late-tectonic magmatism in Dronning Maud Land and Mozambique: insights into the partially delaminated orogenic root of the East African–Antarctic Orogen?: Geological Society, London, Special Publications, v. 308, no. 1, p. 69–90, doi:10.1144/SP308.3.

Jacobs, J., Fanning, C.M., Henjes-Kunst, F., Olesch, M., and Paech, H.J., 1998, Continuation of the Mozambique belt into East Antarctica: Grenville-age metamorphism and polyphase Pan-African high-grade events in Central Dronning Maud Land: The Journal of Geology, v. 106, no. 4, p. 385–406.

Jacobs, J., Klemd, R., Fanning, C.M., Bauer, W., and Colombo, F., 2003b, Extensional collapse of the late Neoproterozoic-early Palaeozoic East African-Antarctic Orogen in central Dronning Maud Land, East Antarctica: Geological Society, London, Special Publications, v. 206, no. 1, p. 271–287, doi:10.1144/GSL.SP.2003.206.01.14.

Johnson, P.R., and Woldehaimanot, B., 2003, Development of the Arabian-Nubian Shield: perspectives on accretion and deformation in the northern East African Orogen and the assembly of Gondwana: Geological Society, London, Special Publications, v. 206, no. 1, p. 289–325, doi:10.1144/GSL.SP.2003.206.01.15.

Johnson, S.D., Poujol, M., and Kisters, A.F.M., 2006, Constraining the timing and migration of collisional tectonics in the Damara Belt, Namibia: U-Pb zircon ages for the syntectonic Salem-type Stinkbank granite: South African Journal of Geology, v. 109, no. 4, p. 611–624, doi:10.2113/gssajg.109.4.611.

Jolivet, L., and Faccenna, C., 2000, Mediterranean extension and the Africa-Eurasia collision: Tectonics, v. 19, no. 6, p. 1095–1106.

Jolivet, L., Faccenna, C., Goffé, B., Mattei, M., Rossetti, F., Brunet, C., Storti, F., Funiciello, R., Cadet, J.P., d'Agostino, N., and Parra, T., 1998, Midcrustal shear zones in postorogenic extension: example from the northern Tyrrhenian Sea: Journal of Geophysical Research, v. 103, no. B6, p. 12,123–12.

Jørgensen, H., 2011, Structural analysis and geochronology of the Tuscan basement and the lowermost tectonic units of the Eastern Elba thrust nappes [Master's thesis]: University of Bergen, 96 p.

Kastens, K., Mascle, J., Auroux, C., Bonatti, E., Broglia, C., Channell, J., Curzi, P., Emeis, K.A.Y.C., Glaçon, G., Hasegawa, S., Hieke, W., Mascle, G., McCoy, F., McKenzie, J., Mendelson, J., Müller, C., Réhault, J.P., Robertson, A., Sartori, R., Sprovieri, R., and Torii, M., 1988, ODP Leg 107 in the Tyrrhenian Sea: Insights into passive margin and back-arc basin evolution: Geological Society of America Bulletin, v. 100, no. 7, p. 1140–1156.

Košler, J., Fonneland, H., Sylvester, P.J., Tubrett, M., and Pedersen, R.B., 2002, U–Pb dating of detrital zircons for sediment provenance studies - a comparison of laser ablation ICPMS and SIMS techniques: Chemical Geology, v. 182, no. 2, p. 605–618, doi:10.1016/S0009-2541(01)00341-2.

Košler, J., and Sylvester, P.J., 2003, Present trends and the future of zircon in geochronology: laser ablation ICPMS: Reviews in mineralogy and geochemistry, v. 53, no. 1, p. 243–275, doi:10.2113/0530243.

Kröner, A., Willner, A.P., Hegner, E., Jaeckel, P., and Nemchin, A., 2001, Single zircon ages, PT evolution and Nd isotopic systematics of high-grade gneisses in southern Malawi and their bearing on the evolution of the Mozambique belt in southeastern Africa: Precambrian Research, v. 109, no. 3–4, p. 257–291, doi:10.1016/S0301-9268(01)00150-4.

Lahondère, D., and Guerrot, C., 1997, Datation Sm-Nd du métamorphisme éclogitique en Corse Alpine: Un argument pour l'existence au Crétacé supérieur d'une zone de subduction active localisée sous le bloc corso-sarde: Géologie de la France, v. 3, p. 3–11.

LeCheminant, A.N., and Heaman, L.M., 1989, Mackenzie igneous events, Canada: Middle Proterozoic hotspot magmatism associated with ocean opening: Earth and Planetary Science Letters, v. 96, no. 1–2, p. 38–48, doi:10.1016/0012-821X(89)90122-2.

Li, Z.X., Bogdanova, S.V., Collins, A.S., Davidson, A., De Waele, B., Ernst, R.E., Fitzsimons, I.C.W., Fuck, R.A., Gladkochub, D.P., Jacobs, J., Karlstrom, K.E., Lu, S., Natapov, L.M., Pease, V., Pisarevsky, S.A., Thrane, K., and Vernikovsky, V., 2008, Assembly, configuration, and break-up history of Rodinia: A synthesis: Precambrian Research, v. 160, no. 1–2, p. 179–210, doi:10.1016/j.precamres.2007.04.021.

Ludwig, K.R., 2012, User's manual for Isoplot 3.75 – A geochronological toolkit for Microsoft Excel: Berkeley Geochronology Center: Special Publication, no. 5, p. 75.

Ludwig, K.R., and Mundil, R., 2002, Extracting reliable U-Pb ages and errors from complex populations of zircons from Phanerozoic tuffs: J. Conf. Abstr. 12th Goldschmidt Conf.

Lustrino, M., Morra, V., Fedele, L., and Franciosi, L., 2009, Beginning of the Apennine subduction system in central western Mediterranean: Constraints from Cenozoic "orogenic" magmatic activity of Sardinia, Italy: Tectonics, v. 28, no. 5, p. 23, doi:10.1029/2008TC002419.

Lustrino, M., Morra, V., Melluso, L., Brotzu, P., d'Amelio, F., Fedele, L., Franciosi, L., Lonis, R., and Petteruti Liebercknecht, A.M., 2004, The Cenozoic igneous activity of Sardinia: Periodico di Mineralogia, v. 73, p. 105–134.

Machado, N., and Simonetti, A., 2001, U-Pb dating and Hf isotopic composition of zircon by laser-ablation-MC-ICP-MS: Laser Ablation ICPMS in the Earth Sciences: Principles and Applications, Short Course, Mineralogical Association of Canada, v. 29, p. 121–146.

Maineri, C., Benvenuti, M., Costagliola, P., Dini, A., Lattanzi, P., Ruggieri, G., and Villa, I.M., 2003, Sericitic alteration at the La Crocetta deposit (Elba Island, Italy): interplay between magmatism, tectonics and hydrothermal activity: Mineralium Deposita, v. 38, no. 1, p. 67–86.

Maluski, H., 1977, Application de la méthode 40Ar/39Ar aux minéraux des roches cristallines perturbées par des événements thermiques et tectoniques en Corse.: Bulletin De La Societe Geologique De France, v. 19, p. 849–855.

Mantovani, E., Albarello, D., Tamburelli, C., Babbucci, D., and Viti, M., 1997, Plate convergence, crustal delamination, extrusion tectonics and minimization of shortening work as

main controlling factors of the recent Mediterranean deformation pattern: Annali di Geofisica, v. 40, p. 3.

Marinelli, P.G., 1967, Genèse des magmas du volcanisme Plio-Quaternaire des Apennins: Geologische Rundschau, v. 57, no. 1, p. 127–141.

Marroni, M., and Treves, B., 1998, Hidden terranes in the Northern Apennines, Italy: a record of late Cretaceous-Oligocene transpressional tectonics: The Journal of Geology, v. 106, no. 2, p. 149–162.

Massoli, D., Koyi, H.A., and Barchi, M.R., 2006, Structural evolution of a fold and thrust belt generated by multiple décollements: analogue models and natural examples from the Northern Apennines (Italy): Journal of Structural Geology, v. 28, p. 185 – 199, doi:10.1016/j.jsg.2005.11.002.

Matte, P., 1986, Tectonics and plate tectonics model for the Variscan belt of Europe: Tectonophysics, v. 126, no. 2–4, p. 329–374, doi:10.1016/0040-1951(86)90237-4.

Matte, P., 2001, The Variscan collage and orogeny (480-290 Ma) and the tectonic definition of the Armorica microplate: a review: Terra Nova, v. 13, no. 2, p. 122–128, doi:10.1046/j.1365-3121.2001.00327.x.

Mattioli, M., Di Battistini, G., and Zanzucchi, G., 2002, Petrology, geochemistry and age of the volcanic clasts from the Canetolo Unit (Northern Apennines, Italy): Bollettino della Società geologica Italiana, v. 121, no. 1, p. 399–416.

Mattioli, M., Lustrino, M., Ronca, S., and Bianchini, G., 2012, Alpine subduction imprint in Apennine volcaniclastic rocks. Geochemical–petrographic constraints and geodynamic implications from Early Oligocene Aveto-Petrignacola Formation (N Italy): Lithos, v. 134–135, p. 201–220, doi:10.1016/j.lithos.2011.12.017.

Mazzoli, S., and Helman, M., 1994, Neogene patterns of relative plate motion for Africa-Europe: some implications for recent central Mediterranean tectonics: Geologische Rundschau, v. 83, p. 464–468.

Meert, J.G., and Torsvik, T.H., 2003, The making and unmaking of a supercontinent: Rodinia revisited: Tectonophysics, v. 375, no. 1–4, p. 261–288, doi:10.1016/S0040-1951(03)00342-1.

Molli, G., 2008, Northern Apennine–Corsica orogenic system: an updated overview: Geological Society, London, Special Publications, v. 298, no. 1, p. 413–442, doi:10.1144/SP298.19.

Molli, G., Giorgetti, G., and Meccheri, M., 2000, Structural and petrological constraints on the tectono-metamorphic evolution of the Massa Unit (Alpi Apuane, NW Tuscany, Italy): Geological Journal, v. 35, no. 3–4, p. 251–264, doi:10.1002/gj.860.

Molli, G., Tribuzio, R., and Marquer, D., 2006, Deformation and metamorphism at the eastern border of the Tenda Massif (NE Corsica): a record of subduction and exhumation of continental crust: Journal of Structural Geology, v. 28, no. 10, p. 1748–1766, doi:10.1016/j.jsg.2006.06.018.

Morra, V., Secchi, F.A.G., Melluso, L., and Franciosi, L., 1997, High-Mg subduction-related Tertiary basalts in Sardinia, Italy: Lithos, v. 40, no. 1, p. 69–91, doi:10.1016/S0024-4937(96)00028-X.

Morton, A.C., 1991, Geochemical studies of detrital heavy minerals and their application to provenance research: Geological Society, London, Special Publications, v. 57, no. 1, p. 31–45.

Morton, A.C., Claoué-Long, J.C., and Berge, C., 1996, SHRIMP constraints on sediment provenance and transport history in the Mesozoic Statfjord Formation, North Sea: Journal of the Geological Society, v. 153, no. 6, p. 915–929, doi:10.1144/gsjgs.153.6.0915.

Muhongo, S., Kröner, A., and Nemchin, A.A., 2001, Single zircon evaporation and SHRIMP ages for granulite-facies rocks in the Mozambique belt of Tanzania: The Journal of Geology, v. 109, no. 2, p. 171–189.

Muhongo, S., and Lenoir, J.L., 1994, Pan-African granulite-facies metamorphism in the Mozambique Belt of Tanzania: U-Pb zircon geochronology: Journal of the Geological Society, v. 151, no. 2, p. 343–347, doi:10.1144/gsjgs.151.2.0343.

Musumeci, G., Mazzarini, F., Tiepolo, M., and Di Vincenzo, G., 2011, U-Pb and 40Ar/39Ar geochronology of Palaeozoic units in the northern Apennines: determining protolith age and alpine evolution using the Calamita Schist and Ortano Porphyroid: Geological Journal, v. 46, no. 4, p. 288–310.

Nesse, W.D., 2009, Introduction to mineralogy: Oxford University Press, 439 p.

Oggiano, G., Gaggero, L., Funedda, A., Buzzi, L., and Tiepolo, M., 2010, Multiple early Paleozoic volcanic events at the northern Gondwana margin: U–Pb age evidence from the Southern Variscan branch (Sardinia, Italy): Gondwana Research, v. 17, no. 1, p. 44–58, doi:10.1016/j.gr.2009.06.001.

Pandeli, E., and Puxeddu, M., 1990, Paleozoic age for the Tuscan upper metamorphic sequences of Elba and its implications for the geology of the Northern Apennines (Italy): Eclogae Geologicae Helvetiae, v. 83, no. 1, p. 123–142.

Pandeli, E., Santo, A.P., Morelli, M., and Orti, L., 2006, Petrological and geological data of porphyritic dikes from the Capo Arco area (Eastern Elba Island, northern Tyrrhenian Sea): Per. Mineral, v. 75, p. 241–254.

Parrish, R.R., and Noble, S.R., 2003, Zircon U-Th-Pb Geochronology by Isotope Dilution - Thermal Ionization Mass Spectrometry (ID-TIMS): Reviews in Mineralogy and Geochemistry, v. 53, no. 1, p. 183–213, doi:10.2113/0530183.

Pisarevsky, S.A., Wingate, M.T.D., Powell, C.M., Johnson, S., and Evans, D.A.D., 2003, Models of Rodinia assembly and fragmentation: Geological Society, London, Special Publications, v. 206, no. 1, p. 35–55, doi:10.1144/GSL.SP.2003.206.01.04.

Platt, J.P., 2007, From orogenic hinterlands to Mediterranean-style back-arc basins: a comparative analysis: Journal of the Geological Society, v. 164, no. 2, p. 297–311, doi:10.1144/âĂŃ0016-76492006-093.

Poli, G., 1992, Geochemistry of Tuscan Archipelago granitoids, Central Italy: The role of hybridization processes in their genesis: The Journal of Geology, v. 100, no. 1, p. 41–56.

Principi, G., and Treves, B., 1984, Il sistema Corso-Appenninico come prisma d'accrezione. Riflessi sul problema generale del limite Alpi-Appennini: Mem. Soc. Geol. It, v. 28, p. 549–576.

Puxeddu, M., Saupe, F., Dechomets, R., Gianelli, G., and Moine, B., 1984, Geochemistry and stratigraphic correlations - Application to the investigation of geothermal and mineral resources of Tuscany, Italy: Contribution to the knowledge of the ore deposits of Tuscany, II: Chemical Geology, v. 43, no. 1-2, p. 77–113, doi:10.1016/0009-2541(84)90141-4.

Quesada, C., 1990, Precambrian successions in SW Iberia: their relationship to "Cadomian" orogenic events: Geological Society, London, Special Publications, v. 51, no. 1, p. 353–362, doi:10.1144/GSL.SP.1990.051.01.23.

Quesada, C., 1991, Geological constraints on the Paleozoic tectonic evolution of tectonostratigraphic terranes in the Iberian Massif: Tectonophysics, v. 185, no. 3–4, p. 225–245, doi:10.1016/0040-1951(91)90446-Y.

Rau, A., and Tongiorgi, M., 1974, Geologia dei Monti Pisani a sud-est della Valle del Guappero: Memoire della Società Geologica Italiana, v. 12, p. 227–408.

Rocchi, S., Westerman, D.S., Dini, A., Innocenti, F., and Tonarini, S., 2002, Two-stage growth of laccoliths at Elba Island, Italy: Geology, v. 30, no. 11, p. 983–986.

Roeder, D., 1980, Geodynamics of the Alpine-Mediterranean system-a synthesis: Eclogae Geologicae Helvetiae, v. 73, no. 2, p. 353–377.

Rogers, J.J.W., and Santosh, M., 2002, Configuration of Columbia, a Mesoproterozoic Supercontinent: Gondwana Research, v. 5, no. 1, p. 5–22, doi:10.1016/S1342-937X(05)70883-2.

Rogers, J.J.W., Unrug, R., and Sultan, M., 1995, Tectonic assembly of Gondwana: Journal of Geodynamics, v. 19, no. 1, p. 1–34, doi:10.1016/0264-3707(94)00007-7.

Romeo, I., Lunar, R., Capote, R., Quesada, C., Dunning, G., Piña, R., and Ortega, L., 2006, U–Pb age constraints on Variscan magmatism and Ni-Cu-PGE metallogeny in the Ossa-Morena Zone (SW Iberia): Journal of the Geological Society, v. 163, no. 5, p. 837–846, doi:10.1144/0016-76492005-065.

Rosenbaum, G., and Lister, G.S., 2004, Neogene and Quaternary rollback evolution of the Tyrrhenian Sea, the Apennines, and the Sicilian Maghrebides: Tectonics, v. 23, p. TC1013.

Rosenbaum, G., Lister, G.S., and Duboz, C., 2002, Relative motions of Africa, Iberia and Europe during Alpine orogeny: Tectonophysics, v. 359, p. 117–129.

Rossi, P., Oggiano, G., and Cocherie, A., 2009, A restored section of the "southern Variscan realm" across the Corsica-Sardinia microcontinent: Comptes Rendus Geoscience, v. 341, no. 2–3, p. 224–238, doi:10.1016/j.crte.2008.12.005.

Sánchez-García, T., Bellido, F., and Quesada, C., 2003, Geodynamic setting and geochemical signatures of Cambrian-Ordovician rift-related igneous rocks (Ossa-Morena Zone, SW Iberia): Tectonophysics, v. 365, no. 1–4, p. 233–255, doi:10.1016/S0040-1951(03)00024-6.

Santosh, M., 2010, Assembling North China Craton within the Columbia supercontinent: The role of double-sided subduction: Precambrian Research, v. 178, no. 1–4, p. 149–167, doi:10.1016/j.precamres.2010.02.003.

Şengör, A.M.C., Yılmaz, Y., and Sungurlu, O., 1984, Tectonics of the Mediterranean Cimmerides: nature and evolution of the western termination of Palaeo-Tethys: Geological Society, London, Special Publications, v. 17, p. 77–112.

Seranne, M., Bruguier, O., and Moussavou, M., 2008, U-Pb single zircon grain dating of present fluvial and Cenozoic aeolian sediments from Gabon: consequences on sediment provenance, reworking, and erosion processes on the equatorial West African margins: Bulletin de la Societe Geologique de France, v. 179, no. 1, p. 29–40, doi:10.2113/gssgfbull.179.1.29.

Serri, G., Innocenti, F., and Manetti, P., 1993, Geochemical and petrological evidence of the subduction of delaminated Adriatic continental lithosphere in the genesis of the Neogene-Quaternary magmatism of central Italy: Tectonophysics, v. 223, no. 1, p. 117–147.

Sláma, J., Košler, J., Condon, D.J., Crowley, J.L., Gerdes, A., Hanchar, J.M., Horstwood, M.S.A., Morris, G.A., Nasdala, L., Norberg, N., Schaltegger, U., Schoene, B., Tubrett, M.N., and Whitehouse, M.J., 2008, Plešovice zircon - A new natural reference material for U–Pb and Hf isotopic microanalysis: Chemical Geology, v. 249, no. 1, p. 1–35.

Speranza, F., Villa, I.M., Sagnotti, L., Florindo, F., Cosentino, D., Cipollari, P., and Mattei, M., 2002, Age of the Corsica–Sardinia rotation and Liguro–Provençal Basin spreading: new paleomagnetic and Ar/Ar evidence: Tectonophysics, v. 347, no. 4, p. 231–251.

Stampfli, G.M., 2000, Tethyan oceans: Geological society, London, special publications, v. 173, p. 1–23.

Stampfli, G.M., and Borel, G.D., 2002, A plate tectonic model for the Paleozoic and Mesozoic constrained by dynamic plate boundaries and restored synthetic oceanic isochrons: Earth and Planetary Science Letters, v. 196, no. 1–2, p. 17–33, doi:10.1016/S0012-821X(01)00588-X.

Stampfli, G.M., Borel, G.D., Cavazza, W., Mosar, J., and Ziegler, P.A., 2001, Palaeotectonic and palaeogeographic evolution of the western Tethys and PeriTethyan domain (IGCP Project 369): Episodes, v. 24, no. 4, p. 222–228.

Stampfli, G.M., Borel, G.D., Marchant, R., and Mosar, J., 2002a, Western Alps geological constraints on western Tethyan reconstructions: Journal of the Virtual Explorer, v. 8, p. 77–106.

Stampfli, G.M., and Hochard, C., 2009, Plate tectonics of the Alpine realm: Geological Society, London, Special Publications, v. 327, p. 89–111.

Stampfli, G.M., Hochard, C., and Von Raumer, J.F., 2006, Reconstructing the Palaeozoic Gondwana margin and its redistribution – new aspects, *in* Geophysical Research Abstracts, v. 8: .

Stampfli, G.M., von Raumer, J.F., and Borel, G.D., 2002b, Paleozoic evolution of pre-Variscan terranes: from Gondwana to the Variscan collision: Geological Society of America - Special papers, v. 364, p. 263–280.

Stöcklin, J., 1974, Possible ancient continental margins in Iran: The geology of continental margins, p. 873–887.

Sylvester, P.J., 2008, LA-(MC)-ICP-MS trends in 2006 and 2007 with particular emphasis on measurement uncertainties: Geostandards and Geoanalytical Research, v. 32, no. 4, p. 469–488, doi:10.1111/j.1751-908X.2008.00924.x.

Tavarnelli, E., 1997, Structural evolution of a foreland fold-and-thrust belt: the Umbria-Marche Apennines, Italy: Journal of Structural Geology, v. 19, no. 3–4, p. 523 – 534, doi:10.1016/S0191-8141(96)00093-4.

Termier, P., 1909, Sur les nappes de l'Ile d'Elbe: C.R. Acad. Sci. Paris, v. 148.

Tommasini, S., Poli, G., and Halliday, A.N., 1995, The role of sediment subduction and crustal growth in Hercynian plutonism: isotopic and trace element evidence from the Sardinia-Corsica Batholith: Journal of Petrology, v. 36, no. 5, p. 1305–1332, doi:10.1093/petrology/36.5.1305.

Toteu, S.F., Van Schmus, W.R., Penaye, J., and Michard, A., 2001, New U–Pb and Sm–Nd data from north-central Cameroon and its bearing on the pre-Pan African history of central Africa: Precambrian Research, v. 108, no. 1–2, p. 45–73, doi:10.1016/S0301-9268(00)00149-2.

Treves, B.E., 1984, Orogenic belts as accretionary prisms: the example of the Northern Apennines: Ofioliti, v. 9, no. 3, p. 577–618.

Trevisan, L., 1950, L'elba orientale e la sua tettonica di scivolamento per gravità: Società Cooperativa Tipografica.

Turco, E., Macchiavelli, C., Mazzoli, S., Schettino, A., and Pierantoni, P.P., 2012, Kinematic evolution of Alpine Corsica in the framework of Mediterranean mountain belts: Tectonophysics, v. 579, p. 193–206, doi:10.1016/j.tecto.2012.05.010.

Vai, G.B., 1978, Tentative correlation of Palaeozoic rocks, Italian peninsula and islands: Österr. Akad. Wissen. Schrifte. Erdwiss. Komm, v. 3, p. 313–329.

Valle Aguado, B., Azevedo, M.R., Schaltegger, U., Martínez Catalán, J.R., and Nolan, J., 2005, U–Pb zircon and monazite geochronology of Variscan magmatism related to syn-convergence extension in Central Northern Portugal: Lithos, v. 82, no. 1–2, p. 169–184, doi:10.1016/j.lithos.2004.12.012.

Valverde-Vaquero, P., and Dunning, G.R., 2000, New U–Pb ages for Early Ordovician magmatism in Central Spain: Journal of the Geological Society, v. 157, no. 1, p. 15–26, doi:10.1144/jgs.157.1.15.

Van Bemmelen, R.W., 1972, Driving forces of Mediterranean orogeny (Tyrrhenian test-case): Geol. Mijnbouw, v. 51, no. 5, p. 548–573.

Vermeesch, P., 2004, How many grains are needed for a provenance study?: Earth and Planetary Science Letters, v. 224, no. 3, p. 441–451, doi:10.1016/j.epsl.2004.05.037.

Villaseca, C., Downes, H., Pin, C., and Barbero, L., 1999, Nature and composition of the lower continental crust in Central Spain and the granulite–granite linkage: inferences from granulitic xenoliths: Journal of Petrology, v. 40, no. 10, p. 1465–1496, doi:10.1093/petroj/40.10.1465.

von Raumer, J.F., Stampfli, G., Borel, G., and Bussy, F., 2002, Organization of pre-Variscan basement areas at the North-Gondwanan margin: International Journal of Earth Sciences, v. 91, p. 35–52.

von Raumer, J.F., Stampfli, G.M., and Bussy, F., 2003, Gondwana-derived microcontinents – the constituents of the Variscan and Alpine collisional orogens: Tectonophysics, v. 365, no. 1–4, p. 7–22, doi:10.1016/S0040-1951(03)00015-5.

Westerman, D.S., Dini, A., Innocenti, F., and Rocchi, S., 2003, When and where did hybridization occur? The case of the Monte Capanne Pluton, Italy: Atlantic Geology, v. 39, p. 147–162.

Westerman, D.S., Dini, A., Innocenti, F., and Rocchi, S., 2004, Rise and fall of a nested Christmas-tree laccolith complex, Elba Island, Italy: Geological Society, London, Special Publications, v. 234, p. 195–213.

Whitehouse, M.J., Bridgwater, D., and Park, R.G., 1997, Detrital zircon ages from the Loch Maree Group, Lewisian Complex, NW Scotland: confirmation of a Palaeoproterozoic Laurentia-Fennoscandia connection: Terra Nova, v. 9, no. 5-6, p. 260–263, doi:10.1111/j.1365-3121.1997.tb00025.x.

Wolf, R., 2005, What is ICP-MS? ...and more importantly, what can it do?: URL `http://crustal.usgs.gov/laboratories/icpms/intro.html`, Accessed 19.02.2013.

Wortmann, U.G., Weissert, H., Funk, H., and Hauck, J., 2001, Alpine plate kinematics revisited: the Adria problem: Tectonics, v. 20, no. 1, p. 134–147.

Zeck, H.P., 1996, Betic-Rif orogeny: subduction of Mesozoic Tethys lithosphere under eastward drifting Iberia, slab detachment shortly before 22 Ma, and subsequent uplift and extensional tectonics: Tectonophysics, v. 254, no. 1-2, p. 1–16, doi:10.1016/0040-1951(95)00206-5.

Zhao, G., Cawood, P.A., Wilde, S.A., and Sun, M., 2002, Review of global 2.1–1.8 Ga orogens: implications for a pre-Rodinia supercontinent: Earth-Science Reviews, v. 59, no. 1–4, p. 125–162, doi:10.1016/S0012-8252(02)00073-9.

Zhao, G., Sun, M., Wilde, S.A., and Li, S., 2003, Assembly, Accretion and Breakup of the Paleo-Mesoproterozoic Columbia Supercontinent: Records in the North China Craton: Gondwana Research, v. 6, no. 3, p. 417–434, doi:10.1016/S1342-937X(05)70996-5.

Zhao, G., Sun, M., Wilde, S.A., and Li, S., 2004, A Paleo-Mesoproterozoic supercontinent: assembly, growth and breakup: Earth-Science Reviews, v. 67, no. 1–2, p. 91–123, doi:10.1016/j.earscirev.2004.02.003.

11 Appendix

Appendix 1 - Sample localities

Appendix 2 - LA-ICPMS Tune parameters

Appendix 3 - LA-ICPMS results

Appendix 1 - Sample localities

Sample	GPS coordinate	Elevation (MASL)	Lithology	Locality description	Outcrop description	Foliation	Joints
EAK-01	32T 0616902 UTM 4738349		Blackish quartzites and phyllites	Roadcut SW of Isolotto d'Ortano	Fine-grained, dark-grey quartzite. Foliated/bedded on cm-dm scale. Some quartz veins parallel and across foliation. Lighter-colored quartzites are observed towards both ends of the outcrop.	271/49 275/48 280/14	033/60 036/60 039/88 019/68 019/53 060/65 032/74 035/76 081/71 046/55
EHS-01	32T 0616253 UTM 4730584	213	Mt. Calamita Schist	Outcrop along tennis-field. Approximately 80x2 m.	Consists of quartzitic layers and more mica-rich layers. the light-grey, quartzitic layers contains quartz seggregations on cm-dm-scale. The dark grey micaschist is fine-grained and contains biotite, quartz and feldspar. Fractured and intensively folded.	322/55 328/70 307/61 282/65 306/82 299/70	214/79 037/85 047/80 019/86 219/84
EHS-02	32T 0616977 UTM 4731947	108	Mt. Calamita Schist	Roadcut on E-side of Mt. Calamita Promontory.	Well exposed outcrop with some vegetation. Thin quartzitic veins (cm-scale) are observed within the micaschist.		
EHS-03	32T 0614251	162	Mt. Calamita Schist	Roadcut on SW-side	Dark grey, fine-grained and quartz-rich	282/30	095/83

	UTM 4730877			of Mt. Calamita Promontory.	sample. Quartz seggregations are observed, but in smaller amount than for EHS-01 and EHS-02. Quartz veins (mm-scale) observed. Larger quartz veins towards SW. Also more mica and more foliated towards SW.	231/20 278/70 256/52	103/88 279/86 095/87
EHS-04	32T 0612544 UTM 4731645	2	Amphibolite lens in Mt. Calamita Schist	Coastal outcrop. 4x2 m.	Sample outcrop is altered and edgy. Outcrop is amphibolite surrounded by Mt. Calamita Schist. Micaschist surrounding the amphibolite is consists of interlayering of mica, quartz and feldspar. Cm-dm thick tourmaline veins follows and cross-cuts bedding.	292/56 280/59 292/51 276/61 279/54	
EHS-05	32T 0616219 UTM 4742620	204	Verruca Formation	Upper parts of the Rio Marina Mines	Well exposed outcrop above Rio Marina Mines. 20X10 m. More phyllitic than EJ-49. Light purple, grey, green and white sample. Hematite can be observed. The rock is more quartzitic at higher levels.	252/27 255/30	
EHS-06	32T 0617267 UTM 4745421	2	Rio Marina Formation	Beach outcrop Le Fornacelle	Well exposed with vegetation. Silty at W-side and more phyllitic at E-side. Light-grey in colour. Quartz veins are observed. Open folding also observed towards E.	266/61 252/52 002/40 347/45 001/31	145/60 163/60 170/64 143/57
EHS-07	32T 0617039 UTM 4738538	3	Quartzitic lens in Capo d'Arco Schist	Coastal outcrop between Ortano Beach and Isolotto d'Ortano	Sample for thin-section. Sample is from a finer quartzitic layer within the Capo d'Arco Schist.		

EHS-08	32T 0616993 UTM 4738663	2	Capo d'Arco Schist	Coastal outcrop between Ortano Beach and Isolotto d'Ortano	Strongly weathered surface. Main constituents of this rock are biotite, quartz and feldspar. Quartz and contact metamorphic minerals observed in the foliation plane. Foliation is cross-cut by veins of quartz and feldspar.	291/49 294/44 293/56	210/87 205/82
EHS-09	32T 0617494 UTM 4743719	5	Verruca Formation	Cliff at Topinetti Beach	Sand-sized grains can occur with various degree of mica. Grey to green/blue in colour in sandy parts. Consists of quartz, feldspar and mica. Sample is from the more sandy parts of the outcrop. Can also appear as purple and phyllitic at this outcrop, but that was not sampled. C-S fabric also observed.	057/32 072/43 066/33 073/44 049/30	
EHS-10	32T 0615865 UTM 4739541	32	Rio Marina Formation	Roadcut in Ortano Valley	Partly well exposed with areas covered by vegetation. Rock is fine-grained and well foliated on mm-scale. Some parts have less prominent foliation. A lot of folding and veins are observed. Outcrop appears more silty towards E and more phyllitic towards E. The silty part is dark grey with quartz veins. Purple in fractures. Phyllitic part is lighter. Probably muscovite in both parts.	252/34 251/54 263/59 256/44 262/37 252/55 258/50 249/48 257/52 264/58	
EHS-11	32T 0616257 UTM 4739320	5	Phyllites and metasiltstones	Roadcut in Ortano Valley	Medium-poorly exposed outcrop with a lot of vegetation. Well foliated towards NW	238/36 241/32	

					(mm-scale) and more massive and less foliated towards SE (cm-scale). Light-medium grey rock. Veins of quartz and feldspar observed.	241/52 243/31 261/26 259/29 268/30 249/25 265/24 254/27 247/23 272/22	
EHS-12	32T 0617163 UTM 4738281	2	Light Capo d'Arco Schist	Coastal outcrop south of Isolotto d'Ortano	Well exposed part of extending outcrop along beach. Light variety of Capo d'Arco Schist. Graphite, contact-metamorphic minerals and a lot of mica. Less quartz seggregation than dark variety of Capo d'Arco Schist.	297/21 316/22 331/24 336/24 290/29	
EHS-13	32T 0617128 UTM 4738245	6	Capo d'Arco Schist	Coastal outcrop south of Isolotto d'Ortano	Well exposed outcrop in the ground. Some vegatation around the outcrop. Less evident foliation than EHS-12, but foliation is still observed. Quartz- and feldspar-rich Capo d'Arco Schist with less mica than EHS-12. Contact-metamorphic minerals observed. Two joint-sets observed.	007/07 057/05	265/87 259/86 266/76 081/72 079/81 072/62 081/75 076/81
EHS-14	32T 0617158 UTM 4738348	5	Pyroxene-rich seggregation in Capo d'Arco Schist	Coastal outcrop south of Isolotto d'Ortano	Pyroxene-rich veins in Capo d'Arco Schist. Sample is for thin-section.		

EHS-15	32T 0617443 UTM 4739411	4	Dark Capo d'Arco Schist	Coastal outcrop NE of Ex. Vedetta	Well exposed coastal outcrop consisting of intermediate-dark Capo d'Arco Schist. Quartz seggregations on mainly mm-cm-scale, but dm-scale is also observed. Isoclinally folded quartz seggregations. Large pegmatites observed with pinch-and-swell structures. Andalusite±cordierite oberved. Outcrop is less weathered than the outcrops south of Isolotto d'Ortano. Less quartz seggregations towards S of the outcrop.	266/32 277/31 289/31 293/39 279/34
EJ-49	32T 0615659 UTM 4736837		Verruca Formation	Roadcut close to contact to Rio Marina Formation	Quite dark. Located below very bright quartzitic layers.	
EJ-50	32T 0616394 UTM 4737507		Phyllites and metasiltstones	100 m SW from entrance of gate to Capo d'Arco Residence	A mixture of quartiztes and phyllites	

Appendix 2 - LA-ICPMS Tune parameters

Parameter	Session						Unit
	130215JJ_zir_a	130215JJ_zir_b	130218JJ_zir_a	130218JJ_zir_b	130320JJ_zir_a	130320JJ_zir_b	
Resolution	Low	Low	Low	Low	Low	Low	
Focus offset	30.00	30.00	30.00	30.00	30.00	30.00	%
UaUb	0.170	0.170	0.170	0.170	0.170	0.170	%
Cool gas	15.95	15.95	15.95	15.95	15.95	15.95	L/min
Aux gas	0.69	0.69	0.65	0.65	0.69	0.69	L/min
Sample gas	1.115	1.115	1.030	1.015	0.800	0.795	L/min
Additional 1	0.000	0.000	0.000	0.000	0.000	0.000	L/min
Plasma power	1300	1300	1300	1300	1300	1300	Watt
Extraction	-2000.0	-2000.0	-2000.0	-2000.0	-2000	-2000	V
Focus	-970.0	-965.0	-940.0	-1010.0	-975.00	-975.00	V
X-Deflection	-0.20	-0.20	-0.30	-0.30	-0.50	-0.50	V
Y-Deflection	2.00	2.00	2.50	2.50	3.90	3.90	V
Shape	117.00	117.00	117.00	117.00	117.00	117.00	V
Rotation quadropol 1	0.00	0.00	0.00	0.00	0.00	0.00	V
Rotation quadropol 2	0.00	0.00	0.00	0.00	0.00	0.00	V
Focus quadropol 1	0.00	0.00	0.00	0.00	0.00	0.00	V
Focus quadropol 2	0.00	0.00	0.00	0.00	0.00	0.00	V
MATSUDA-Plate	58.09	58.09	58.09	58.09	58.09	58.09	V
SEM-Deflection	-48.00	-48.00	-48.00	-48.00	-48.00	-48.00	V
SEM	1920.0	1920.0	1920.0	1920.0	2175.0	2175.0	V
Guard Electrode	Yes	Yes	Yes	Yes	Yes	Yes	
Additional 2	0.000	0.000	0.000	0.000	0.000	0.000	L/min
Torch X-Pos.	2.000	2.000	2.000	2.200	2.100	2.100	mm
Torch Y-Pos.	0.800	0.800	0.800	1.000	1.200	1.200	mm
Torch Z-Pos.	-4.800	-4.800	-4.800	-4.800	-4.800	-4.800	mm
Peri. Pump Speed	5.00	5.00	5.00	5.00	5.00	5.00	rpm

Appendix 3 - LA-ICPMS results

	ISOTOPIC RATIOS							CALCULATED AGES (Ma)							Prob. of
ID	$^{207}Pb/^{235}U$	$\pm1\sigma$	$^{206}Pb/^{238}U$	$\pm1\sigma$	Rho	$^{207}Pb/^{206}Pb$	$\pm1\sigma$	$^{206}Pb/^{238}U$	$\pm1\sigma$	$^{207}Pb/^{206}Pb$	$\pm1\sigma$	Conc. age	$\pm2\sigma$	Conc.	conc.
Sample EHS-15 - Biotite-rich micaschist (Capo d'Arco Schist)															
EHS-15-01	0.5320	0.0289	0.0692	0.0017	0.2233	0.0564	0.0014	432	10	470	53	432	19	91.8	0.9334
EHS-15-02	0.5418	0.0308	0.0696	0.0022	0.2839	0.0561	0.0014	434	14	457	54	435	25	95.0	0.7790
EHS-15-03	0.5934	0.0377	0.0788	0.0025	0.2478	0.0568	0.0013	489	15	483	52	486	28	101.2	0.5153
EHS-15-04	0.5778	0.0296	0.0729	0.0025	0.3368	0.0561	0.0012	454	16	455	49	457	27	99.8	0.6428
EHS-15-05	0.5271	0.0266	0.0686	0.0013	0.1820	0.0560	0.0012	428	8	453	49	428	15	94.4	0.8933
EHS-15-06	0.5322	0.0255	0.0695	0.0011	0.1654	0.0563	0.0012	433	7	466	47	433	13	93.0	0.9994
EHS-15-07	0.5253	0.0310	0.0692	0.0019	0.2275	0.0561	0.0014	432	12	454	55	431	21	95.0	0.8903
EHS-15-08	0.5411	0.0254	0.0707	0.0013	0.1947	0.0554	0.0012	440	8	427	49	440	15	103.1	0.9393
EHS-15-09	0.5367	0.0271	0.0691	0.0011	0.1564	0.0567	0.0014	431	7	478	53	431	13	90.1	0.7603
EHS-15-10	0.4993	0.0278	0.0646	0.0034	0.4719	0.0541	0.0013	403	21	377	56	408	34	107.0	0.6972
EHS-15-11	0.4873	0.0266	0.0659	0.0017	0.2363	0.0559	0.0012	411	11	446	48	410	19	92.1	0.6557
EHS-15-12	0.4852	0.0447	0.0668	0.0032	0.2577	0.0557	0.0015	417	20	440	60	413	36	94.7	0.6331
EHS-15-13	0.5271	0.0265	0.0684	0.0013	0.1902	0.0560	0.0013	427	8	452	53	427	15	94.4	0.8521
EHS-15-14	0.5141	0.0295	0.0673	0.0023	0.2927	0.0549	0.0013	420	14	410	52	420	25	102.3	0.9420
EHS-15-15	0.5083	0.0279	0.0657	0.0022	0.3017	0.0550	0.0013	410	14	411	54	412	24	100.0	0.7273
EHS-15-16	0.4877	0.0284	0.0692	0.0015	0.1830	0.0546	0.0012	432	9	396	48	428	17	109.0	0.1493
EHS-15-17	0.5282	0.0330	0.0702	0.0024	0.2698	0.0567	0.0012	438	15	480	48	436	26	91.2	0.7604
EHS-15-18	0.5587	0.0418	0.0732	0.0031	0.2836	0.0568	0.0015	455	19	483	58	454	34	94.2	0.8683
EHS-15-19	0.5365	0.0259	0.0696	0.0015	0.2258	0.0559	0.0012	434	9	450	49	434	17	96.3	0.8917
EHS-15-20	0.5022	0.0249	0.0660	0.0016	0.2477	0.0554	0.0012	412	10	427	50	412	19	96.6	0.9403
EHS-15-21	0.5316	0.0251	0.0688	0.0011	0.1739	0.0554	0.0012	429	7	427	48	430	13	100.5	0.8292
EHS-15-22	0.5393	0.0295	0.0690	0.0022	0.2949	0.0551	0.0013	430	14	416	52	432	25	103.3	0.7043
EHS-15-23	0.5079	0.0286	0.0666	0.0024	0.3250	0.0551	0.0012	416	15	415	50	416	27	100.3	0.9518
EHS-15-24	0.5426	0.0280	0.0678	0.0017	0.2487	0.0562	0.0013	423	11	460	53	426	20	91.9	0.3567
EHS-15-25	0.5277	0.0327	0.0693	0.0022	0.2580	0.0566	0.0013	432	14	478	52	431	25	90.4	0.9463

	ISOTOPIC RATIOS							CALCULATED AGES (Ma)							Prob. of
ID	$^{207}Pb/^{235}U$	$\pm1\sigma$	$^{206}Pb/^{238}U$	$\pm1\sigma$	Rho	$^{207}Pb/^{206}Pb$	$\pm1\sigma$	$^{206}Pb/^{238}U$	$\pm1\sigma$	$^{207}Pb/^{206}Pb$	$\pm1\sigma$	Conc. age	$\pm2\sigma$	Conc.	conc.
Sample EHS-15 - Biotite-rich micaschist (Capo d'Arco Schist)															
EHS-15-26	0.4949	0.0275	0.0680	0.0015	0.1954	0.0553	0.0012	424	9	423	49	422	17	100.3	0.3954
EHS-15-27	0.5276	0.0266	0.0676	0.0022	0.3244	0.0549	0.0009	422	14	406	35	424	24	103.8	0.6423
EHS-15-28	0.9585	0.0573	0.1081	0.0054	0.4167	0.0622	0.0009	662	33	683	30	673	52	96.9	0.5290
EHS-15-29	0.5510	0.0346	0.0684	0.0037	0.4310	0.0562	0.0009	427	23	461	35	436	38	92.6	0.4310
EHS-15-30	0.5480	0.0301	0.0734	0.0020	0.2456	0.0561	0.0009	457	12	457	36	454	22	99.9	0.5281
EHS-15-31	0.5499	0.0315	0.0694	0.0019	0.2349	0.0563	0.0010	432	12	464	38	434	21	93.1	0.5526
EHS-15-32	0.5787	0.0252	0.0691	0.0023	0.3810	0.0553	0.0009	431	14	423	37	442	25	101.9	0.0513
EHS-15-33	0.5717	0.0299	0.0699	0.0029	0.3909	0.0562	0.0009	435	18	458	34	445	30	95.0	0.2433
EHS-15-34	0.5418	0.0288	0.0734	0.0017	0.2198	0.0561	0.0009	456	11	456	35	454	20	100.1	0.3868
EHS-15-35	0.5470	0.0262	0.0689	0.0021	0.3171	0.0562	0.0010	429	13	460	40	433	23	93.4	0.4450
EHS-15-36	0.8520	0.0438	0.1010	0.0037	0.3585	0.0627	0.0010	620	23	697	34	623	38	89.1	0.8395
EHS-15-37	0.5734	0.0221	0.0719	0.0026	0.4753	0.0563	0.0010	447	16	465	38	455	26	96.3	0.4070
EHS-15-38	0.6417	0.0286	0.0793	0.0033	0.4706	0.0576	0.0011	492	21	513	40	499	32	95.8	0.5477
EHS-15-39	0.7265	0.0736	0.0904	0.0061	0.3353	0.0626	0.0011	558	38	696	36	557	64	80.2	0.9418
EHS-15-40	0.8046	0.0346	0.0955	0.0032	0.3850	0.0596	0.0013	588	19	591	46	593	32	99.5	0.5815
EHS-15-41	0.5395	0.0235	0.0677	0.0024	0.4129	0.0578	0.0010	422	15	521	39	429	25	81.0	0.3346
EHS-15-42	0.5556	0.0299	0.0695	0.0035	0.4640	0.0560	0.0011	433	22	454	43	442	35	95.4	0.4610
EHS-15-43	0.6208	0.1032	0.0779	0.0091	0.3500	0.0611	0.0010	484	56	644	36	486	96	75.1	0.9207
EHS-15-44	0.5873	0.0178	0.0752	0.0020	0.4306	0.0563	0.0009	468	12	463	36	468	20	101.1	0.9004
EHS-15-45	0.5304	0.0403	0.0694	0.0045	0.4280	0.0565	0.0010	432	28	474	39	432	46	91.3	0.9924
EHS-15-46	0.5671	0.0217	0.0697	0.0020	0.3753	0.0569	0.0010	434	12	488	40	442	22	88.9	0.1362
EHS-15-47	0.5258	0.0197	0.0699	0.0022	0.4132	0.0550	0.0009	436	13	412	36	432	22	105.6	0.6372
EHS-15-48	0.8198	0.0428	0.0960	0.0045	0.4512	0.0610	0.0011	591	28	639	38	601	43	92.5	0.5211
EHS-15-49	0.5482	0.0195	0.0708	0.0025	0.4867	0.0561	0.0009	441	15	457	34	443	23	96.5	0.8455
EHS-15-50	0.6894	0.0284	0.0870	0.0026	0.3581	0.0591	0.0009	538	16	572	34	536	26	94.0	0.7681
EHS-15-51	0.6665	0.0253	0.0837	0.0023	0.3666	0.0583	0.0010	518	14	541	39	518	24	95.8	0.9816
EHS-15-52	1.7886	0.0848	0.1749	0.0055	0.3324	0.0756	0.0014	1039	33	1084	38	1040	50	95.9	0.9519
EHS-15-53	0.5343	0.0249	0.0678	0.0025	0.3978	0.0566	0.0011	423	16	476	43	428	26	88.9	0.4922
EHS-15-54	0.4917	0.0588	0.0681	0.0043	0.2655	0.0568	0.0015	425	27	485	56	420	48	87.5	0.6532

	ISOTOPIC RATIOS							CALCULATED AGES (Ma)							Prob. of
ID	$^{207}Pb/^{235}U$	$\pm1\sigma$	$^{206}Pb/^{238}U$	$\pm1\sigma$	Rho	$^{207}Pb/^{206}Pb$	$\pm1\sigma$	$^{206}Pb/^{238}U$	$\pm1\sigma$	$^{207}Pb/^{206}Pb$	$\pm1\sigma$	Conc. age	$\pm2\sigma$	Conc.	conc.
Sample EHS-12 - Quartzitic phyllite (Capo d'Arco Schist)															
EHS-12-01	0.5291	0.0298	0.0692	0.0030	0.3828	0.0558	0.0010	431	19	445	41	431.2	31.2	96.9	0.9955
EHS-12-02	0.5503	0.0233	0.0684	0.0024	0.4185	0.0560	0.0009	426	15	451	37	434.9	25.2	94.5	0.2422
EHS-12-03	0.5354	0.0246	0.0687	0.0026	0.4061	0.0559	0.0010	428	16	447	41	431.5	26.6	95.8	0.6781
EHS-12-04	0.5138	0.0249	0.0645	0.0030	0.4823	0.0558	0.0009	403	19	444	35	413.4	30.1	90.9	0.3144
EHS-12-05	0.5856	0.0223	0.0704	0.0033	0.6250	0.0560	0.0011	438	21	453	42	465.1	28.4	96.8	0.0602
EHS-12-06	0.5253	0.0201	0.0692	0.0020	0.3696	0.0556	0.0009	431	12	435	37	430.3	20.6	99.2	0.8530
EHS-12-07	0.5327	0.0238	0.0694	0.0024	0.3835	0.0566	0.0009	432	15	477	33	432.9	24.9	90.6	0.9437
EHS-12-08	0.5165	0.0184	0.0663	0.0018	0.3763	0.0558	0.0009	414	11	444	35	417.4	19.0	93.2	0.4979
EHS-12-09	0.5199	0.0236	0.0695	0.0021	0.3308	0.0555	0.0009	433	13	433	35	430.4	22.6	100.0	0.6281
EHS-12-10	0.5161	0.0243	0.0676	0.0023	0.3688	0.0554	0.0009	422	15	428	37	422.1	24.9	98.6	0.9654
EHS-12-11	0.5610	0.0221	0.0688	0.0024	0.4389	0.0566	0.0009	429	15	476	36	440.1	24.5	90.1	0.1227
EHS-12-12	0.4913	0.0364	0.0664	0.0046	0.4659	0.0542	0.0011	414	29	379	46	409.1	44.6	109.2	0.7560
EHS-12-13	0.5164	0.0197	0.0682	0.0021	0.3955	0.0564	0.0008	425	13	468	32	424.2	21.4	91.0	0.8537
EHS-12-14	0.5792	0.0225	0.0701	0.0037	0.6779	0.0559	0.0014	437	23	446	55	464.8	28.9	97.9	0.0987
EHS-12-15	0.5115	0.0226	0.0669	0.0023	0.3929	0.0556	0.0009	418	15	438	37	418.5	24.3	95.4	0.9147
EHS-12-16	0.5032	0.0256	0.0654	0.0027	0.4014	0.0554	0.0013	409	17	429	51	410.9	28.0	95.2	0.7755
EHS-12-17	0.5314	0.0163	0.0660	0.0018	0.4567	0.0556	0.0009	412	12	437	36	422.7	18.8	94.2	0.0684
EHS-12-18	0.5611	0.0366	0.0704	0.0043	0.4650	0.0567	0.0010	439	27	481	39	446.3	42.4	91.1	0.5945
EHS-12-19	0.5614	0.0197	0.0721	0.0020	0.4034	0.0561	0.0009	449	13	458	36	450.4	21.0	98.0	0.7760
EHS-12-20	0.5434	0.0266	0.0668	0.0035	0.5296	0.0553	0.0012	417	22	426	49	433.1	33.1	97.9	0.2131
EHS-12-21	0.5440	0.0250	0.0725	0.0027	0.3994	0.0555	0.0009	451	17	433	36	446.4	27.1	104.2	0.5632
EHS-12-22	0.5456	0.0394	0.0694	0.0047	0.4706	0.0557	0.0010	432	29	442	38	438.0	46.4	97.8	0.7247
EHS-12-23	0.5355	0.0200	0.0679	0.0022	0.4320	0.0563	0.0009	423	14	465	36	429.3	22.4	91.1	0.3878
EHS-12-24	0.5314	0.0300	0.0677	0.0029	0.3802	0.0560	0.0012	422	18	454	46	426.3	30.9	93.1	0.6132
EHS-12-25	0.5197	0.0178	0.0678	0.0019	0.4207	0.0554	0.0009	423	12	430	35	423.8	19.9	98.2	0.8593
EHS-12-26	0.5066	0.0253	0.0658	0.0026	0.3962	0.0555	0.0010	411	16	430	41	413.3	27.4	95.5	0.7790
EHS-12-27	0.4877	0.0262	0.0635	0.0029	0.4252	0.0553	0.0011	397	18	423	44	400.1	30.0	93.9	0.7390
EHS-12-28	0.5352	0.0417	0.0700	0.0045	0.4138	0.0551	0.0010	436	28	416	41	435.6	46.0	104.7	0.9807

	ISOTOPIC RATIOS							CALCULATED AGES (Ma)							Prob. of
ID	$^{207}Pb/^{235}U$	$\pm1\sigma$	$^{206}Pb/^{238}U$	$\pm1\sigma$	Rho	$^{207}Pb/^{206}Pb$	$\pm1\sigma$	$^{206}Pb/^{238}U$	$\pm1\sigma$	$^{207}Pb/^{206}Pb$	$\pm1\sigma$	Conc. age	$\pm2\sigma$	Conc.	conc.
Sample EAK-01 - Blackish quartzites and phyllites															
EAK-01-01	0.9446	0.0359	0.1082	0.0034	0.4197	0.0630	0.0008	663	21	708	27	670	33	93.5	0.5429
EAK-01-02	0.8484	0.0340	0.0987	0.0047	0.5928	0.0605	0.0013	607	29	623	47	622	37	97.4	0.4379
EAK-01-03	0.5766	0.0229	0.0735	0.0025	0.4347	0.0566	0.0008	457	16	477	31	460	25	95.9	0.7433
EAK-01-04	1.6287	0.0593	0.1615	0.0080	0.6825	0.0728	0.0015	965	48	1008	42	984	45	95.8	0.6286
EAK-01-05	0.5481	0.0289	0.0711	0.0027	0.3642	0.0568	0.0010	443	17	485	38	443	29	91.3	0.9577
EAK-01-06	0.5650	0.0197	0.0724	0.0018	0.3530	0.0565	0.0008	451	11	472	31	452	19	95.4	0.7604
EAK-01-07	0.5800	0.0181	0.0722	0.0022	0.4906	0.0561	0.0009	449	14	457	34	459	21	98.4	0.2354
EAK-01-08	0.5585	0.0214	0.0728	0.0020	0.3673	0.0565	0.0007	453	13	472	29	452	21	96.0	0.8763
EAK-01-09	0.5644	0.0278	0.0719	0.0034	0.4845	0.0558	0.0011	447	21	444	46	452	33	100.8	0.7200
EAK-01-10	0.5705	0.0279	0.0720	0.0032	0.4503	0.0567	0.0009	448	20	479	33	454	32	93.5	0.5964
EAK-01-11	0.5609	0.0239	0.0735	0.0023	0.3628	0.0560	0.0008	457	14	451	33	455	24	101.4	0.7578
EAK-01-12	0.5641	0.0284	0.0726	0.0021	0.2850	0.0571	0.0011	452	13	494	44	452	23	91.3	0.8921
EAK-01-13	0.5625	0.0308	0.0746	0.0025	0.3048	0.0567	0.0010	464	15	478	38	461	27	97.0	0.6083
EAK-01-14	0.5879	0.0203	0.0721	0.0023	0.4624	0.0558	0.0010	449	14	443	40	460	23	101.3	0.1331
EAK-01-15	0.5837	0.0211	0.0736	0.0020	0.3791	0.0571	0.0008	458	13	497	31	462	21	92.1	0.5400
EAK-01-16	0.5565	0.0270	0.0712	0.0020	0.2963	0.0554	0.0012	444	13	427	49	445	23	103.8	0.7555
EAK-01-17	0.5251	0.0374	0.0723	0.0023	0.2198	0.0559	0.0014	450	14	447	54	446	26	100.7	0.3975
EAK-01-18	0.6153	0.0259	0.0757	0.0019	0.2918	0.0573	0.0012	471	12	504	47	475	21	93.3	0.3367
EAK-01-19	0.5623	0.0257	0.0751	0.0021	0.3121	0.0560	0.0008	467	13	450	34	462	23	103.6	0.4342
EAK-01-20	0.5780	0.0202	0.0750	0.0019	0.3596	0.0559	0.0009	466	12	448	35	465	20	104.0	0.8333
EAK-01-21	0.5463	0.0261	0.0722	0.0021	0.3105	0.0565	0.0009	449	13	473	37	447	23	95.0	0.6989
EAK-01-22	0.5587	0.0210	0.0744	0.0013	0.2360	0.0554	0.0010	463	8	428	38	460	15	108.1	0.3925
EAK-01-23	0.5606	0.0249	0.0713	0.0019	0.3064	0.0567	0.0013	444	12	480	52	446	21	92.5	0.6411
EAK-01-24	0.5572	0.0330	0.0728	0.0031	0.3591	0.0557	0.0013	453	19	441	50	452	33	102.8	0.8755
EAK-01-25	0.5855	0.0127	0.0719	0.0016	0.5172	0.0564	0.0007	447	10	470	29	461	15	95.2	0.0203
EAK-01-26	0.5301	0.0501	0.0726	0.0025	0.1835	0.0570	0.0018	452	16	492	71	450	29	91.9	0.5511
EAK-01-27	0.5674	0.0298	0.0744	0.0027	0.3491	0.0566	0.0010	462	17	476	37	460	29	97.2	0.7666

	ISOTOPIC RATIOS							CALCULATED AGES (Ma)							Prob. of
ID	$^{207}Pb/^{235}U$	$\pm1\sigma$	$^{206}Pb/^{238}U$	$\pm1\sigma$	Rho	$^{207}Pb/^{206}Pb$	$\pm1\sigma$	$^{206}Pb/^{238}U$	$\pm1\sigma$	$^{207}Pb/^{206}Pb$	$\pm1\sigma$	Conc. age	$\pm2\sigma$	Conc.	conc.
Sample EAK-01 - Blackish quartzites and phyllites															
EAK-01-28	0.8805	0.0475	0.1094	0.0035	0.2977	0.0611	0.0010	669	21	644	34	659	36	104.0	0.3096
EAK-01-29	0.5508	0.0246	0.0724	0.0017	0.2703	0.0567	0.0010	451	11	481	39	450	20	93.8	0.7510
EAK-01-30	0.5371	0.0207	0.0690	0.0019	0.3519	0.0562	0.0009	430	12	461	36	432	20	93.4	0.6615
EAK-01-31	0.5837	0.0247	0.0732	0.0028	0.4450	0.0563	0.0011	455	17	466	43	461	28	97.8	0.5022
EAK-01-32	0.5785	0.0231	0.0730	0.0014	0.2458	0.0572	0.0012	454	9	498	47	456	16	91.2	0.5429
EAK-01-33	0.5345	0.0373	0.0753	0.0027	0.2543	0.0562	0.0012	468	17	460	48	460	30	101.7	0.1913
EAK-01-34	0.5179	0.0407	0.0725	0.0029	0.2548	0.0550	0.0016	451	18	413	64	445	32	109.2	0.3288
EAK-01-35	0.5797	0.0321	0.0740	0.0031	0.3767	0.0563	0.0012	460	19	464	47	462	32	99.2	0.8504
EAK-01-36	0.6067	0.0256	0.0740	0.0024	0.3897	0.0569	0.0012	460	15	488	47	469	26	94.4	0.2156
EAK-01-37	0.8368	0.0482	0.0993	0.0039	0.3394	0.0621	0.0013	610	24	677	45	613	40	90.2	0.8052
EAK-01-38	0.5294	0.0379	0.0727	0.0029	0.2803	0.0563	0.0013	452	18	466	50	447	32	97.1	0.4243
EAK-01-39	0.5627	0.0257	0.0730	0.0027	0.4043	0.0568	0.0008	454	17	483	32	454	28	93.9	0.9646
EAK-01-40	0.5791	0.0238	0.0751	0.0022	0.3527	0.0558	0.0011	467	14	446	45	466	23	104.7	0.8428
EAK-01-41	0.5791	0.0284	0.0737	0.0025	0.3421	0.0566	0.0012	458	15	478	46	460	27	96.0	0.7729
EAK-01-42	0.5509	0.0254	0.0719	0.0024	0.3690	0.0563	0.0010	447	15	465	41	447	26	96.2	0.9202
EAK-01-43	0.8460	0.0325	0.1019	0.0035	0.4416	0.0591	0.0009	626	21	571	32	624	32	109.5	0.8680
EAK-01-44	0.5239	0.0289	0.0716	0.0030	0.3778	0.0554	0.0010	446	19	427	39	438	31	104.5	0.3885
EAK-01-45	0.5757	0.0337	0.0731	0.0031	0.3658	0.0558	0.0017	455	19	444	68	458	33	102.4	0.7725
EAK-01-46	0.5518	0.0295	0.0729	0.0029	0.3728	0.0571	0.0009	453	18	497	36	450	30	91.3	0.7241
EAK-01-47	0.5591	0.0248	0.0731	0.0024	0.3646	0.0558	0.0010	455	15	446	40	453	25	102.0	0.8343
EAK-01-48	0.4503	0.0349	0.0617	0.0034	0.3543	0.0549	0.0011	386	21	410	45	383	36	94.2	0.7350
EAK-01-49	0.5585	0.0266	0.0711	0.0027	0.4037	0.0570	0.0010	443	17	490	37	446	28	90.4	0.6664
EAK-01-50	0.6386	0.0255	0.0761	0.0029	0.4689	0.0562	0.0012	473	18	462	49	489	28	102.5	0.0953
EAK-01-51	0.5704	0.0281	0.0718	0.0028	0.3998	0.0570	0.0010	447	18	491	40	452	29	91.0	0.5532
EAK-01-52	0.5888	0.0302	0.0712	0.0026	0.3612	0.0559	0.0015	444	16	448	58	453	29	98.9	0.1894
EAK-01-53	0.6090	0.0287	0.0734	0.0032	0.4640	0.0566	0.0012	457	20	475	48	471	32	96.3	0.1773
EAK-01-54	0.5387	0.0263	0.0726	0.0025	0.3553	0.0550	0.0011	452	16	412	45	446	26	109.8	0.4372

	ISOTOPIC RATIOS							CALCULATED AGES (Ma)							Prob. of
ID	$^{207}Pb/^{235}U$	$\pm1\sigma$	$^{206}Pb/^{238}U$	$\pm1\sigma$	Rho	$^{207}Pb/^{206}Pb$	$\pm1\sigma$	$^{206}Pb/^{238}U$	$\pm1\sigma$	$^{207}Pb/^{206}Pb$	$\pm1\sigma$	Conc. age	$\pm2\sigma$	Conc.	conc.
Sample EAK-01 - Blackish quartzites and phyllites															
EAK-01-55	0.5528	0.0266	0.0740	0.0026	0.3604	0.0560	0.0009	460	16	452	36	455	27	101.7	0.4786
EAK-01-56	0.5479	0.0252	0.0724	0.0023	0.3450	0.0561	0.0009	451	14	457	36	448	24	98.7	0.6838
EAK-01-57	1.6571	0.0657	0.1686	0.0065	0.4883	0.0709	0.0008	1005	39	953	24	994	49	105.4	0.7021
EAK-01-58	0.5482	0.0286	0.0733	0.0023	0.3077	0.0570	0.0010	456	15	490	40	452	26	93.1	0.5322
EAK-01-59	0.5237	0.0319	0.0724	0.0027	0.3020	0.0555	0.0010	451	17	432	42	444	29	104.4	0.2972
EAK-01-60	0.5381	0.0324	0.0736	0.0027	0.3010	0.0560	0.0012	458	17	453	46	451	29	101.1	0.3594
EAK-01-61	0.5956	0.0229	0.0711	0.0024	0.4463	0.0565	0.0012	443	15	471	49	458	25	93.9	0.0404
EAK-01-62	0.5921	0.0313	0.0721	0.0035	0.4638	0.0562	0.0016	449	22	458	64	462	35	97.9	0.2763
EAK-01-63	0.5362	0.0249	0.0718	0.0025	0.3719	0.0552	0.0010	447	15	419	41	442	26	106.7	0.5382
EAK-01-64	0.5511	0.0507	0.0721	0.0046	0.3444	0.0572	0.0014	449	28	497	55	448	49	90.2	0.9306
EAK-01-65	0.5371	0.0323	0.0745	0.0029	0.3264	0.0556	0.0009	463	18	434	36	453	31	106.6	0.2355
EAK-01-66	0.5420	0.0341	0.0736	0.0030	0.3231	0.0567	0.0010	458	19	479	40	452	32	95.6	0.4420
EAK-01-67	0.5761	0.0344	0.0747	0.0032	0.3585	0.0562	0.0012	464	20	460	49	463	34	100.9	0.9190
EAK-01-68	0.5764	0.0334	0.0757	0.0027	0.3051	0.0573	0.0013	471	17	503	50	468	29	93.6	0.7061
EAK-01-69	0.5622	0.0337	0.0719	0.0037	0.4320	0.0568	0.0011	448	23	482	41	450	37	92.9	0.8236
EAK-01-70	0.5556	0.0317	0.0769	0.0024	0.2682	0.0562	0.0011	478	15	461	43	470	26	103.7	0.1777
EAK-01-71	0.5664	0.0372	0.0751	0.0036	0.3656	0.0555	0.0012	467	22	433	49	462	37	107.7	0.6689
EAK-01-72	0.5674	0.0276	0.0716	0.0026	0.3782	0.0560	0.0013	446	16	454	50	450	28	98.3	0.5757
EAK-01-73	0.5881	0.0297	0.0750	0.0023	0.3095	0.0557	0.0015	466	15	440	60	467	26	105.9	0.8715
EAK-01-74	0.5864	0.0299	0.0738	0.0031	0.4173	0.0573	0.0012	459	20	504	45	464	32	91.1	0.6503
EAK-01-75	1.1962	0.0562	0.1342	0.0057	0.4520	0.0655	0.0008	812	34	791	25	803	48	102.6	0.6766
EAK-01-76	0.5808	0.0232	0.0738	0.0026	0.4392	0.0555	0.0010	459	16	430	41	462	26	106.6	0.7069
EAK-01-77	0.5523	0.0229	0.0725	0.0025	0.4079	0.0563	0.0007	451	15	466	29	449	25	96.9	0.7687
EAK-01-78	0.5836	0.0348	0.0726	0.0037	0.4318	0.0559	0.0016	452	23	450	65	459	38	100.5	0.5272
EAK-01-79	0.5310	0.0329	0.0728	0.0027	0.2966	0.0565	0.0012	453	17	471	46	447	29	96.3	0.3685
EAK-01-80	0.8504	0.0400	0.1032	0.0042	0.4317	0.0609	0.0007	633	26	637	25	628	39	99.5	0.7317

	ISOTOPIC RATIOS							CALCULATED AGES (Ma)							Prob. of
ID	$^{207}Pb/^{235}U$	$\pm1\sigma$	$^{206}Pb/^{238}U$	$\pm1\sigma$	Rho	$^{207}Pb/^{206}Pb$	$\pm1\sigma$	$^{206}Pb/^{238}U$	$\pm1\sigma$	$^{207}Pb/^{206}Pb$	$\pm1\sigma$	Conc. age	$\pm2\sigma$	Conc.	conc.
Sample EJ-50 - Phyllites and metasiltstones															
EJ-50-01	0.5523	0.0410	0.0728	0.0042	0.3853	0.0567	0.0006	453	26	482	23	450	43	94.1	0.8153
EJ-50-02	0.8192	0.0423	0.1003	0.0036	0.3471	0.0612	0.0009	616	22	648	33	613	36	95.1	0.7358
EJ-50-03	1.4056	0.0656	0.1498	0.0060	0.4264	0.0680	0.0010	900	36	869	30	894	51	103.6	0.7990
EJ-50-04	1.0799	0.0788	0.1265	0.0064	0.3481	0.0652	0.0008	768	39	779	24	756	61	98.5	0.5712
EJ-50-05	0.3537	0.0176	0.0490	0.0019	0.3947	0.0531	0.0008	308	12	333	34	308	21	92.7	0.9449
EJ-50-06	0.9676	0.0376	0.1128	0.0039	0.4425	0.0620	0.0007	689	24	674	24	688	35	102.3	0.9358
EJ-50-07	0.5767	0.0269	0.0745	0.0030	0.4391	0.0564	0.0006	463	19	470	24	463	30	98.6	0.9644
EJ-50-08	0.5645	0.0277	0.0716	0.0036	0.5083	0.0564	0.0007	446	22	468	26	452	34	95.2	0.6659
EJ-50-09	0.8323	0.0311	0.1008	0.0034	0.4482	0.0594	0.0007	619	21	580	26	616	31	106.7	0.8255
EJ-50-10	0.8737	0.0353	0.1002	0.0040	0.4952	0.0618	0.0006	616	25	665	22	631	36	92.5	0.3125
EJ-50-11	0.7411	0.0445	0.0938	0.0048	0.4216	0.0592	0.0006	578	29	575	22	569	45	100.4	0.6132
EJ-50-12	0.3236	0.0198	0.0452	0.0025	0.4439	0.0526	0.0006	285	16	310	25	285	26	91.9	0.9818
EJ-50-13	5.5733	0.2243	0.3391	0.0140	0.5144	0.1180	0.0013	1882	78	1926	20	1912	69	97.7	0.6086
EJ-50-14	0.9564	0.0497	0.1134	0.0046	0.3886	0.0633	0.0009	692	28	717	30	687	44	96.6	0.7023
EJ-50-15	1.0706	0.0461	0.1194	0.0045	0.4344	0.0652	0.0007	727	27	782	22	734	41	93.0	0.6390
EJ-50-16	13.7241	0.5462	0.5180	0.0203	0.4912	0.1880	0.0016	2691	105	2725	14	2732	75	98.7	0.5929
EJ-50-17	0.8027	0.0594	0.1015	0.0038	0.2518	0.0599	0.0007	623	23	600	27	617	41	103.9	0.4730
EJ-50-18	0.6969	0.0506	0.0904	0.0049	0.3761	0.0584	0.0008	558	30	544	31	548	49	102.5	0.5324
EJ-50-19	0.2866	0.0152	0.0397	0.0026	0.6282	0.0514	0.0006	251	17	259	29	255	24	96.9	0.7007
EJ-50-20	0.6215	0.0367	0.0788	0.0046	0.4896	0.0572	0.0008	489	28	498	29	490	43	98.3	0.9484
EJ-50-21	0.7178	0.0560	0.0920	0.0051	0.3556	0.0598	0.0009	568	31	595	33	560	52	95.4	0.6119
EJ-50-22	7.3123	0.2201	0.3803	0.0227	0.9906	0.1298	0.0017	2078	124	2095	23	2174	10	99.2	0.3561
EJ-50-23	0.7863	0.0295	0.0929	0.0038	0.5450	0.0602	0.0006	573	23	611	21	586	33	93.7	0.3975
EJ-50-24	0.6154	0.0268	0.0744	0.0034	0.5241	0.0568	0.0008	463	21	483	30	479	32	95.7	0.1833
EJ-50-25	0.9813	0.0410	0.1134	0.0042	0.4399	0.0626	0.0009	692	25	693	30	694	38	99.9	0.9336
EJ-50-26	0.5787	0.0209	0.0744	0.0026	0.4873	0.0563	0.0007	463	16	464	26	463	25	99.7	0.9522
EJ-50-27	5.6881	0.2335	0.3482	0.0152	0.5324	0.1180	0.0009	1926	84	1927	14	1930	71	100.0	0.9565
EJ-50-28	5.4685	0.1470	0.3346	0.0110	0.6111	0.1160	0.0012	1861	61	1896	19	1900	45	98.1	0.4133
EJ-50-29	0.7671	0.0360	0.0913	0.0044	0.5152	0.0602	0.0006	563	27	610	23	574	39	92.3	0.5261
EJ-50-30	0.5863	0.0173	0.0701	0.0026	0.6307	0.0566	0.0008	437	16	477	32	466	22	91.6	0.0098

	ISOTOPIC RATIOS							CALCULATED AGES (Ma)							Prob. of
ID	$^{207}Pb/^{235}U$	$\pm1\sigma$	$^{206}Pb/^{238}U$	$\pm1\sigma$	Rho	$^{207}Pb/^{206}Pb$	$\pm1\sigma$	$^{206}Pb/^{238}U$	$\pm1\sigma$	$^{207}Pb/^{206}Pb$	$\pm1\sigma$	Conc. age	$\pm2\sigma$	Conc.	conc.
Sample EJ-50 - Phyllites and metasiltstones															
EJ-50-31	0.6250	0.0316	0.0813	0.0032	0.3946	0.0572	0.0009	504	20	500	33	498	33	100.8	0.6170
EJ-50-32	1.3081	0.0439	0.1394	0.0054	0.5788	0.0662	0.0009	841	33	812	28	849	39	103.6	0.7518
EJ-50-33	0.5615	0.0450	0.0733	0.0054	0.4567	0.0558	0.0009	456	33	446	38	454	52	102.3	0.9095
EJ-50-34	0.6055	0.0250	0.0776	0.0028	0.4366	0.0571	0.0008	482	17	497	30	481	28	97.0	0.9421
EJ-50-35	0.7970	0.0632	0.0957	0.0068	0.4463	0.0610	0.0009	589	42	638	31	593	64	92.4	0.8859
EJ-50-36	0.5870	0.0331	0.0804	0.0032	0.3501	0.0567	0.0007	498	20	479	26	486	33	104.0	0.1969
EJ-50-37	0.3250	0.0122	0.0453	0.0017	0.4861	0.0526	0.0006	286	10	311	26	286	17	91.9	0.9965
EJ-50-38	0.4279	0.0179	0.0597	0.0019	0.3829	0.0537	0.0008	374	12	358	32	368	20	104.3	0.3772
EJ-50-39	0.5896	0.0282	0.0781	0.0033	0.4441	0.0563	0.0006	485	21	463	23	476	32	104.6	0.4815
EJ-50-40	1.2012	0.0635	0.1356	0.0047	0.3260	0.0657	0.0010	820	28	797	32	812	45	102.8	0.5625
EJ-50-41	0.3068	0.0141	0.0438	0.0013	0.3348	0.0518	0.0006	276	8	278	27	275	15	99.5	0.6699
EJ-50-42	0.8323	0.0456	0.1013	0.0036	0.3219	0.0611	0.0008	622	22	641	30	619	37	97.0	0.7973
EJ-50-43	1.2789	0.0646	0.1346	0.0050	0.3684	0.0653	0.0016	814	30	784	50	825	48	103.9	0.4896
EJ-50-44	0.5786	0.0262	0.0746	0.0022	0.3306	0.0564	0.0010	464	14	468	39	464	24	99.0	0.9995
EJ-50-45	0.5220	0.0275	0.0691	0.0027	0.3694	0.0559	0.0007	431	17	449	26	429	28	96.0	0.8221
EJ-50-46	0.7881	0.0379	0.0979	0.0029	0.3061	0.0602	0.0008	602	18	612	28	598	30	98.3	0.5983
EJ-50-47	0.3249	0.0187	0.0461	0.0015	0.2761	0.0523	0.0010	291	9	296	46	290	17	98.1	0.7297
EJ-50-48	1.5669	0.0671	0.1552	0.0047	0.3559	0.0723	0.0010	930	28	993	29	943	44	93.7	0.3719
EJ-50-49	0.6115	0.0230	0.0772	0.0018	0.3126	0.0572	0.0009	479	11	499	36	481	20	96.2	0.7402
EJ-50-50	0.5614	0.0201	0.0723	0.0017	0.3334	0.0550	0.0008	450	11	413	32	451	19	108.9	0.8649
EJ-50-51	0.9162	0.0411	0.1040	0.0035	0.3748	0.0627	0.0010	638	21	696	35	648	35	91.6	0.3436
EJ-50-52	0.8088	0.0401	0.0975	0.0042	0.4390	0.0598	0.0008	600	26	595	28	601	40	100.8	0.9324
EJ-50-53	0.5644	0.0313	0.0756	0.0027	0.3243	0.0572	0.0008	470	17	499	30	464	29	94.1	0.4788
EJ-50-54	0.6244	0.0221	0.0778	0.0019	0.3497	0.0574	0.0009	483	12	506	33	486	21	95.4	0.5097
EJ-50-55	1.2821	0.0568	0.1401	0.0046	0.3738	0.0670	0.0007	845	28	839	23	841	43	100.7	0.8008
EJ-50-56	0.8174	0.0359	0.0998	0.0027	0.3081	0.0608	0.0008	613	17	633	27	611	28	96.9	0.7525
EJ-50-57	0.5808	0.0421	0.0766	0.0040	0.3587	0.0565	0.0008	476	25	472	31	471	42	100.8	0.7121
EJ-50-58	0.5902	0.0318	0.0759	0.0029	0.3581	0.0570	0.0008	472	18	490	30	472	31	96.4	0.9675
EJ-50-59	1.7266	0.0779	0.1653	0.0057	0.3826	0.0744	0.0011	986	34	1051	30	1004	51	93.8	0.3363
EJ-50-60	0.5379	0.0216	0.0731	0.0015	0.2524	0.0560	0.0009	455	9	452	34	451	17	100.7	0.2293
EJ-50-61	1.1502	0.0571	0.1292	0.0052	0.4087	0.0646	0.0009	783	32	761	28	780	47	102.9	0.8441

	ISOTOPIC RATIOS							CALCULATED AGES (Ma)							Prob. of
ID	$^{207}Pb/^{235}U$	$\pm1\sigma$	$^{206}Pb/^{238}U$	$\pm1\sigma$	Rho	$^{207}Pb/^{206}Pb$	$\pm1\sigma$	$^{206}Pb/^{238}U$	$\pm1\sigma$	$^{207}Pb/^{206}Pb$	$\pm1\sigma$	Conc. age	$\pm2\sigma$	Conc.	conc.
Sample EJ-50 - Phyllites and metasiltstones - YOUNG GRAINS															
EJ-50-63	0.0384	0.0039	0.0048	0.0004	0.44	0.0499	0.0016	31	3	190	77	32	5	16.1	0.0309
EJ-50-64	0.0403	0.0028	0.0051	0.0002	0.28	0.0558	0.0020	33	1	446	80	34	3	7.4	0.0085
EJ-50-65	0.0301	0.0024	0.0048	0.0004	0.52	0.0449	0.0011	31	3	-61	61	30	4	-50.8	0.7643
EJ-50-66	0.0403	0.0025	0.0049	0.0003	0.51	0.0531	0.0019	31	2	332	82	34	4	9.4	0.0001
EJ-50-67	0.0379	0.0031	0.0056	0.0003	0.36	0.0447	0.0019	36	2	-73	105	36	4	-49.2	0.5477
EJ-50-68	0.0314	0.0019	0.0049	0.0002	0.32	0.0463	0.0013	31	1	11	66	31	2	277.2	0.9521
EJ-50-69	0.0345	0.0022	0.0050	0.0003	0.56	0.0460	0.0017	32	2	-4	88	33	4	-729.4	0.2413
EJ-50-70	0.0325	0.0024	0.0052	0.0002	0.31	0.0456	0.0010	34	2	-25	55	33	3	-136.5	0.6227
EJ-50-71	0.0300	0.0021	0.0049	0.0002	0.34	0.0449	0.0013	31	1	-63	69	31	3	-49.4	0.5280
EJ-50-72	0.0351	0.0034	0.0051	0.0003	0.27	0.0537	0.0026	33	2	358	111	33	3	9.1	0.4709
EJ-50-73	0.0307	0.0027	0.0049	0.0003	0.37	0.0453	0.0016	32	2	-37	83	31	4	-85.2	0.7604
EJ-50-74	0.0399	0.0022	0.0063	0.0002	0.28	0.0481	0.0011	41	1	104	56	41	2	39.2	0.6319
EJ-50-75	0.0348	0.0035	0.0048	0.0003	0.36	0.0523	0.0020	31	2	298	88	31	4	10.3	0.2217
EJ-50-76	0.0346	0.0023	0.0051	0.0002	0.28	0.0518	0.0014	33	1	276	61	33	2	11.8	0.3637
EJ-50-77	0.0392	0.0053	0.0051	0.0003	0.20	0.0656	0.0027	33	2	793	86	33	4	4.2	0.2480
EJ-50-78	0.0371	0.0027	0.0050	0.0002	0.29	0.0548	0.0019	32	1	405	78	33	3	7.9	0.0508
EJ-50-79	0.0340	0.0017	0.0049	0.0002	0.46	0.0467	0.0013	32	1	33	66	33	3	95.0	0.1788
EJ-50-80	0.0368	0.0025	0.0048	0.0002	0.34	0.0523	0.0018	31	1	297	78	32	3	10.4	0.0158
EJ-50-81	0.0423	0.0034	0.0044	0.0007	0.99	0.0586	0.0028	29	5	552	105	71	3	5.2	0.0000
EJ-50-82	0.0605	0.0079	0.0060	0.0002	0.14	0.0664	0.0026	38	1	819	83	39	3	4.7	0.0053
EJ-50-83	0.0729	0.0036	0.0111	0.0003	0.31	0.0500	0.0009	71	2	193	41	71	4	36.7	0.8970
EJ-50-84	0.0297	0.0030	0.0048	0.0002	0.18	0.0475	0.0020	31	1	74	100	31	2	42.3	0.6332
EJ-50-85	0.0294	0.0066	0.0057	0.0002	0.08	0.0519	0.0024	37	1	283	105	36	2	12.9	0.2731

	ISOTOPIC RATIOS							CALCULATED AGES (Ma)							Prob. of
ID	$^{207}Pb/^{235}U$	$\pm1\sigma$	$^{206}Pb/^{238}U$	$\pm1\sigma$	Rho	$^{207}Pb/^{206}Pb$	$\pm1\sigma$	$^{206}Pb/^{238}U$	$\pm1\sigma$	$^{207}Pb/^{206}Pb$	$\pm1\sigma$	Conc. age	$\pm2\sigma$	Conc.	conc.
Sample EJ-50 - Phyllites and metasiltstones - YOUNG GRAINS															
EJ-50-86	0.0315	0.0018	0.0048	0.0002	0.29	0.0471	0.0014	31	1	55	68	31	2	56.6	0.7832
EJ-50-87	0.0349	0.0023	0.0047	0.0002	0.37	0.0502	0.0017	30	2	205	81	31	3	14.8	0.0436
EJ-50-88	0.0257	0.0036	0.0051	0.0003	0.20	0.0413	0.0016	33	2	-270	100	32	3	-12.1	0.0648
EJ-50-89	0.0627	0.0060	0.0052	0.0001	0.15	0.0762	0.0049	33	1	1099	129	33	2	3.0	0.0000
EJ-50-90	0.0406	0.0034	0.0059	0.0003	0.28	0.0497	0.0017	38	2	183	78	38	3	20.6	0.4046
EJ-50-91	0.0313	0.0030	0.0048	0.0002	0.23	0.0481	0.0021	31	1	102	105	31	3	30.1	0.8467
EJ-50-92	0.0727	0.0101	0.0052	0.0003	0.22	0.0995	0.0072	33	2	1614	134	33	4	2.1	0.0001
EJ-50-93	0.0333	0.0042	0.0051	0.0004	0.28	0.0489	0.0021	32	2	144	103	33	4	22.6	0.8481
EJ-50-94	0.0214	0.0059	0.0048	0.0003	0.10	0.0447	0.0029	31	2	-74	158	30	3	-41.8	0.1120
EJ-50-95	0.0284	0.0037	0.0049	0.0002	0.17	0.0507	0.0017	32	1	228	76	31	3	13.8	0.4073
EJ-50-96	0.0327	0.0065	0.0055	0.0004	0.20	0.0463	0.0019	36	3	14	100	35	5	254.7	0.6595
EJ-50-97	0.0403	0.0034	0.0050	0.0002	0.19	0.0627	0.0023	32	1	696	77	33	2	4.6	0.0177
EJ-50-98	0.0707	0.0070	0.0056	0.0002	0.14	0.0726	0.0040	36	1	1003	112	36	2	3.6	0.0000
EJ-50-99	0.0340	0.0055	0.0046	0.0003	0.23	0.0598	0.0026	30	2	598	93	30	4	5.0	0.4435
EJ-50-100	0.0290	0.0038	0.0049	0.0002	0.16	0.0511	0.0018	32	1	246	80	31	3	12.8	0.5085
EJ-50-101	0.0215	0.0109	0.0048	0.0005	0.11	0.0450	0.0030	31	3	-55	163	30	7	-56.2	0.3930
EJ-50-102	0.0329	0.0043	0.0062	0.0002	0.14	0.0495	0.0017	40	2	172	82	39	3	23.2	0.1042
EJ-50-103	0.0339	0.0023	0.0052	0.0002	0.33	0.0443	0.0019	33	1	-92	104	33	3	-36.0	0.7315
EJ-50-104	0.0311	0.0030	0.0049	0.0002	0.22	0.0488	0.0018	32	1	140	86	32	3	22.7	0.8110
EJ-50-105	0.0852	0.0083	0.0101	0.0005	0.24	0.0603	0.0035	65	3	615	124	66	6	10.5	0.0180
EJ-50-106	0.0325	0.0047	0.0052	0.0003	0.17	0.0534	0.0023	34	2	345	98	34	3	9.8	0.7860
EJ-50-107	0.0320	0.0020	0.0049	0.0001	0.23	0.0460	0.0017	31	1	-3	89	31	2	-931.3	0.7509

	ISOTOPIC RATIOS							CALCULATED AGES (Ma)							Prob. of
ID	$^{207}Pb/^{235}U$	$\pm1\sigma$	$^{206}Pb/^{238}U$	$\pm1\sigma$	Rho	$^{207}Pb/^{206}Pb$	$\pm1\sigma$	$^{206}Pb/^{238}U$	$\pm1\sigma$	$^{207}Pb/^{206}Pb$	$\pm1\sigma$	Conc. age	$\pm2\sigma$	Conc.	conc.
Sample EHS-06 - Rio Marina Formation															
EHS-06-01	1.7130	0.1108	0.1677	0.0071	0.3274	0.0754	0.0009	1000	42	1079	25	1006	66	92.6	0.7695
EHS-06-02	0.9074	0.0468	0.1087	0.0033	0.2962	0.0601	0.0017	665	20	606	60	662	34	109.8	0.7194
EHS-06-03	1.0400	0.0420	0.1160	0.0032	0.3445	0.0629	0.0013	707	20	707	44	714	32	100.1	0.4696
EHS-06-04	0.9814	0.0488	0.1170	0.0035	0.3012	0.0643	0.0013	713	21	752	43	706	36	94.9	0.4821
EHS-06-05	5.6758	0.2299	0.3407	0.0074	0.2664	0.1269	0.0015	1890	41	2056	21	1909	56	91.9	0.3787
EHS-06-06	1.5531	0.0707	0.1538	0.0050	0.3556	0.0727	0.0011	922	30	1006	32	936	46	91.6	0.3569
EHS-06-07	0.8468	0.0284	0.0988	0.0021	0.3219	0.0611	0.0009	608	13	642	31	613	22	94.6	0.3582
EHS-06-08	0.7769	0.0263	0.0952	0.0020	0.3091	0.0602	0.0008	586	12	610	28	585	21	96.1	0.8744
EHS-06-09	0.5138	0.0484	0.0676	0.0061	0.4796	0.0554	0.0010	421	38	430	42	421	59	98.1	0.9905
EHS-06-10	1.7882	0.0954	0.1715	0.0082	0.4459	0.0764	0.0013	1020	49	1106	34	1035	65	92.2	0.6232
EHS-06-11	0.5212	0.0189	0.0674	0.0023	0.4629	0.0563	0.0010	420	14	464	39	424	22	90.7	0.6857
EHS-06-12	0.7746	0.0300	0.0914	0.0036	0.5106	0.0600	0.0010	564	22	605	36	577	33	93.2	0.3410
EHS-06-13	0.5366	0.0203	0.0716	0.0024	0.4498	0.0554	0.0012	446	15	430	47	440	24	103.6	0.5194
EHS-06-14	0.5575	0.0257	0.0687	0.0029	0.4628	0.0564	0.0017	429	18	467	68	440	30	91.8	0.2329
EHS-06-15	5.7927	0.3095	0.3441	0.0205	0.5580	0.1197	0.0019	1906	114	1952	28	1948	92	97.7	0.6337
EHS-06-16	1.4688	0.0527	0.1477	0.0060	0.5700	0.0714	0.0013	888	36	968	36	916	43	91.8	0.2867
EHS-06-17	0.7626	0.0344	0.0915	0.0039	0.4762	0.0606	0.0011	564	24	625	38	571	37	90.2	0.6110
EHS-06-18	0.8705	0.0454	0.1033	0.0050	0.4663	0.0620	0.0014	634	31	674	48	635	45	94.1	0.9442
EHS-06-19	0.5487	0.0178	0.0703	0.0021	0.4580	0.0569	0.0010	438	13	486	38	442	21	90.2	0.6409
EHS-06-20	1.5588	0.0846	0.1560	0.0070	0.4108	0.0728	0.0013	934	42	1007	38	946	60	92.8	0.6188

	ISOTOPIC RATIOS							CALCULATED AGES (Ma)							Prob. of
ID	$^{207}Pb/^{235}U$	$\pm1\sigma$	$^{206}Pb/^{238}U$	$\pm1\sigma$	Rho	$^{207}Pb/^{206}Pb$	$\pm1\sigma$	$^{206}Pb/^{238}U$	$\pm1\sigma$	$^{207}Pb/^{206}Pb$	$\pm1\sigma$	Conc. age	$\pm2\sigma$	Conc.	conc.
Sample EHS-05 - Verruca Formation															
EHS-05-01	0.4139	0.0178	0.0567	0.0014	0.2846	0.0542	0.0010	356	9	379	41	355	16	93.8	0.7576
EHS-05-02	7.0120	0.2837	0.3689	0.0113	0.3798	0.1374	0.0018	2024	62	2195	23	2093	69	92.2	0.0855
EHS-05-03	0.5070	0.0236	0.0675	0.0018	0.2933	0.0555	0.0010	421	12	434	39	420	20	97.1	0.7778
EHS-05-04	0.6224	0.0228	0.0781	0.0017	0.2999	0.0581	0.0009	485	11	534	33	487	19	90.8	0.6668
EHS-05-05	0.5731	0.0203	0.0736	0.0016	0.3088	0.0565	0.0008	458	10	472	32	458	18	96.9	0.8619
EHS-05-06	0.5697	0.0471	0.0748	0.0043	0.3480	0.0574	0.0011	465	27	507	43	462	45	91.7	0.8255
EHS-05-07	0.6575	0.0293	0.0820	0.0030	0.4133	0.0584	0.0008	508	19	544	29	510	30	93.4	0.7871
EHS-05-08	0.5290	0.0184	0.0688	0.0015	0.3115	0.0561	0.0009	429	9	454	34	430	16	94.4	0.8757
EHS-05-09	0.4139	0.0179	0.0573	0.0013	0.2696	0.0543	0.0009	359	8	385	36	358	15	93.4	0.5641
EHS-05-10	1.0081	0.0694	0.1187	0.0047	0.2893	0.0648	0.0013	723	29	768	41	718	48	94.2	0.6846
EHS-05-11	5.1961	0.1982	0.3221	0.0082	0.3318	0.1166	0.0018	1800	46	1905	27	1833	58	94.5	0.2181
EHS-05-12	0.9132	0.0397	0.1110	0.0026	0.2644	0.0627	0.0009	679	16	697	29	673	27	97.4	0.3703
EHS-05-13	0.7398	0.0321	0.0947	0.0021	0.2511	0.0599	0.0009	584	13	601	33	578	22	97.2	0.2748
EHS-05-14	0.8995	0.0391	0.1075	0.0028	0.2992	0.0629	0.0010	658	17	704	33	656	29	93.6	0.7551
EHS-05-15	0.7897	0.0319	0.0973	0.0026	0.3276	0.0593	0.0010	598	16	579	38	596	27	103.4	0.7027
EHS-05-16	6.1236	0.2452	0.3587	0.0092	0.3192	0.1297	0.0017	1976	51	2094	23	1987	62	94.4	0.7008
EHS-05-17	5.3844	0.2612	0.3415	0.0105	0.3160	0.1206	0.0016	1894	58	1965	24	1887	73	96.4	0.8317
EHS-05-18	0.3671	0.0150	0.0516	0.0014	0.3433	0.0529	0.0008	324	9	325	32	322	16	99.8	0.5662
EHS-05-19	0.9712	0.0349	0.1124	0.0026	0.3234	0.0643	0.0010	687	16	752	34	688	27	91.3	0.9021
EHS-05-20	0.2915	0.0162	0.0410	0.0017	0.3831	0.0520	0.0009	259	11	284	38	259	19	91.1	0.9504
EHS-05-21	1.4558	0.0728	0.1537	0.0042	0.2718	0.0725	0.0012	921	25	1000	33	918	41	92.1	0.7795
EHS-05-22	0.6387	0.0608	0.0878	0.0025	0.1492	0.0589	0.0016	543	15	565	57	539	29	96.1	0.2742
EHS-05-23	0.5768	0.0185	0.0721	0.0016	0.3476	0.0560	0.0008	449	10	451	30	453	17	99.5	0.2731
EHS-05-24	0.3197	0.0165	0.0455	0.0013	0.2672	0.0526	0.0009	287	8	314	39	286	15	91.5	0.6749
EHS-05-25	0.3567	0.0152	0.0455	0.0024	0.6098	0.0522	0.0008	287	15	294	36	305	22	97.5	0.0513

	ISOTOPIC RATIOS							CALCULATED AGES (Ma)							Prob. of
ID	$^{207}Pb/^{235}U$	$\pm1\sigma$	$^{206}Pb/^{238}U$	$\pm1\sigma$	Rho	$^{207}Pb/^{206}Pb$	$\pm1\sigma$	$^{206}Pb/^{238}U$	$\pm1\sigma$	$^{207}Pb/^{206}Pb$	$\pm1\sigma$	Conc. age	$\pm2\sigma$	Conc.	conc.
Sample EHS-05 - Verruca Formation															
EHS-05-26	0.3147	0.0136	0.0451	0.0011	0.27	0.0517	0.0007	285	7	272	32	283	12	104.5	0.5232
EHS-05-27	0.3256	0.0202	0.0441	0.0016	0.29	0.0525	0.0015	278	10	306	63	280	18	91.1	0.6169
EHS-05-28	1.7039	0.0920	0.1662	0.0062	0.34	0.0735	0.0010	991	37	1028	28	1000	56	96.4	0.6299
EHS-05-29	0.4026	0.0343	0.0559	0.0027	0.28	0.0537	0.0012	350	17	358	51	349	31	97.9	0.7859
EHS-05-30	4.6531	0.2077	0.2968	0.0078	0.29	0.1116	0.0014	1676	44	1825	23	1717	62	91.8	0.0677
EHS-05-31	5.8102	0.2314	0.3412	0.0072	0.26	0.1232	0.0013	1893	40	2004	19	1919	55	94.5	0.1887
EHS-05-32	13.7410	0.5412	0.4881	0.0132	0.34	0.1949	0.0023	2562	69	2784	20	2692	73	92.0	0.0025
EHS-05-33	11.4311	0.5286	0.4679	0.0131	0.30	0.1762	0.0021	2474	69	2617	20	2532	79	94.5	0.1620
EHS-05-34	0.3156	0.0160	0.0445	0.0022	0.48	0.0518	0.0013	280	14	276	59	279	22	101.4	0.8873
EHS-05-35	0.7527	0.0296	0.0901	0.0049	0.69	0.0592	0.0008	556	30	575	31	571	34	96.8	0.5207
EHS-05-36	11.3442	0.4132	0.4580	0.0237	0.71	0.1760	0.0024	2431	126	2615	23	2575	58	92.9	0.1452
EHS-05-37	0.8140	0.0336	0.0950	0.0050	0.64	0.0604	0.0012	585	31	618	42	605	38	94.7	0.3851
EHS-05-38	10.6116	0.4317	0.4467	0.0235	0.65	0.1740	0.0024	2380	125	2596	23	2507	70	91.7	0.1954
EHS-05-39	0.6406	0.0359	0.0811	0.0043	0.48	0.0581	0.0012	503	27	532	44	503	41	94.4	0.9956
EHS-05-40	0.7166	0.0322	0.0894	0.0045	0.56	0.0595	0.0011	552	28	584	42	549	37	94.5	0.8725
EHS-05-41	0.5507	0.0214	0.0728	0.0036	0.63	0.0564	0.0008	453	22	468	33	446	28	96.9	0.6411
EHS-05-42	0.7691	0.0340	0.0949	0.0050	0.60	0.0598	0.0009	584	31	597	32	580	39	97.8	0.8348
EHS-05-43	6.0151	0.2095	0.3456	0.0172	0.72	0.1248	0.0017	1914	95	2025	24	1992	54	94.5	0.3150
EHS-05-44	0.3635	0.0155	0.0500	0.0026	0.60	0.0530	0.0008	315	16	331	35	315	23	95.1	0.9837
EHS-05-45	0.6298	0.0349	0.0826	0.0044	0.48	0.0573	0.0012	512	27	504	47	501	40	101.6	0.5237
EHS-05-46	0.5430	0.0254	0.0706	0.0039	0.58	0.0557	0.0009	440	24	439	37	440	33	100.2	0.9704
EHS-05-47	0.3393	0.0130	0.0463	0.0022	0.64	0.0520	0.0009	292	14	284	38	296	20	102.8	0.6346
EHS-05-48	0.6918	0.0376	0.0874	0.0048	0.51	0.0593	0.0010	540	30	579	36	536	43	93.3	0.8052
EHS-05-49	1.1421	0.0586	0.1246	0.0076	0.59	0.0657	0.0010	757	46	797	31	773	55	94.9	0.6338